NASA CR-72080
Aerotherm Report No. 66-2

Aerotherm Copy No. 25

FINAL REPORT

STUDIES OF NOZZLE ABLATIVE MATERIAL PERFORMANCE FOR LARGE SOLID BOOSTERS

by

John W. Schaefer and Thomas J. Dahm

prepared for

NATIONAL AERONAUTICS AND SPACE ADMINISTRATION

December 15, 1966

CONTRACT NAS7-405

Itek Corporation
Vidya Division P.O. 8280 V9003

Technical Management
NASA Lewis Research Center
Cleveland, Ohio
Solid Rocket Technology Branch
J. J. Notardonato

AEROTHERM CORPORATION

460 CALIFORNIA AVENUE, PALO ALTO, CALIFORNIA 94306 - TELEPHONE (415) 327-8262 TWX 415-492-9243

ABSTRACT

Analytical and experimental studies of nozzle ablative material performance for large solid boosters were performed. Carbon phenolic, graphite phenolic, and silica phenolic materials were considered. Predictions of material performance for three large booster nozzles (260-SL-1, 120-SS-1, and UA-1205-10) were made using ablation computer programs. An analysis of material performance was made through comparisons of the predicted and measured performance. Tests to study the ablative material performance were conducted using an arc-plasma generator to simulate the solid propellant environment; the ablative material test sections were in the form of supersonic nozzles. Char thermal conductivity was also determined under dynamic conditions using this test approach. Some special studies were performed and areas that require future study were identified.

SUMMARY

Analytical and experimental studies of nozzle ablative material performance for large solid boosters were performed. The two main study efforts were the prediction and analysis of ablative material performance for three large solid boosters and the laboratory testing and analysis of ablative materials to determine their performance characteristics and properties. Some special studies were also performed and areas that require future study were identified.

Predictions of material performance using the Aerotherm ablation computer programs were made for carbon phenolic, graphite phenolic, and silica phenolic in the nozzles of the Aerojet 260-SL-1, Aerojet 120-SS-1, and UTC UA-1205-1 motors. These predictions were compared with the measured material performance, thereby providing the basis for the analysis of the material performance and of the computer prediction technique. The carbon phenolic and graphite phenolic materials performed, by and large, as expected and predicted. The silica phenolic materials were not consistently predictable and the reasons for this problem were identified. The analysis demonstrated that significant cost and weight savings can be effected through the use of thinner ablative parts without sacrafice of ablative material thermal protection performance (assuming structural integrity can also be maintained) and that, for the conditions and materials considered, the type of cure had little or no effect on the material performance.

Tests using the Aerotherm arc-plasma generator were conducted to determine the performance characteristics and properties of carbon phenolic and graphite phenolic. The material test sections were supersonic nozzles that formed the exit nozzle of the arc-plasma generator; the test environments simulated a typical solid propellant. Char thermal conductivity was determined for carbon phenolic and graphite phenolic under dynamic conditions typical of a solid rocket application using this test approach. The surface erosion, char depth, and insulation performance were also studied for these materials. As expected, the surface erosion performance of carbon phenolic and graphite phenolic are comparable, but carbon phenolic exhibits a lower char depth and better insulation performance due to its lower virgin material and char thermal conductivities.

The study of special problems encompassed four specific efforts, the main one being an analysis and extension of the theoretical approach to calculating heat and mass transfer coefficients. The other efforts were a calculation of heat flux and heat transfer coefficients for a hypothetical 260-inch liquid-cooled nozzle, the study of the effects on material performance of a quench after shutdown, and predictions of material performance in support of an Air Force program to characterize carbon and graphite phenolic chars.

Finally, the problem areas of nozzle design and material performance that require future study were defined and possible approaches to their solution suggested.

TABLE OF CONTENTS

TABLE OF CONTENTS

LIST OF TABLES

LIST OF FIGURES

LIST OF FIGURES (continued)

LIST OF FIGURES (concluded)

LIST OF SYMBOLS

a	constant in Equation (A2)
A	area, or constant in Equations (A8), (A11), (A15)
B	pre-exponential constant
$\dot{B}$	β/C_H^*
C_H	Stanton number
C_{H_T}	isothermal wall Stanton number
C_H^*	non-ablating wall Stanton number
C_M	mass transfer Stanton number
c_p	specific heat at constant pressure
D	diameter
E	voltage, or activation energy
G	Equation (A6)
h_T	heat transfer coefficient based on temperature driving potential
h	enthalpy
h_r	recovery enthalpy
I	current
k	thermal conductivity
L	characteristic axial length
Le	Lewis number
m	exponent in Equation (A2)
$\dot{m}$	mass flow rate
$\dot{m}_c$	char mass flux
$\dot{m}_g$	pyrolysis gas mass flux
n	exponent in $u_e \propto x^n$
Nu_R	Nusselt number based on radius $\frac{(\rho_e u_e C_H)\ c_p R}{k}$
p	pressure
Pr	Prandtl number
q	heat flux
q_r	radiation heat flux
r, R	radius
R	enthalpy recovery factor, or gas constant
Re_x	length Reynolds number, $\frac{\rho_e u_e x}{\mu}$

Re_{φ}	energy thickness Reynolds number, $\frac{\rho_e u_e \varphi}{\mu}$
Re_R	Reynolds number based on radius $\frac{\rho_e u_e R}{\mu_\infty}$
T	temperature
u	velocity, freestream or parallel to x coordinate
v	velocity parallel to y coordinate
x	surface coordinate
y	coordinate normal to a surface
z	axial coordinate
β	blowing rate $\frac{(\rho v)_w}{(\rho u)_e}$
ϵ	emissivity
θ	material layup angle, or time
λ	constant in local blowing correction - Equation (A18)
$\overline{\lambda}$	constant in average blowing correction - Equation (A23)
μ	viscosity
ρ	density
ρ_{o_i}	original density
ρ_{r_i}	residual density
σ	Stefan-Boltzmann constant
φ	energy thickness, $\int_o^\infty \frac{\rho u}{\rho_e u_e} \frac{h_{te} - h_t}{h_{te} - h_w} dy$

Subscripts

c	chamber
e	boundary layer edge
i	initial, input, or component i
o,t	stagnation
w	wall
x	refers to constant Re_x
∞	freestream
φ	refers to constant Re_φ
ψ	density ratio exponent
*	throat

2. PREDICTION OF LARGE BOOSTER NOZZLE ABLATIVE MATERIAL PERFORMANCE

2.1 Introduction

The Aerotherm ablation computer programs were used to predict the ablative material performance for the nozzles of the following large booster motors

Motor	Firing Date	Brief Description
Aerojet 260-SL-1	September 19, 1964	half-length 260-inch motor
Aerojet 120-SS-1	September 25, 1965	120-inch subscale to the Aerojet 260-inch motor
UTC UA-1205-10	December 17, 1964	120-inch Titan IIIC strap-on development motor

The locations for which predictions were made encompassed the subsonic, throat, and supersonic regions of the nozzles. The predicted performance was compared with the available measured performance results for each nozzle. These results provided the basis for the analysis of materials performance in each firing, including future design recommendations and the identification of the probable cause for any anomalous or unexpected results. Also, these results provided an evaluation of the computer programs for use in rocket nozzle design and a definition of areas where computer program improvements might be desirable.[1]

The following sections discuss the predictions for the three nozzles considered and their comparisons with measured performance. The nozzle configurations, including the ablative materials used, and the firing conditions are presented in Section 2.2. Section 2.3 discusses the prediction technique; the computer programs are briefly described and the input information to the computer programs is presented. The predicted and measured material performance for all locations in the three nozzles is presented and discussed in Section 2.4, these results covering surface erosion depth, char depth, insulation performance, and other material performance variables. Finally, a summary of the results and conclusions is presented in Section 2.5.

2.2 Description of Nozzle Configurations and Firing Conditions

The nozzle configurations and firing conditions for the three motors are presented in the following sections. The chamber conditions and propellant are described in Section 2.2.1. The nozzle configurations, the nozzle ablative materials, and the locations for which predictions were made are presented in Section 2.2.2.

---

[1] Predictions and analyses of material performance for the Thiokol 156-2C-1 nozzle and the LPC 156-5 and 156-6 submerged nozzles are presented in References 1-4. These results and the results of this contract are summarized in Reference 5.

1.0 INTRODUCTION

A large solid rocket booster represents a sizeable investment in terms of both money and time. The development of such motors must therefore be accomplished with a minimum number of development motor firings and a maximum utilization of less costly analytic and laboratory techniques in support of this development. The ablative nozzles of solid propellant rocket motors have, historically, been designed by costly and time consuming cut-and-try approaches. For the smaller motors of the past, these approaches were economically justifiable; they were also necessary because of the absence of reliable techniques, both for analytic analysis and laboratory test, to support ablative nozzle design. Such techniques are now available, however, and some results of their application are presented in this report. The use of ablation computer programs in support of nozzle design and for analysis of ablative material performance is demonstrated through predictions of material performance for three large booster nozzles. The use of laboratory techniques in support of nozzle design and for analysis of ablative material performance is demonstrated through tests on ablative materials to define their properties and performance characteristics.

Specifically, computer program predictions of surface erosion depth, char depth, and internal thermal response were made for the nozzles of the Aerojet 260-SL-1 motor, the Aerojet 120-SS-1 motor, and the UTC UA-1205-10 motor. Carbon phenolic, graphite phenolic, and silica phenolic exposed ablative materials were considered; predictions were made for 5 locations in each nozzle. Wherever possible, comparisons were made with post-fire measurements. These results are presented in Section 2. Arc-plasma generator firings under simulated solid propellant combustion products conditions were performed on supersonic nozzles of carbon phenolic materials and graphite phenolic materials. From these firings the char thermal conductivity of the materials was determined, their surface erosion, char depth, and insulation performance were evaluated, and the effect of upstream ablation on surface erosion was studied. These results are presented in Section 3. The results of some special studies in related problem areas performed during the contract are presented in Section 4. This includes the evaluation and extension of a useful technique for calculating heat and mass transfer coefficients for solid propellant ablative nozzles. Section 5 presents some recommendations for future work.

The authors express their appreciation to the many Aerotherm staff members who have contributed to the study. Particular thanks go to D. T. Flood, J. J. Reese, K. J. Clark, D. Y. Cheng, and T. Wong. The contributions of the NASA Technical Monitors, J. J. Notardonato and J. F. McBride are also gratefully acknowledged.

2.2.1 Propellant and chamber conditions

The propellant for the Aerojet 260-SL-1 and 120-SS-1 motors was a standard aluminized propellant designated ANB-3105. The propellant grain ports were a cloverleaf configuration with a "star" valley (minimum) diameter less than the throat diameter. The propellant for the UTC UA-1205-10 motor also was a standard aluminized propellant and was designated UTP-3001. The propellant grain port was circular.

The chamber conditions and web times are summarized below:

Motor	Web Time	Web Time Average Chamber Pressure	Chamber Temperature at 1000 psia
	sec	psia	^{o}K
260-SL-1	114	533	3380
120-SS-1	74.4	519	3380
UA-1205-10	109.2	520	3408

The measured chamber pressure histories for the three motors were available and used in the calculation of transfer coefficients as discussed in Section 2.3.2.3, Transfer Coefficients.

2.2.2 Nozzle configurations, materials, and locations for analysis

The nozzle configurations for the 260-SL-1, 120-SS-1, and UA-1205-10 motors are presented in Figures 1-3, respectively. The two Aerojet nozzles were conventional convergent-divergent nozzles. The UTC nozzle was convergent-divergent with an unusually short convergent section, the nozzle entry area ratio being $A/A_* = -1.93$. The UTC nozzle centerline was canted 6^{o} from the case centerline. The exposed material designations are also shown in the figures. For the 260-SL-1 and 120-SS-1 nozzles, the exposed material in the subsonic region at high area ratios was General Tire V-44 elastomeric insulation over Fiberite MX2646 silica phenolic; in the low area ratio subsonic section, the throat section, the throat extension section, and the exit cone section to $A/A_* = 3.0$ for the 260-SL-1 and to $A/A_* = 3.5$ for the 120-SS-1, the exposed material was Fiberite MX4926 carbon phenolic; in the section making up the remainder of the exit cone the exposed material was U. S. Polymeric FM5131 silica phenolic. In the 260-SL-1 nozzle, all carbon and silica phenolic parts in the subsonic region, throat, and throat extension were autoclave cured at a nominal pressure of 325 psia whereas the comparable parts for the 120-SS-1 nozzle were hydroclave cured. The carbon and silica phenolic exit cone parts in both nozzles were cured using a nylon overwrap. For the UA-1205-10 nozzle, the subsonic and throat region was made up of 6 sections of U. S. Polymeric FM5014 graphite phenolic as the exposed material. In the throat extension the exposed material was also FM5014 graphite phenolic, and in the exit cone the exposed material was Fiberite MX2646 silica phenolic. The type of cure for the UA-1205-10 nozzle parts was not known.

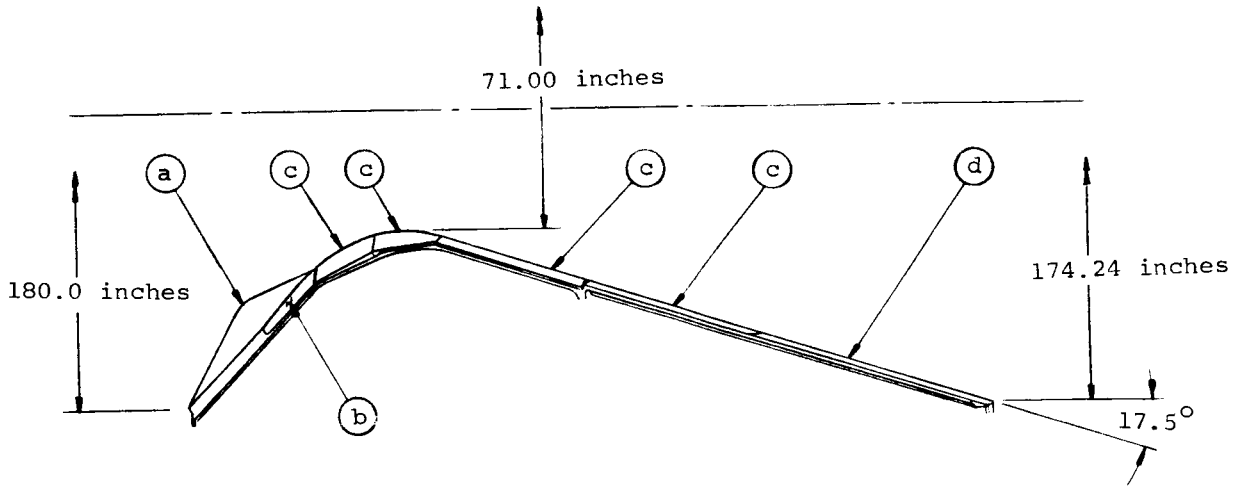

a) V-44 elastomeric

b) MX2646 silica phenolic

c) MX4926 carbon phenolic

d) FM5131 silica phenolic

Figure 1.- Nozzle configuration and exposed materials for the Aerojet 260-SL-1 motor.

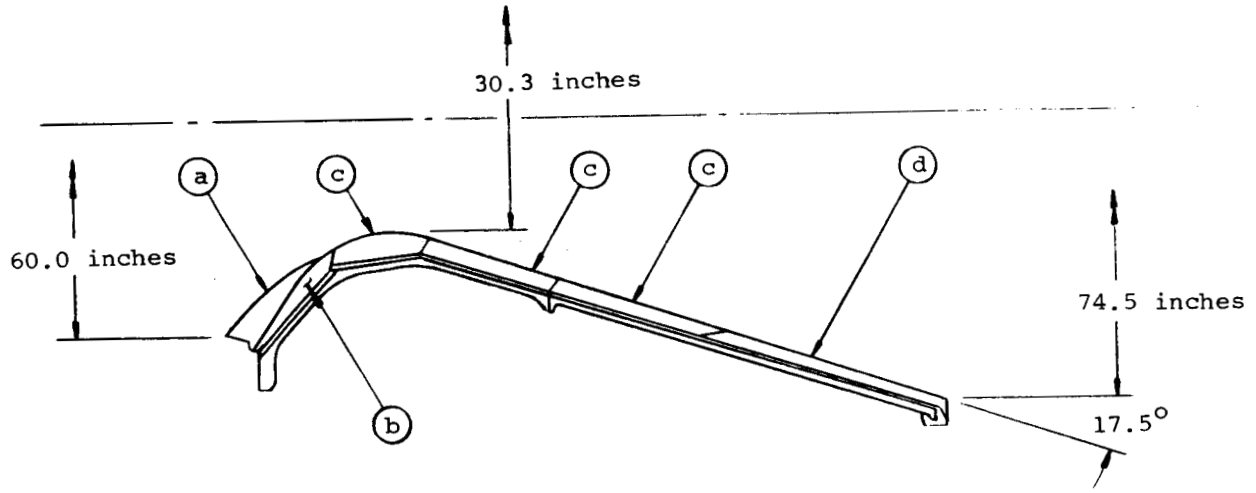

a) V-44 elastomeric

b) MX2646 silica phenolic

c) MX4926 carbon phenolic

d) FM5131 silica phenolic

Figure 2.- Nozzle configuration and exposed materials for the Aerojet 120-SS-1 motor.

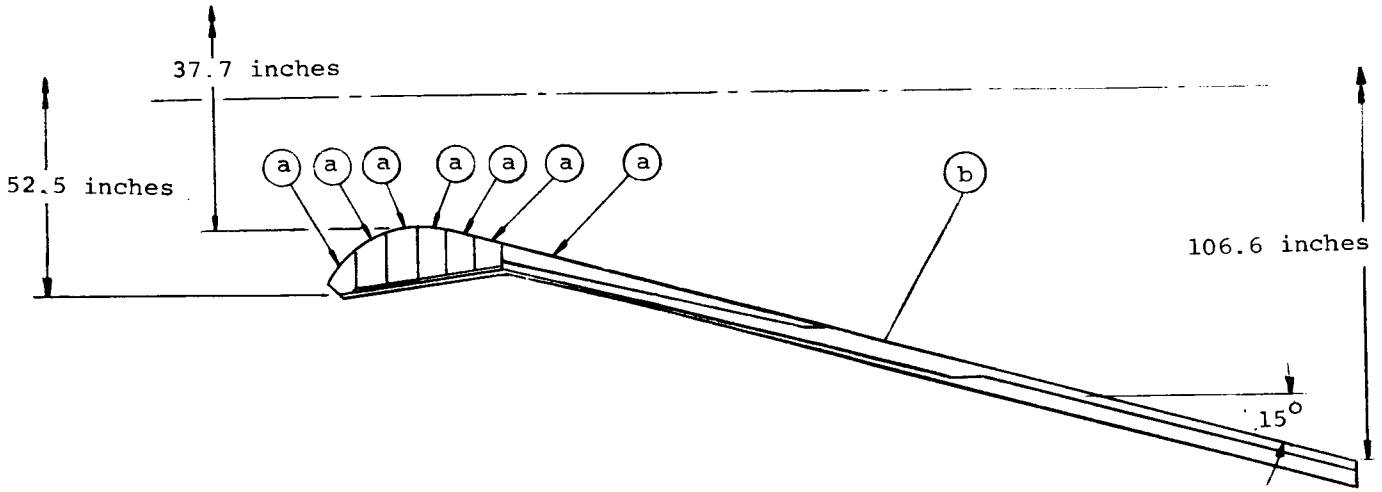

a) FM5014 graphite phenolic
b) MX2646 silica phenolic

Figure 3.- Nozzle configuration and exposed materials for the UTC UA-1205-10 motor.

The locations for which computer program predictions were made and the corresponding materials and layup angles are presented below:

Motor	Area Ratio	Exposed Material	Layup Angle (Referenced to Surface)
260-SL-1	-1.2	MX4926 carbon phenolic	55°
	1.0	MX4926 carbon phenolic	68°
	1.9	MX4926 carbon phenolic	52.5°
	2.5	MX4926 carbon phenolic	17.5°
	3.8	FM5131 silica phenolic	17.5°
120-SS-1	-1.2	MX4926 carbon phenolic	55°
	1.0	MX4926 carbon phenolic	66°
	1.9	MX4926 carbon phenolic	17.5°
	2.7	MX4926 carbon phenolic	17.5°
	4.8	FM5131 silica phenolic	17.5°
UA-1205-10	-1.13	FM5014 graphite phenolic	rosette
	1.0	FM5014 graphite phenolic	rosette
	1.21	FM5014 graphite phenolic	rosette
	1.90	FM4015 graphite phenolic	15°
	3.41	MX2646 silica phenolic	15°

Note: Negative area ratio indicates a subsonic location

These locations were chosen to correspond to stations where surface erosion and char depth measurements were made. The subsonic points were fairly close to the throat because of the above requirement; the area ratio of -1.2 station was the first measurement station downstream of the elastomeric insulation in the Aerojet nozzles and the -1.13 station was the first measurement station in the UTC nozzle. No calculations for stations in the Aerojet motor including the V-44 elastomeric insulation could be made because insufficient material property data were available for the material.

2.3 Prediction Technique

The predictions of ablative material performance were accomplished using the set of two Aerotherm ablation computer programs appropriate to charring materials. The prediction technique is presented below through a discussion of these programs in terms of their functions, information available from them, input information, and their limitations. The computer programs are discussed in Section 2.3.1 and the input information pertinent to the calculations performed herein is presented in Section 2.3.2.

2.3.1 Ablation computer programs

The set of two programs used in the prediction of material performance were the Equilibrium Surface Thermochemistry (EST) Program and the Charring Material Ablation (CMA) Program. The Equilibrium Surface Thermochemistry Program treats the chemical response of a wall material to the combined environment of the boundary-layer-edge gases, the pyrolysis off-gases, and, if applicable, condensed-phase particles. The program assumes chemical equilibrium at the surface; that is, the surface chemical-reaction rates are limited only by the diffusion rates of reactive species to the surface. The input requirement is the basic thermochemical data for all possible gaseous and condensed-phase species in the system of interest, the system pressure, and the elemental compositions of the boundary-layer-edge gases, pyrolysis off-gases, char, and, if applicable, condensed phase particles. The program output is in the form of surface-erosion rate as a function of surface temperature, pyrolysis off-gas rate, and, if applicable, particle-impaction rate. The enthalpy of the gases at the wall is also output. Two program options are available. One treats all gas-phase species as having equal diffusion coefficients, and the other is a general treatment of multicomponent diffusion wherein unequal diffusion coefficients are allowed.

In the calculations presented herein, the equal diffusion coefficient option of the program was used, this also being the case for References 1-3. The more realistic unequal diffusion coefficient option was not used because both options yield very similar erosion predictions[2] for the solid propellant combustion products environment of interest herein and because of the precedence of References 1-3.

The Charring Material Ablation Program calculates the transient response, both surface and in depth, of a charring ablator. The output information at each output time includes erosion depth, char depth, pyrolysis zone depth, surface-recession rate, char recession rate, pyrolysis zone recession rate, surface temperature, internal temperature distribution, and internal density distribution (due to resin and/or reinforcement decomposition). Cooldown after termination of a firing and restart after cooldown can both be treated. Multiple restarts can also be calculated continuously. The input requirements include:

Surface thermochemistry (output of Equilibrium Surface Thermochemistry Program)

[2] As an example, the predicted erosion for the throat of the UTC UA-1205-10 nozzle was 2 percent higher using the unequal diffusion coefficient option than that using the equal diffusion coefficient option.

Material properties

- Specific heat
- Thermal conductivity
- Surface emissivity

} Virgin material and char

- Kinetic constants of resin and, if applicable, reinforcement decomposition

Transfer coefficients (heat transfer coefficient and ratio of mass transfer and heat transfer coefficients)

Incident radiation heat flux

The details of this input are presented in the following section, Section 2.3.2. The program can treat a planar (slab) geometry, an axisymmetric geometry with either an internal or external radius, a spherically symmetric geometry, and a perfectly general specification of heat flow cross-sectional area as a function of depth from the surface, effectively, the definition of a heat flow "stream tube". In all options, the heat flow is assumed to be one-dimensional. Up to six backup materials can be specified, and contact resistance between each can also be specified. In its present form, the program does not consider the decomposition of a backup material. A general back wall boundary condition is allowed; insulated, free or forced convection, radiation, or a combination of the last two.

For all locations considered herein, the approximation of a planar geometry was appropriate and this option was used in the calculations.

Further details on both computer programs are presented in References 6-8.

2.3.2 Input information

The input information to the computer programs and the methods of determining this information for the calculations performed under this contract are discussed in the following sections. The boundary-layer-edge conditions required in the calculation of much of the input for both computer programs are discussed in Section 2.3.2.1. Section 2.3.2.2 discusses the material thermal properties and Section 2.3.2.3 presents the heat-transfer coefficient calculation method.

Before discussing the input information in detail, it should be noted that two predictions were made for each location in each motor; one before the final results of the laboratory experimental program and special studies program were available and one after these results were available and which incorporated them. The primary difference between these two predictions was in char thermal conductivity, the final predictions incorporating the conductivity data derived from the experimental program. The special studies task also resulted in a change in the calculation of heat transfer coefficient for the case of an ablating wall. The effect of blowing at the surface, due to the pyrolysis off-gases and the products of char consumption, on reducing heat and mass transfer coefficient was found to be larger than assumed in the earlier calculations. This

correction, together with the rather arbitrary but convenient assumption of Prandtl number equal unity, allowed the elimination of the one element of empiricism in generating the input to the computer programs. The empirical 0.8 constant multiplier on the boundary layer computer program transfer coefficient output (See Section 2.3.2.3) used in the initial material performance predictions of this contract and the predictions of References 1 and 3 was eliminated. These changes are discussed in detail in the appropriate section, Section 3.5.1 and Section 4.1.3.

2.3.2.1 Boundary-layer-edge conditions

The boundary-layer-edge conditions are required for the calculation of surface thermochemistry, convective heat-transfer coefficient, recovery enthalpy, and free-stream radiative heat flux, all of which are inputs for the charring ablation calculation. The calculation procedures to define these edge conditions at each location for analysis are discussed below.

The first step in the determination of edge conditions was the calculation of propellant enthalpy from the given chamber temperature and pressure and the propellant elemental composition. An early version of the Chemical Equlibrium (ACE) Program was used for this calculation.

An isentropic expansion from average measured chamber pressure (web time average) and at the calculated enthalpy was then calculated for each motor using the ACE Program. The calculations were performed for the area ratios analyzed; the boundary-layer-edge conditions of temperature, enthalpy pressure, velocity, and molecular composition were defined at these locations. Calculations were also performed at intermediate locations to smoothly define the variation with running length, this being required for the boundary-layer calculation of heat-transfer coefficient. Note that the calculations were performed for the average chamber pressures, whereas the actual chamber pressures varied significantly during the firings; the effect on the boundary-layer-edge molecular compositions should not be appreciable however (Reference 3), and the effect on the other edge variables should be negligible.

For the throat and supersonic locations, no condensed phase particles would be expected to penetrate the boundary layer; for the subsonic location, the particle-impaction rate is unknown and may actually be zero also. Because of this, a gas-phase-only composition was used at all locations for calculation of surface thermochemistry and heat-transfer coefficients. Condensed phase alumina (the only condensed phase present) was therefore eliminated from the molecular composition determined from the expansion calculations and the appropriate gas phase-only elemental composition defined. The boundary-layer-edge temperature, pressure, and velocity were assumed to be defined by the expansion calculation

which, of course, included the condensed phase. This temperature and pressure and the gas-phase-only composition then defined the enthalpy and molecular weight which, all together, defined the boundary layer edge conditions.

To facilitate calculations, the gas-phase-only elemental composition was assumed constant at the value at the throat for all calculation locations; this composition actually varied slightly with location due to the increasing fraction of condensed phase alumina with distance downstream.

The recovery enthalpy was calculated from

$$h_r = h_e + R \frac{u_e^2}{2} \tag{1}$$

where R is the recovery factor, equal to $Pr^{1/3}$ for turbulent flow.

In all calculations, a stream emissivity of unity with radiation at the local static temperature was assumed. The sizes of the motors were felt to be sufficient to make these assumptions valid; the particle cloud would have sufficient depth to be essentially opaque and particle temperature lag effects would be small. The radiation heat flux was therefore calculated from the equation

$$q_r = \epsilon \sigma T_e^4 \tag{2}$$

where $\epsilon = 1.0$.

2.3.2.2 Material properties

The compositions and thermophysical properties of the exposed materials are required in the calculation of surface thermochemistry (composition only) and of material thermal response and ablation. This information is presented below for the materials considered in the predictions presented herein.

A summary of the compositions and thermal properties used in the prediction is presented in Table I. These data were the same for both the initial and the final predictions except for the char thermal conductivity. The final char conductivity is presented in Table Ia and the initial assumed conductivity is presented in Table Ib. Note that the conductivity data, both virgin material and char, are for the extremes in layup angle, 0° and 90°. The input conductivities at intermediate layup angles were calculated from

$$k = k_{0^\circ} \left[1 + \left(\frac{k_{90^\circ}}{k_{0^\circ}} - 1 \right) \sin \theta \right] \tag{3}$$

where θ is the layup angle referenced to a tangent to the surface. The background and sources of the data presented in Table I are reviewed below.

TABLE I. COMPOSITION AND PROPERTIES OF SEVERAL COMPOSITE ABLATIVE MATERIALS

a) Final

Material	Nominal Density lb/ft^3	Nominal Resin Fraction	Resin Residual	Assumed Resin Elemental Formula	Reinf. Elemental Formula	Temp. $^\circ$R	Virgin Material: Spec. Heat Btu/lb $^\circ$R	Virgin Material: Thermal Cond. Btu/ft sec $^\circ$R x 10^4 0° Layup	Virgin Material: Thermal Cond. Btu/ft sec $^\circ$R x 10^4 90° Layup	Virgin Material: Emissivity	Char: Spec. Heat Btu/lb $^\circ$R	Char: Thermal Cond. Btu/ft sec $^\circ$R x 10^4 0° Layup	Char: Thermal Cond. Btu/ft sec $^\circ$R x 10^4 90° Layup	Char: Emissivity
MX4926 carbon phenolic	89.4	0.345	0.40	C_6H_6O	C	530	0.210	1.39	2.36	0.85	0.210	1.83	3.11	0.85
						800	.360	1.58	2.69	.85	-	-	-	.85
						1000	-	-	-	.85	.430	1.90	3.15	.85
						1160	.360	1.83	3.11	.85	-	-	-	.85
						1500	.472	1.83	3.11	.85	.472	1.95	3.20	.85
						2000	.484	1.83	3.11	.85	.484	2.35	4.15	.85
						3000	.493	1.83	3.11	.85	.493	5.40	8.95	.85
						4000	.498	1.83	3.11	.85	.498	11.65	14.70	.85
						5000	.500	1.83	3.11	.85	.500	18.80	21.25	.85
						6000	.500	1.83	3.11	.85	.500	26.50	28.35	.85
MX4500 graphite phenolic[b]	87.5	0.340	0.40	C_6H_6O	C	530	.240	2.04	6.12	.85	.210	2.32	6.96	.85
						800	.340	2.16	6.48	.85	-	-	-	.85
						1000	-	-	-	.85	.430	2.90	7.65	.85
						1160	.390	2.32	6.96	.85	-	-	-	.85
FM5014 graphite phenolic[b]	89.1	0.345	0.40	C_6H_6O	C	1500	.472	2.32	6.96	.85	.472	3.80	8.65	.85
						2000	.484	2.32	6.96	.85	.484	5.00	9.85	.85
						3000	.493	2.32	6.96	.85	.493	8.60	13.15	.85
						4000	.498	2.32	6.96	.85	.498	13.80	17.30	.85
						5000	.500	2.32	6.96	.85	.500	19.90	22.80	.85
						6000	.500	2.32	6.96	.85	.500	27.10	29.60	.85
FM5131 silica phenolic	108.2	0.325	0.50	C_6H_6O	SiO_2	530	.260	.76	.91	.85	.210	.85	1.02	.85
						1000	-	.76	.91	.85	.430	.85	1.15	.85
						1160	.310	.76	.91	.85	-	-	-	.85
						1500	.472	.76	.91	.85	.472	.90	1.35	.85
						2000	.484	.76	.91	.85	.484	1.00	1.60	.85
						3000	.493	.76	.91	.85	.493	1.60	2.60	.85
						4000	.498	.76	.91	.85	.498	3.40	5.00	.85
						5000	.500	.76	.91	.85	.500	7.35	9.10	.85
						6000	.500	.76	.91	.85	.500	13.55	14.45	.85
MX2646 silica phenolic	118.3	0.205	0.50	C_6H_6O	SiO_2	530	.190	.46	.74	.85	.210	.60	.96	.85
						760	.255	.51	.82	.85	.430	.60	.96	.85
						1000	-	-	-	.85	.430	.60	.96	.85
						1160	-	.60	.96	.85	-	-	-	.85
						1500	.472	.60	.96	.85	.472	.60	1.05	.85
						2000	.484	.60	.96	.85	.484	.65	1.20	.85
						3000	.493	.60	.96	.85	.493	.70	1.60	.85
						4000	.498	.60	.96	.85	.498	1.50	2.90	.85
						5000	.500	.60	.96	.85	.500	4.35	6.00	.85
						6000	.500	.60	.96	.85	.500	9.65	10.70	.85

a) To account for the effect of layup angle, the following equation is suggested

$$k = K_{0^\circ}\left[1 + \left(\frac{k_{90^\circ}}{k_{0^\circ}} - 1\right)\sin\theta\right]$$

where θ is the layup angle referenced to a tangent to the surface.

b) The thermal properties of MX4500 and FM5014 graphite phenolics were assumed to be the same.

TABLE I. CONCLUDED

b) Initial [a]

Material	Temp. $^{\circ}R$	Char Thermal Cond. Btu/ft sec $^{\circ}R$ x 10^4		Material	Temp. $^{\circ}R$	Char Thermal Cond. Btu/ft sec $^{\circ}R$ x 10^4	
		0° Layup	90° Layup			0° Layup	90° Layup
MX4926 carbon phenolic	530	2.05	3.49	FM5131 silica phenolic	530	0.85	1.02
	1000	2.18	3.71		1000	.91	1.09
	1500	2.33	3.96		1500	.97	1.16
	2000	2.48	4.22		2000	1.03	1.24
	3000	2.81	4.78		3000	1.17	1.40
	4000	3.18	5.41		4000	1.32	1.58
	5000	3.68	6.26		5000	1.53	1.84
	6000	4.47	7.60		6000	1.86	2.23
FM5014 graphite phenolic	530	2.32	6.96	MX2646 silica phenolic	530	0.60	0.96
	1000	3.40	7.90		1000	1.40	1.70
	1500	4.60	9.05		1500	2.25	2.60
	2000	5.90	10.25		2000	3.20	3.55
	3000	8.65	12.95		3000	5.60	5.90
	4000	12.00	16.20		4000	8.70	8.90
	5000	16.30	20.50		5000	13.30	13.30
	6000	22.90	26.80		6000	20.80	20.80

[a]All compositions and properties but char thermal conductivity were the same for both initial and final predictions.

TABLE II

PHENOLIC RESIN DECOMPOSITION KINETIC CONSTANTS

Reaction, i	Pre-exponential Factor B (sec^{-1})	Activation Energy Factor E_a/R ($^{\circ}R$)	Density Factor Exponent ψ	Initial Density ρ_o (lb/ft^3)	Residual Density ρ_r (lb/ft^3)
A	1.40×10^4	15,400	3	20.25	0
B	4.48×10^9	36,800	3	60.75	32.40[a] 40.50[b]

[a]Resin residual = 0.40

[b]Resin residual = 0.50

The densities and resin fractions were taken from the manufacturers' specifications. The resin residual (the fraction of resin left behind as part of the char after pyrolysis is complete) was estimated from the results of Reference 6. The resin elemental formulas represent only the relative mole composition of the elements making up the resins; the formula used is the accepted composition for a standard phenolic resin. The virgin material specific heat and thermal conductivity for MX4926 carbon phenolic and FM5131 silic phenolic were obtained directly from Reference 9.[3] For FM5014 graphite phenolic and MX2646 silica phenolic, these properties were estimated from References 9-11. These virgin material property data are available up to 1160°R (700°F), the temperature above which material decomposition occurs. For purposes of input to the computer program, these data were extrapolated to high temperature; the thermal conductivity at 1160°R was assumed to be representative of that at high temperature and therefore a constant value was used for 1160°R on up and the specific heat above 1160°R was assumed to be equal to the char specific heat. The char specific heat was assumed to be the same for all materials and was obtained from Reference 12. The char thermal conductivity for MX4926 carbon phenolic was taken directly from the experimental program results obtained under this contract (Table Ia). The char thermal conductivity for FM5014 graphite phenolic was assumed to be equivalent to that for MX4500 graphite phenolic and was also taken directly from the experimental program results (Table Ia). The char conductivity for the silica phenolics, FM5131 and MX2646, was estimated based on consideration of the virgin material conductivity, the resin fraction, and char conductivity variations for the carbon and graphite phenolics. The surface emissivity of the char and the virgin material was assumed to be constant at 0.85 for all materials.

In characterizing resin decomposition, two parallel, kinetically controlled reactions of the form

$$\frac{\partial \rho_i}{\partial \theta} = B_i e^{-E_{a_i}/RT} \rho_{o_i} \left(\frac{\rho_i - \rho_{r_i}}{\rho_{o_i}} \right)^{\psi_i} \tag{4}$$

[3] The virgin material specific heat of MX4926 carbon phenolic was also measured in the Aerotherm thermal properties laboratory. The specific heat from these tests was slightly higher than that of Reference 9.

where

$$\frac{\partial \rho}{\partial \theta} = \sum_i \frac{\partial \rho_i}{\partial \theta} \tag{5}$$

are treated in the computer calculation. The constants of Equation (4) were not available for the specific phenolic resins used in the materials considered. The constants of Reference 13 for 91LD phenolic, which are appropriate to the actual resins as well, were therefore used and are presented in Table II.

2.3.2.3 Transfer coefficients

The heat-transfer coefficient as a function of firing time at each location for analysis is a required input to the Charring Material Ablation Program. The input values are computed for a nonablating wall, and the correction for local blowing due to surface chemical reactions and pyrolysis off-gases is done internal to the program. The heat-transfer coefficient also defines the mass-transfer coefficient through a Chilton-Colburn type analogy

$$\rho_e u_e C_M = \rho_e u_e C_H \, Le^{2/3} \tag{6}$$

which is the relation used in the computer program. In keeping with the analyses of References 1 and 3, the Lewis number was taken as 1.0.

The actual calculation of heat-transfer coefficient was accomplished using the method of Appendix A, Reference 6. This method, termed the energy thickness method, is based on a general boundary-layer analysis and is an integral solution of the boundary-layer energy equation. The method was originally programmed for real air, but has recently been generalized to allow consideration of any gaseous environment for the specific purpose of calculating rocket nozzle heat-transfer coefficients (Reference 3). The details of the method and program are not presented here, but are available in References 3 and 6.

The program input was the thermodynamic properties for the gas-phase-only edge gas and, as a function of surface running length from the start of the boundary layer, x, the boundary-layer-edge pressure, velocity, and enthalpy, the local nozzle radius, the wall enthalpy, and the Prandtl number. Also, the boundary-layer transition criterion was input as a transition Reynolds number on momentum thickness of 200 for the two Aerojet nozzles. Because of the abrupt entry in the UTC nozzle, the boundary layer was assumed to be turbulent throughout. For the sake of simplicity, calculations were performed at three wall enthalpies corresponding to surface temperatures of 530°R, 4200°R, 5200°R and

to account for the effect of propellant grain regression through the firing, at boundary layer starting locations corresponding to three (for the 260-SL-1 and 120-SS-1 nozzles) or four (for the UA-1205-10 nozzle) times through the firing. The input to the Charring Material Ablation Program therefore accounted for the effects of variable wall temperature and propellant regression through the firings. The pressures at which calculations were made corresponded to the web time average chamber pressure. The input was also corrected for the effect of variable pressure through the firings by the following equation (Reference 2)

$$\rho_e u_e C_H = (\rho_e u_e C_H)_{calc} \left[\frac{p_c}{(p_c)_{web\ ave.}} \right]^{0.8} \tag{7}$$

In the calculation of heat transfer coefficient for the initial predictions, the Prandtl number was taken as 0.8 and the calculated heat transfer coefficients were multiplied by an empirical 0.8 factor for input to the charring ablation calculation. This factor and the use of the 0.8 Prandtl number was derived from the study of References 2 and 3. The correction of the non-ablating wall heat transfer coefficient input to the Charring Material Ablation Program, for the effect of blowing at the wall is accomplished internal to the program through the following equation

$$\rho_e u_e C_H = (\rho_e u_e C_H)_i \frac{\Phi}{e^{\Phi}-1} \tag{8}$$

where

$$\Phi = 2\lambda \dot{B} = 2\lambda \frac{\dot{m}_c + \dot{m}_g}{(\rho_e u_e C_H)_i} \tag{9}$$

and i refers to the input value. In the initial predictions, λ was taken as 0.2 consistent with previous calculations (References 1-3). An analysis performed under the special studies task of this contract revealed that for turbulent flow the blowing parameter, λ, should be 0.4 (see Section 4.1), however, not the 0.2 value used previously. This new value was therefore used in the final predictions. Also, because of a desire to eliminate the one empirical constant used in generating the input to the charring ablation calculation, the 0.8 multiplier on the calculated heat transfer coefficient was eliminated in the final calculations. Finally, a somewhat arbitrary and simplifying assumption of a Prandtl number equal 1.0 rather than 0.8 was made for the final

calculation of input heat transfer coefficient. Note that this Prandtl number change also affects the recovery enthalpy, Equation (1).

The final calculated heat transfer coefficients for the 260-SL-1, 120-SS-1, and UA-1205-10 nozzles are presented as a function of firing time in Figures 4-6 for all locations for which predictions were made.

2.4 Predicted and Measured Material Performance

2.4.1 Presentation of results

The predictions of material performance, and wherever possible, the corresponding measured performance, are presented in Figures 7-15 and Tables III-VI. The content of these figures and tables is summarized below:

	260-SL-1	120-SS-1	UA-1205-10	Figure Content
Figure	7	10	13	Predicted and measured surface erosion depths through the range of area ratios for which predictions were made
Figure	8	11	14	Predicted surface erosion and char depths at the throat through the firing and cooldown, and comparable post-fire measurements
Figure	9	12	15	Predicted internal temperature and density distributions at the throat for three times during the firing and cooldown
Table	III	IV	V	Predicted and measured surface erosion and char depths at the area ratios for which predictions were made
Table	VI			Predicted maximum depths of the 500°F isotherm, and actual material thicknesses used at the area ratios for which predictions were made

In Figures 7, 10, and 13 and in Figures 8 and 9, the initial as well as the final predictions are presented to allow an assessment of the effects of the improved input information on the predictions and their comparison with measurement. It should be noted that the most significant variable between the initial and final predictions is char thermal conductivity. In all other figures and in the tables, the final predictions only are presented. The transient response of the materials and the internal property distributions (Figure 8, 11, and 14 and Figures 9, 12, and 15, respectively) are presented for the throat only;

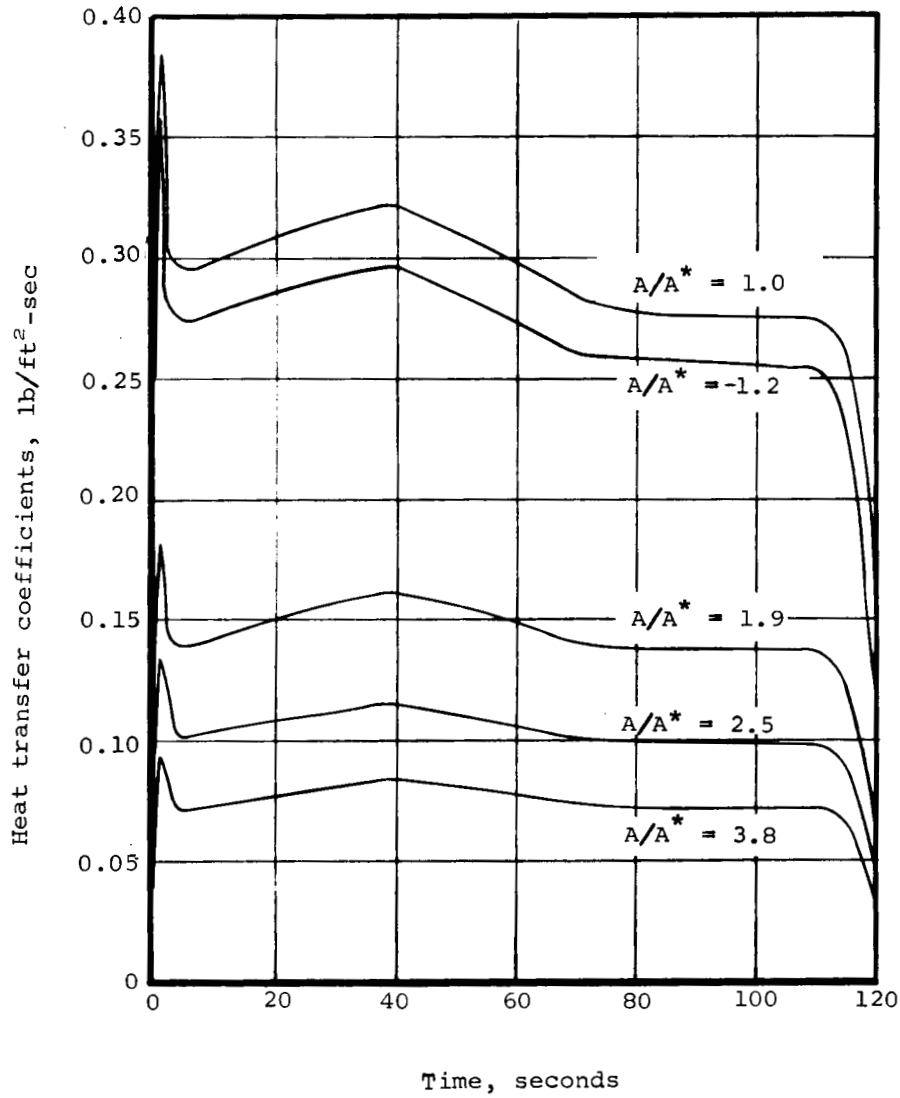

Figure 4.- Calculated heat transfer coefficients for the 260-SL-1 nozzle.

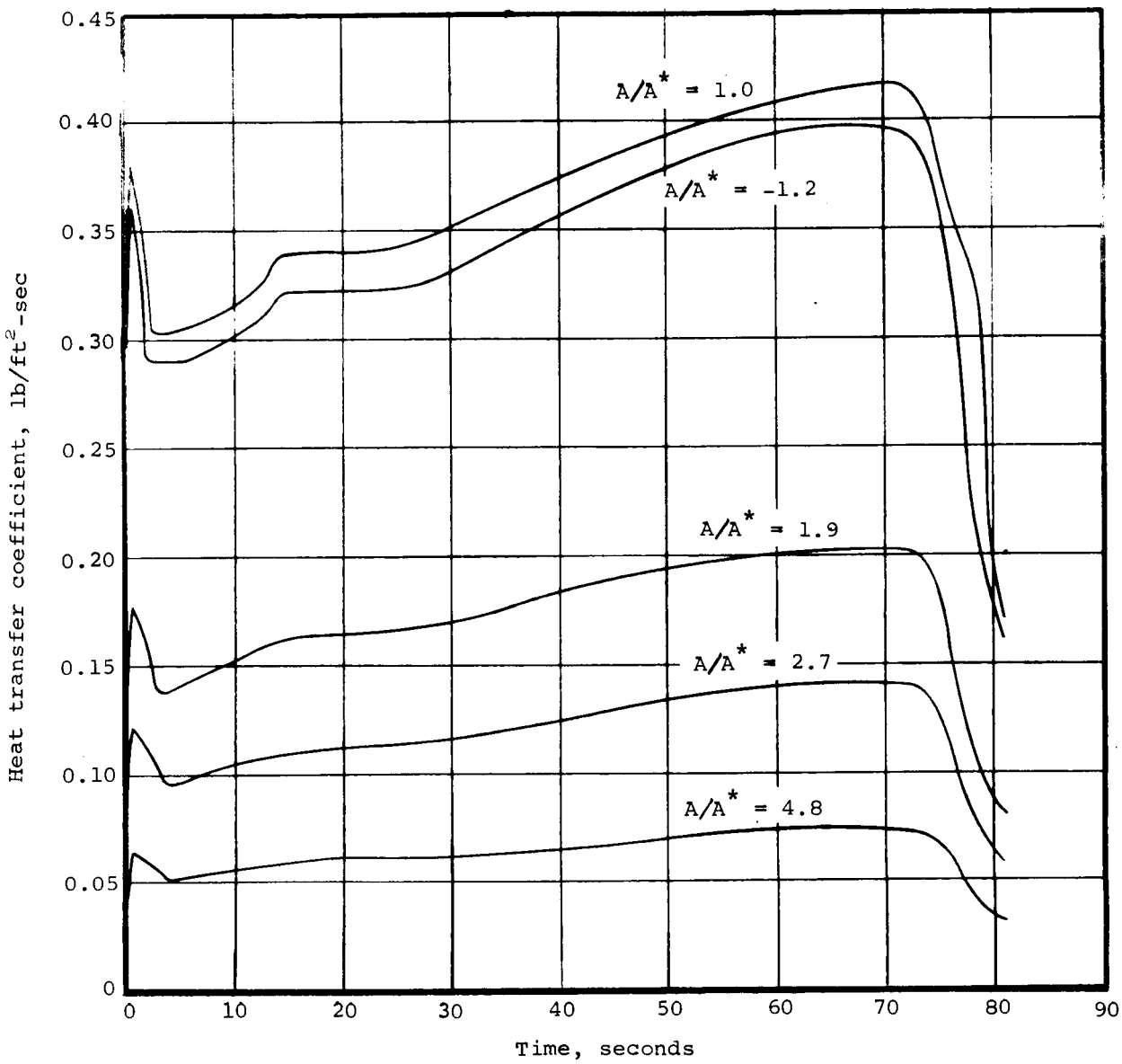

Figure 5.- Calculated heat transfer coefficients for the 120-SS-1 nozzle.

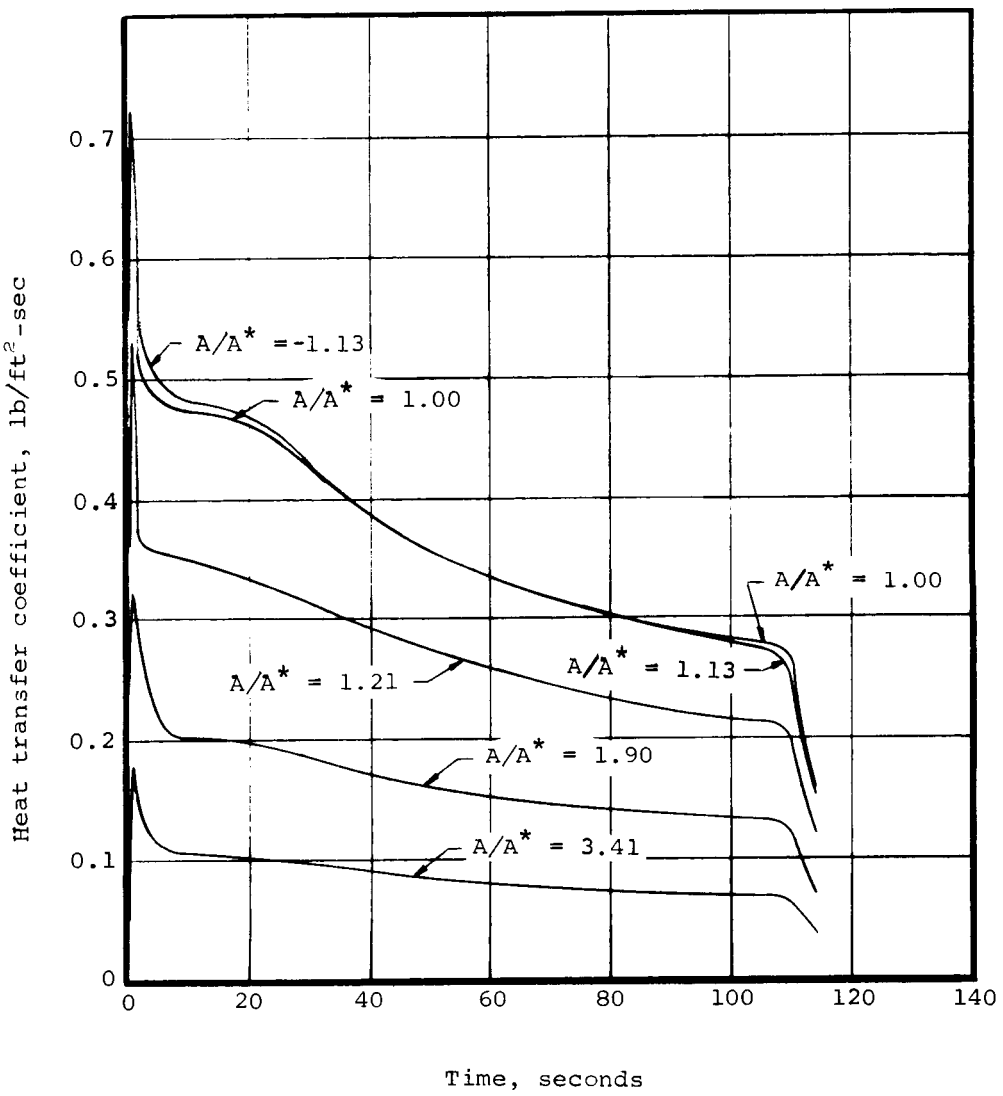

Figure 6.- Calculated heat transfer coefficients for the UA-1205-10 nozzle.

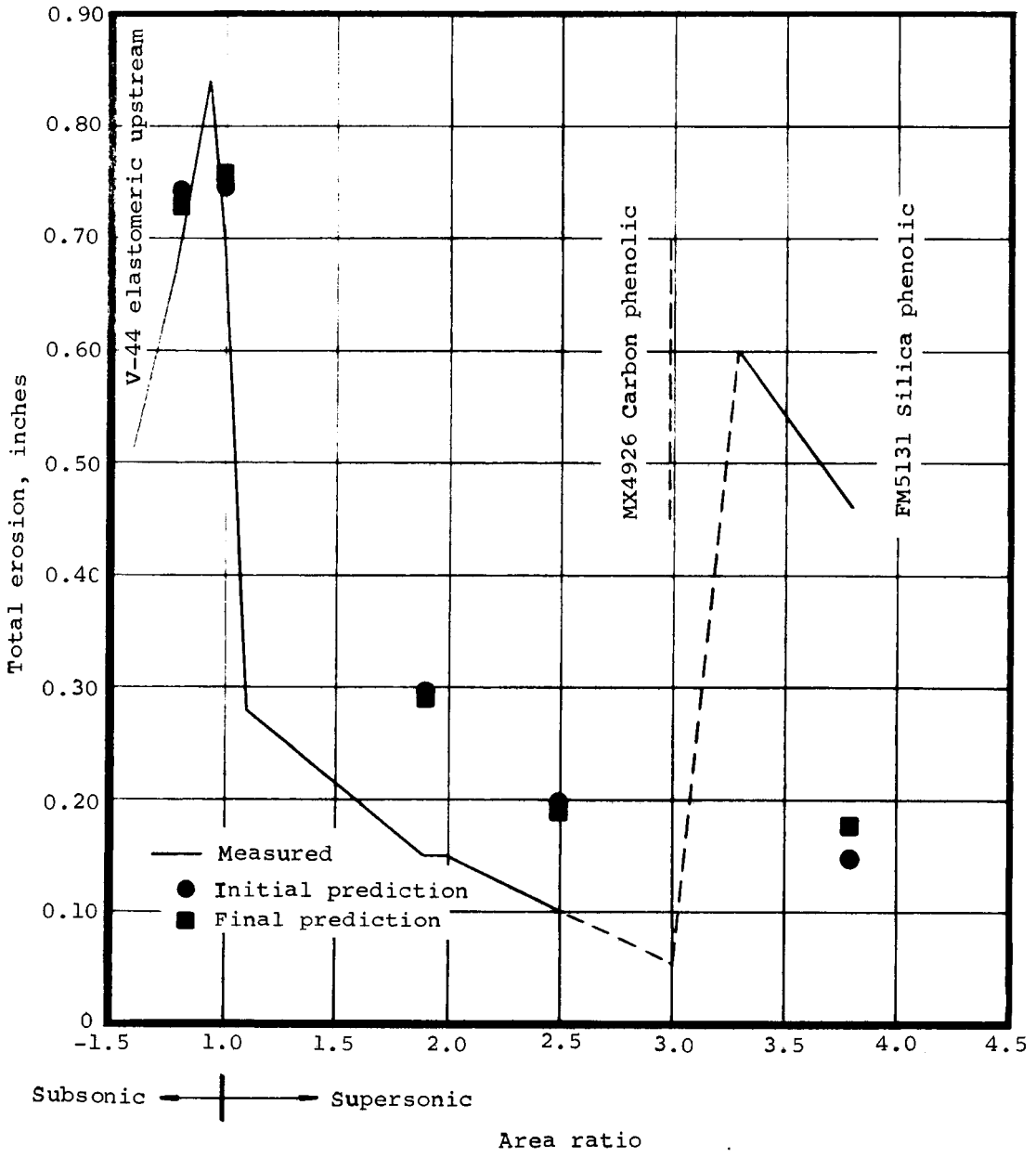

Figure 7.- Predicted and measured erosion depths for the 260-SL-1 nozzle.

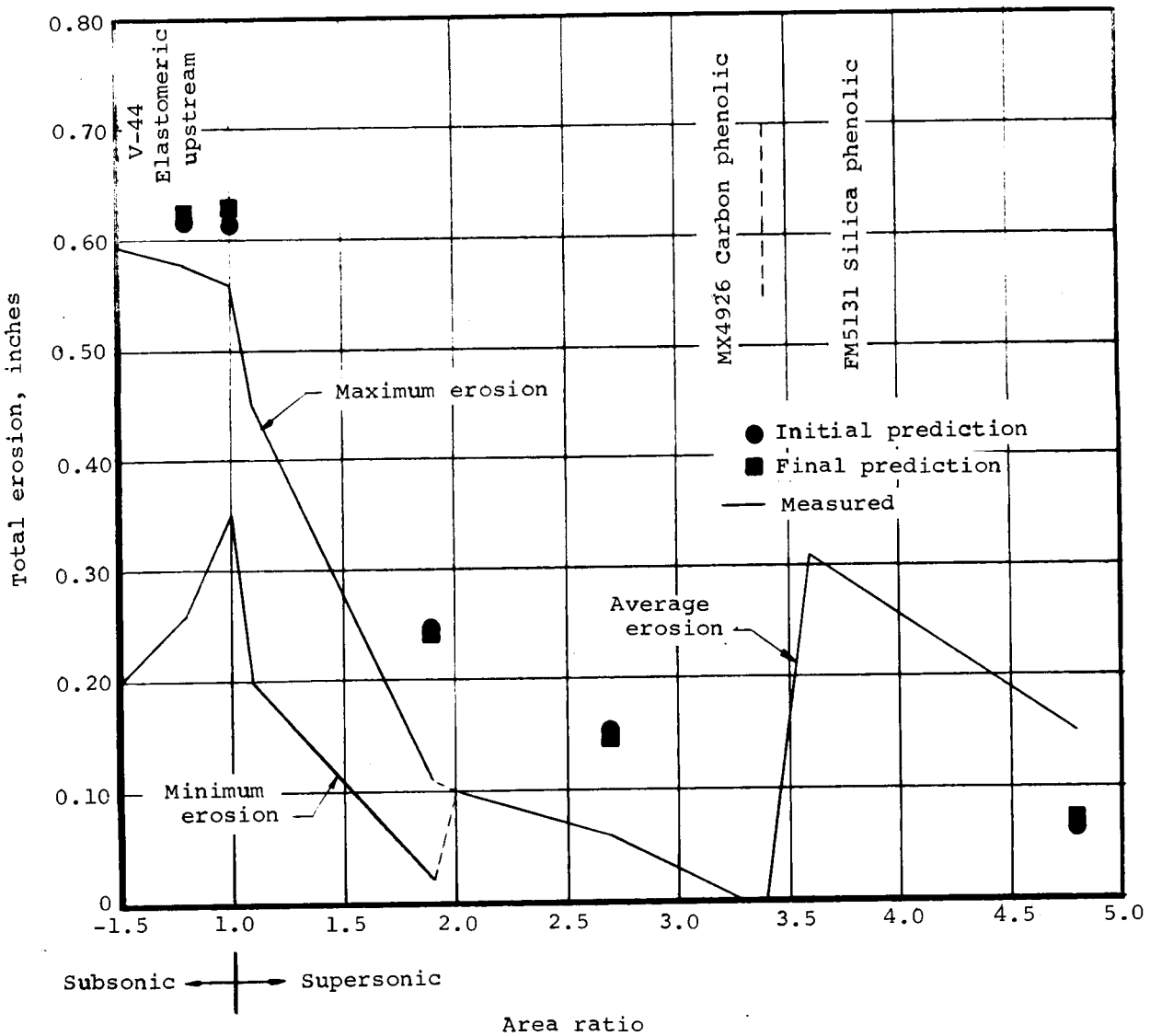

Figure 8.- Predicted and measured erosion depths for the 120-SS-1 nozzle.

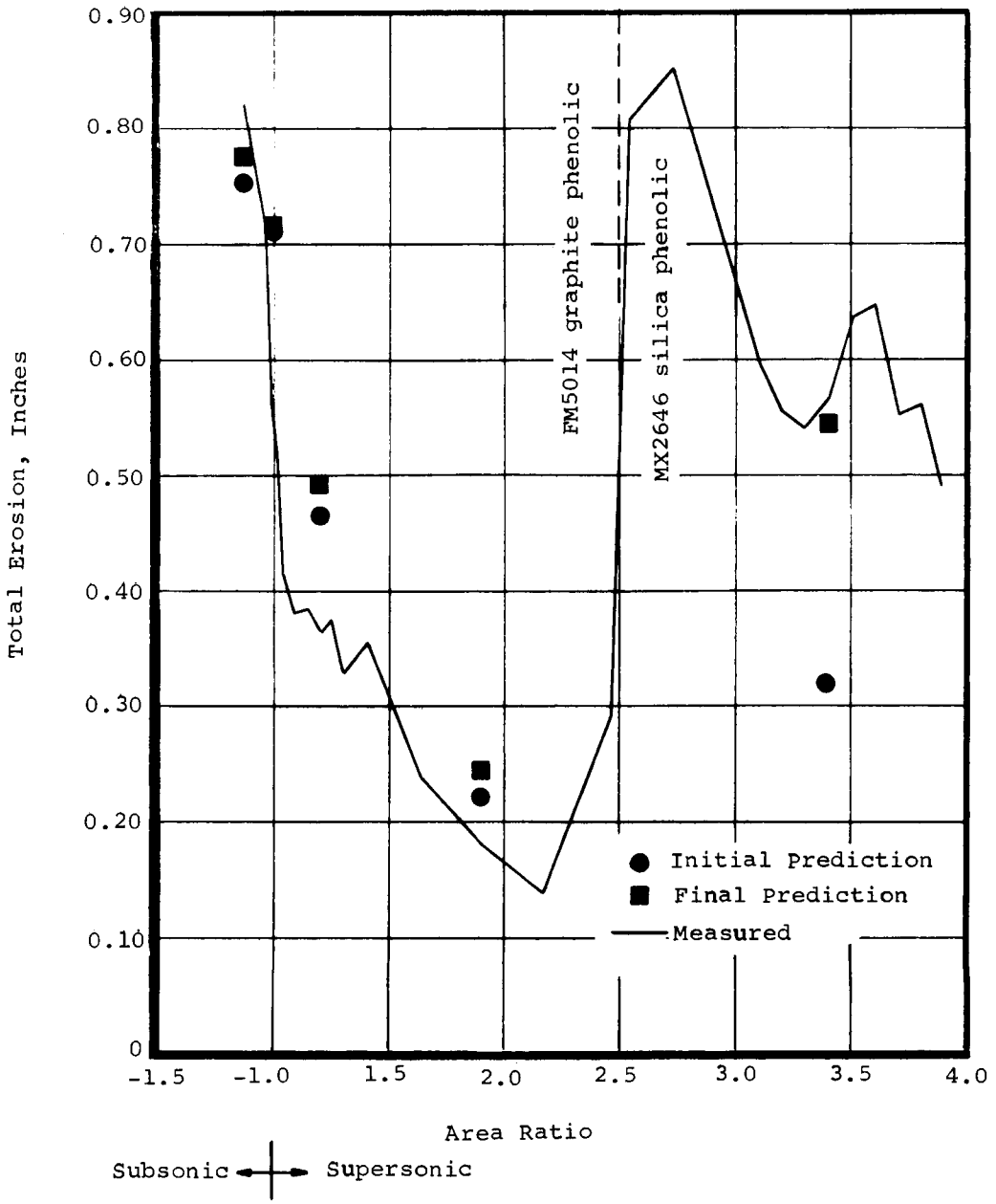

Figure 9.- Predicted and measured erosion depths for the UA-1205-10 nozzle.

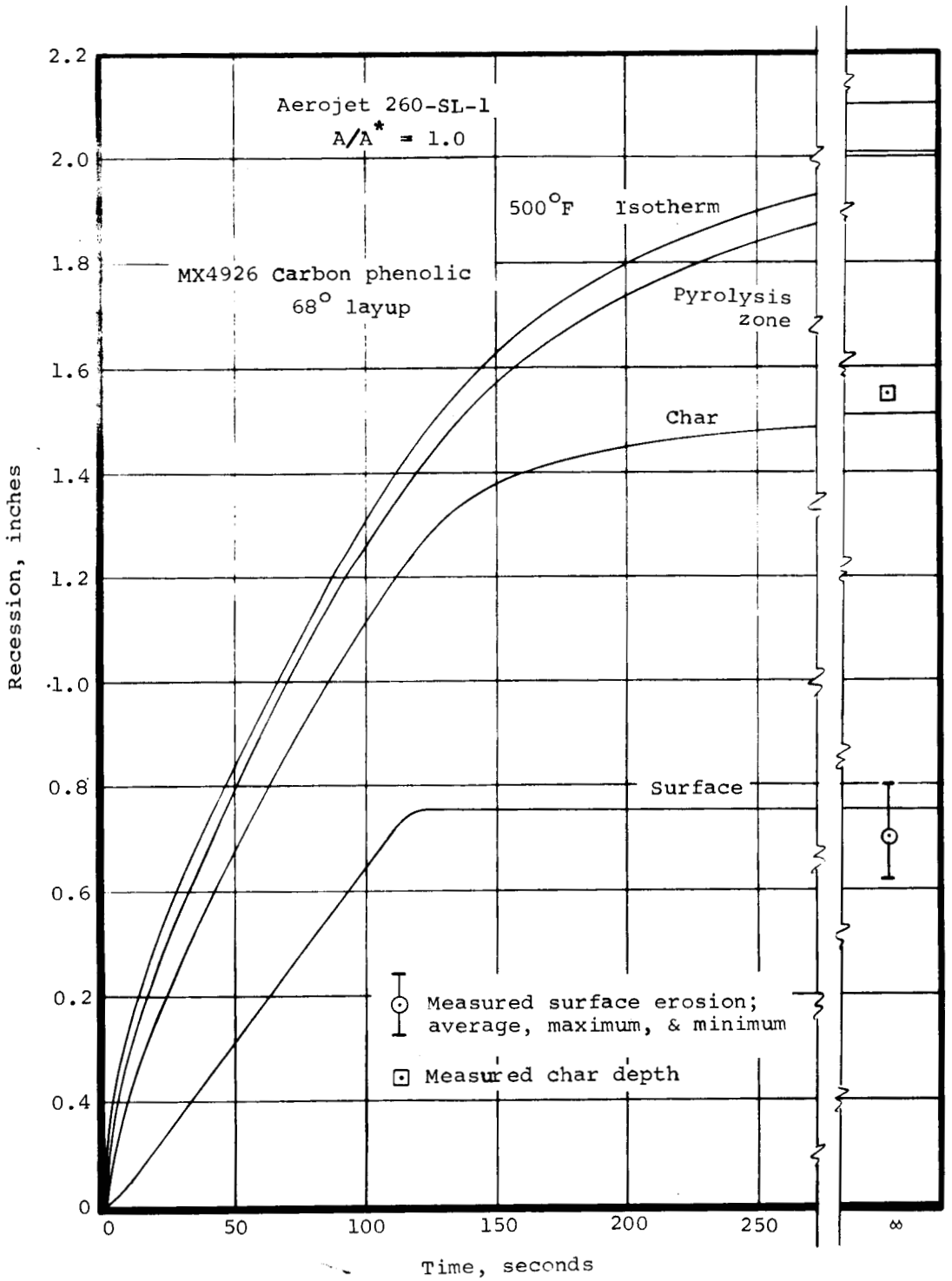

a) Final prediction

Figure 10.- Predicted transient response of the throat material for the 260-SL-1 nozzle and comparison with post-fire measurement.

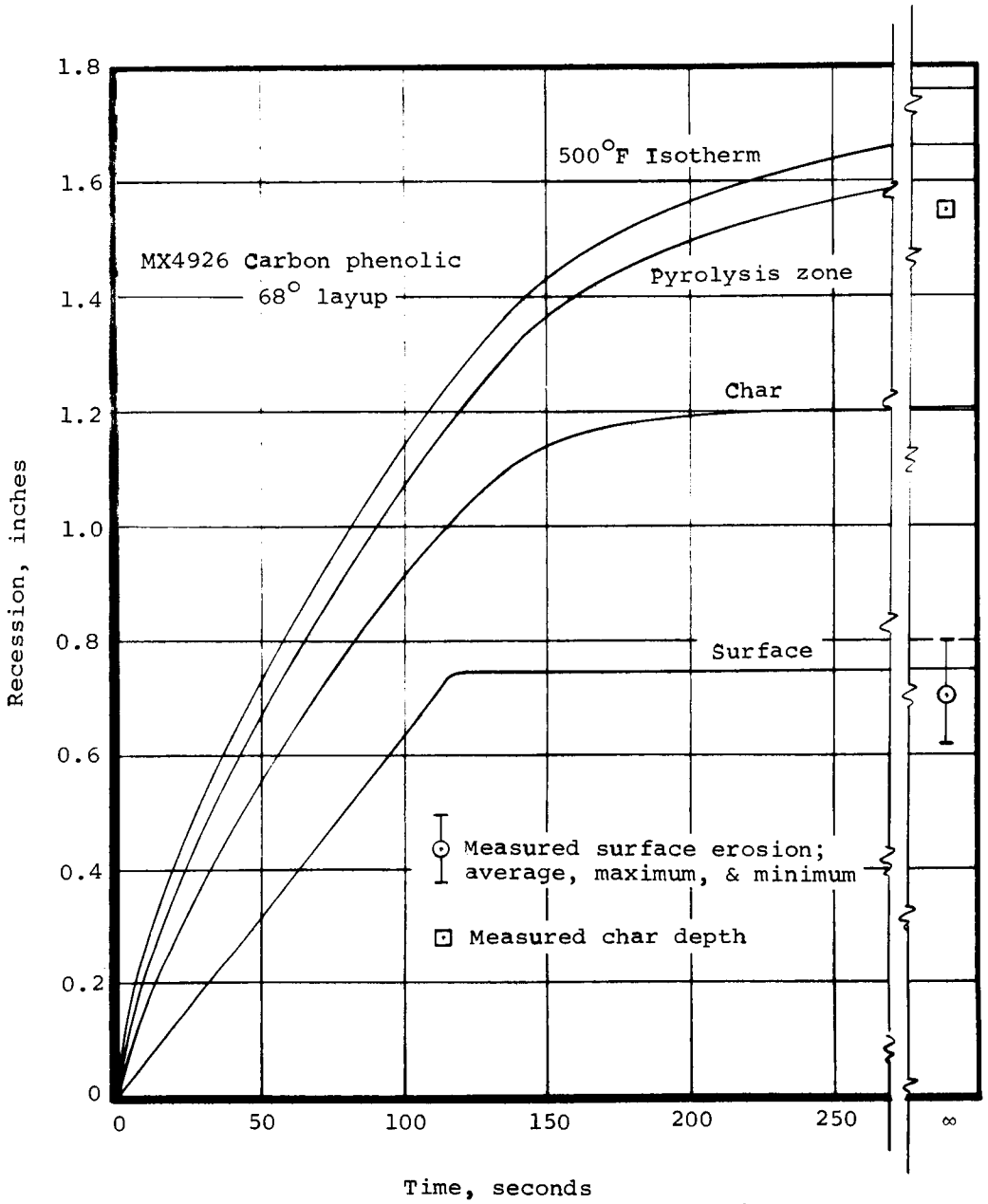

b) Initial prediction

Figure 10.- Concluded.

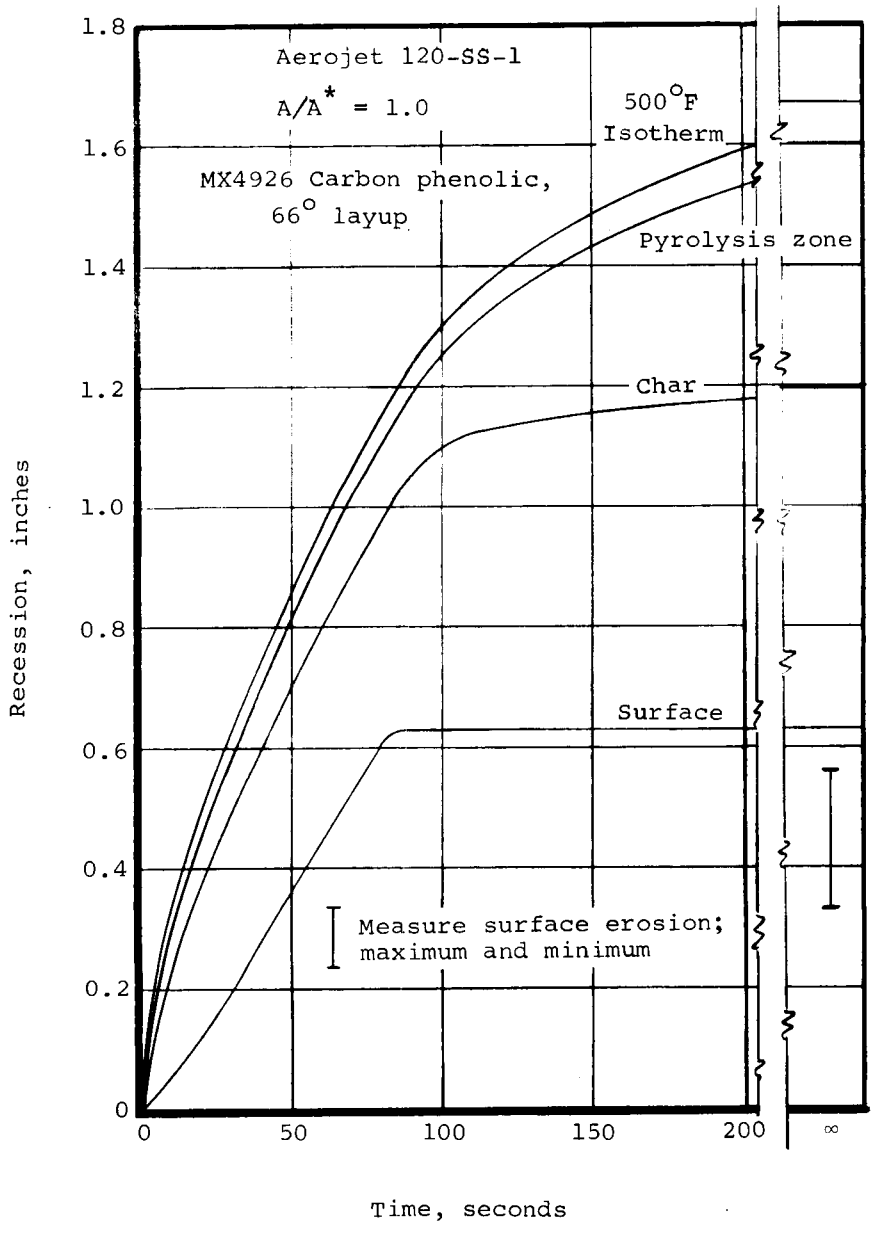

Figure 11.- Predicted transient response of the throat material for the 120-SS-1 nozzle and comparison with post-fire measurement.

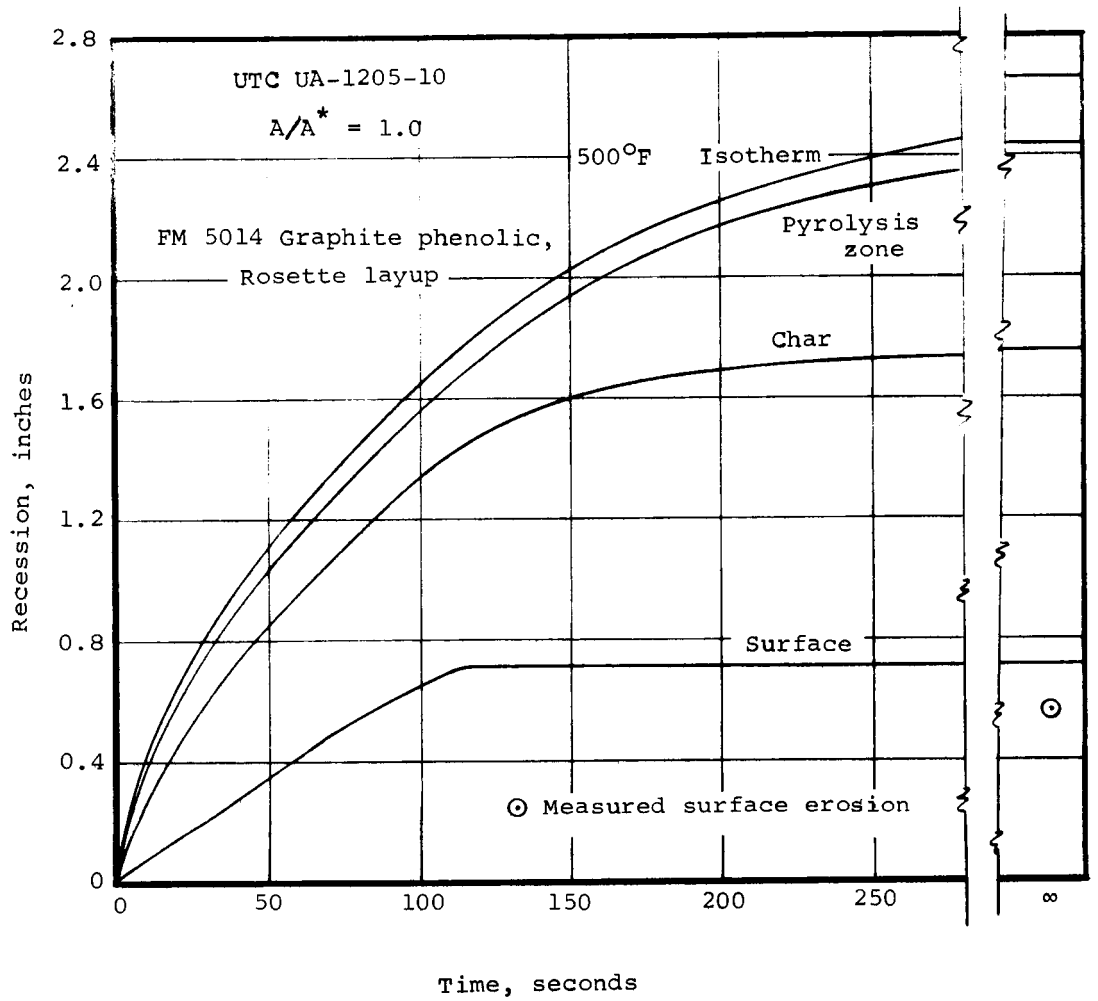

Figure 12.- Predicted transient response of the throat material for the UA-1205-10 nozzle and comparison with post-fire measurement.

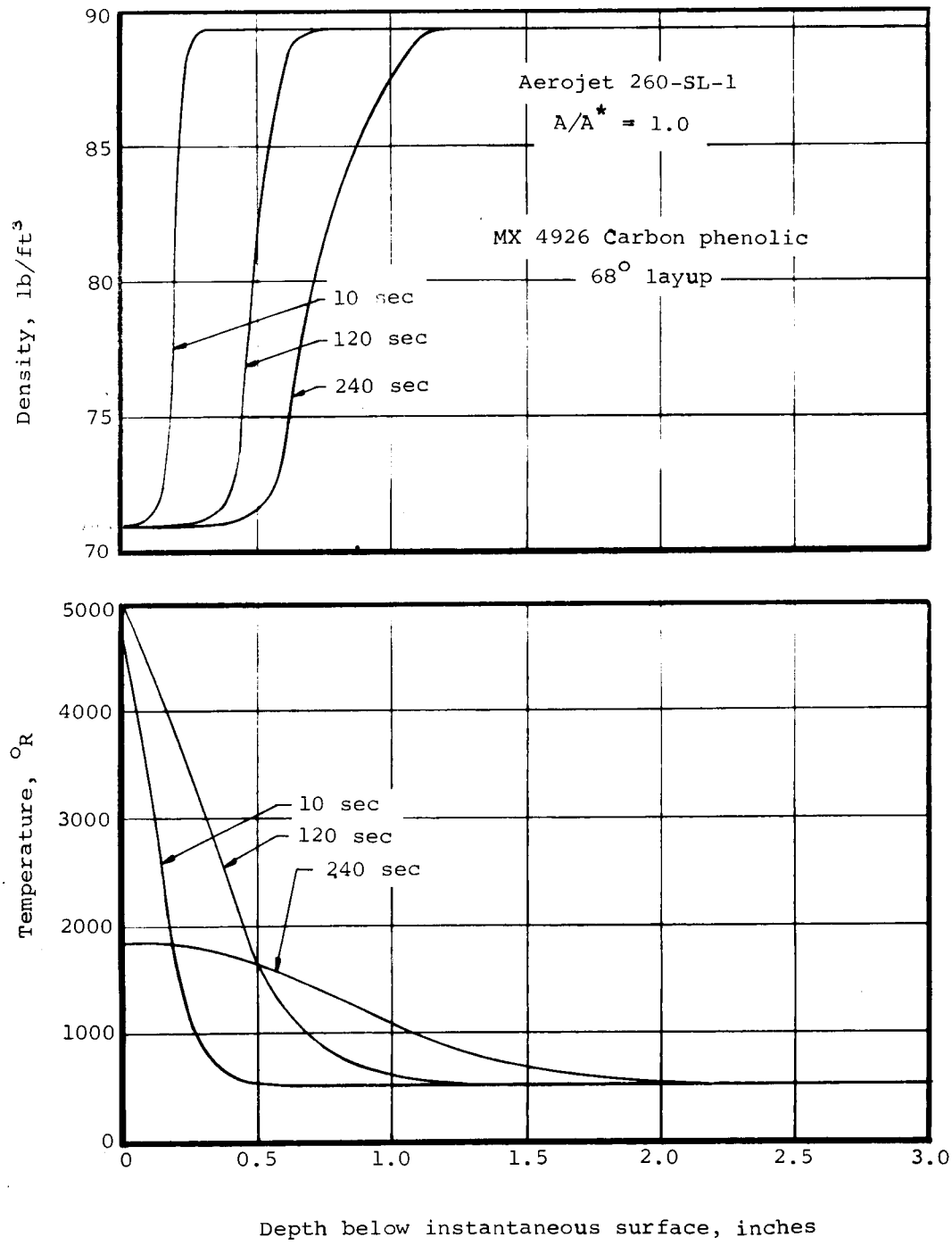

a) Final prediction

Figure 13.- Predicted temperature and density distributions for the throat of the 260-SL-1 nozzle.

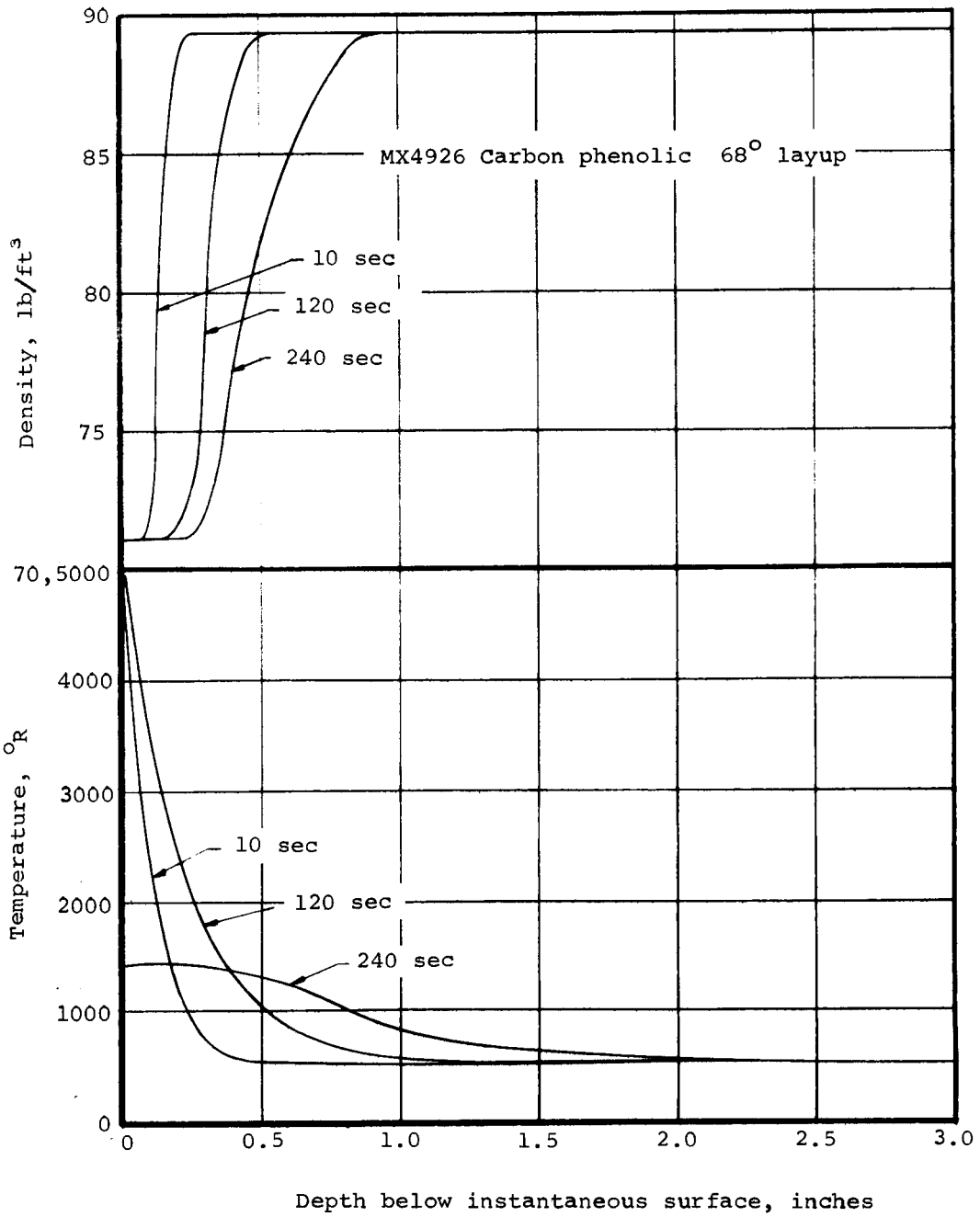

b) Initial prediction

Figure 13.- Concluded.

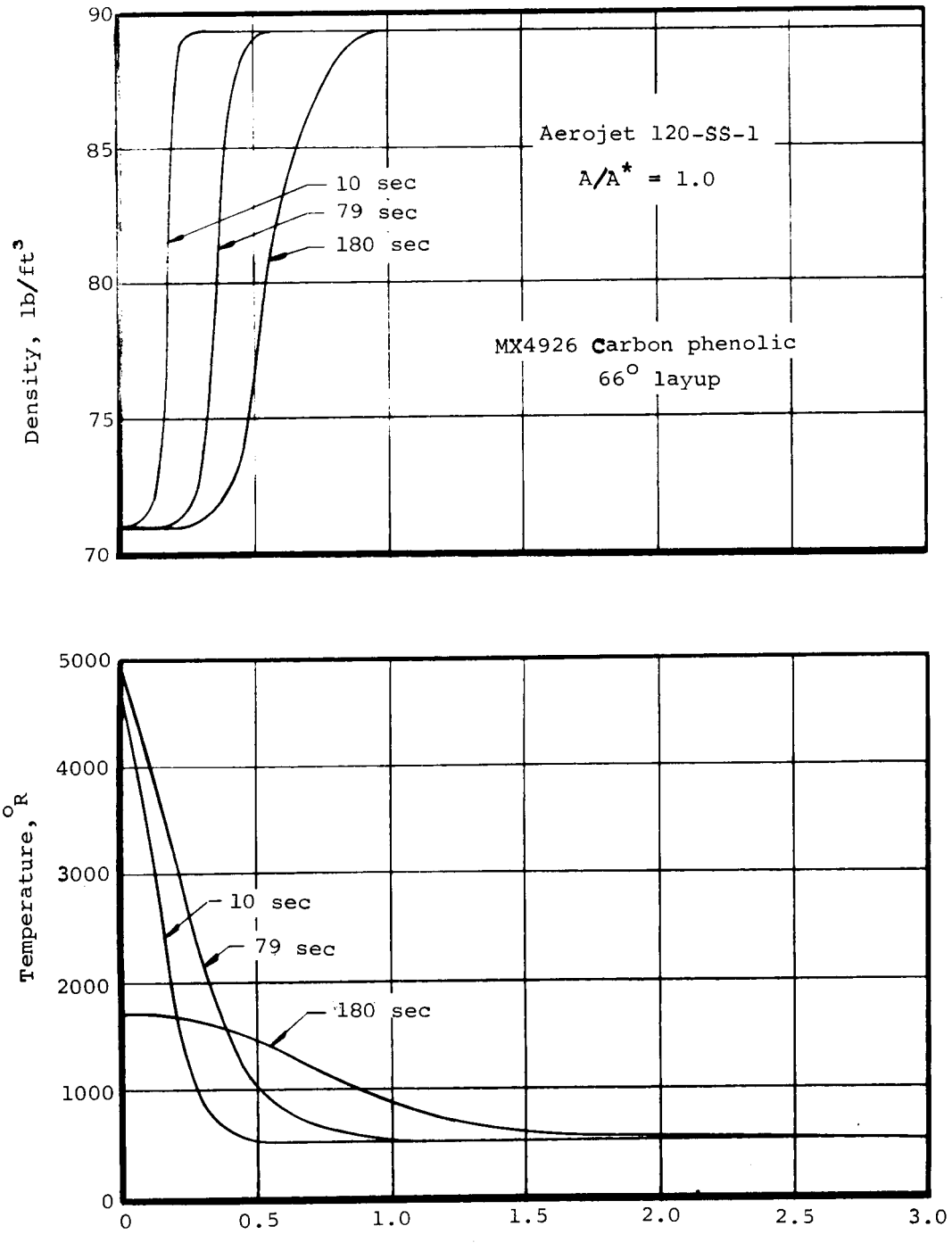

Figure 14.- Predicted temperature and density distributions for the throat of the 120-SS-1 nozzle.

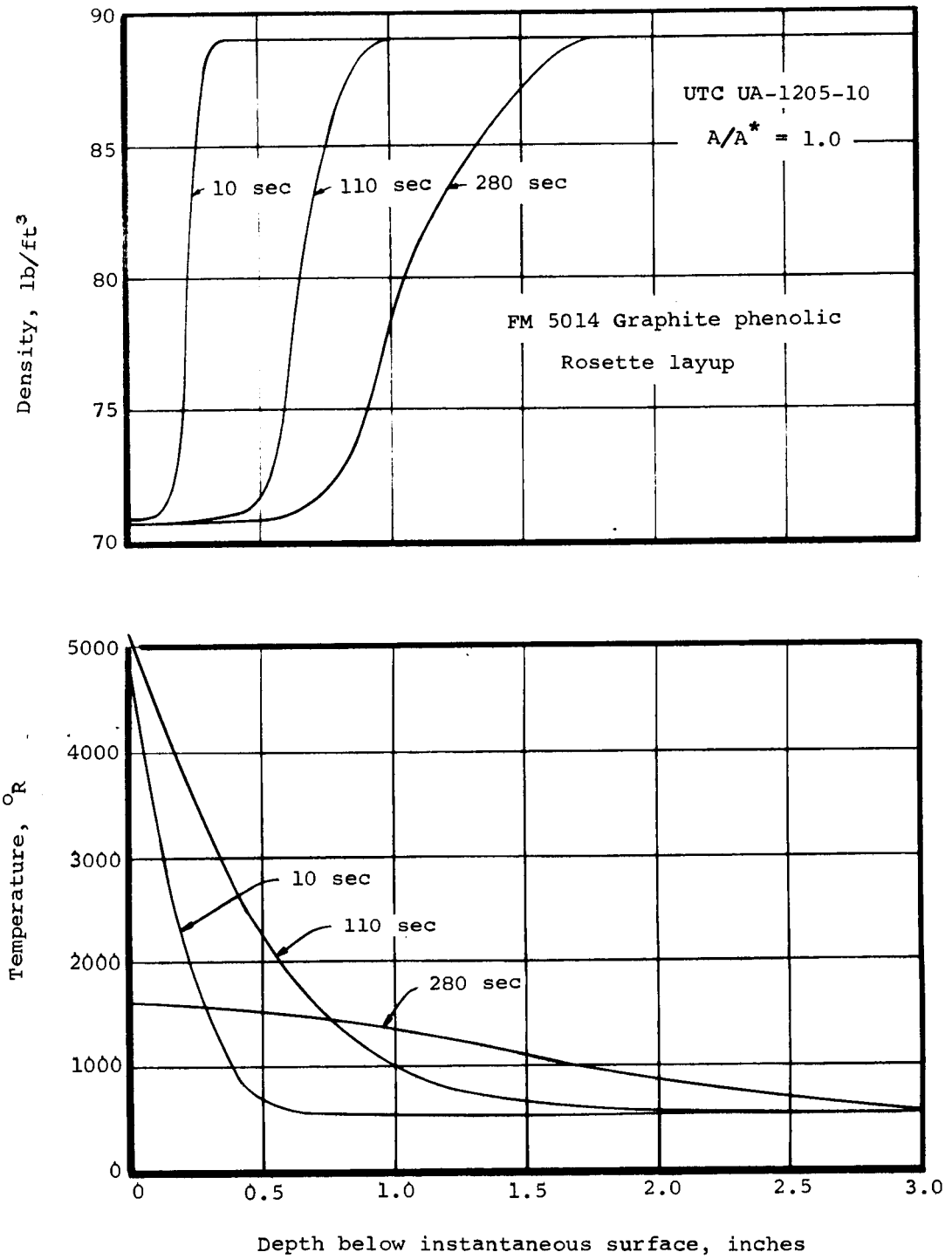

Figure 15- Predicted temperature and density distributions for the throat of the UA-1205-10 nozzle.

TABLE III. PREDICTED AND MEASURED SURFACE EROSION DEPTHS, CHAR DEPTHS, AND CHAR THICKNESSES FOR THE AEROJET 260-SL-1 NOZZLE

Nozzle Throat Dia. in.	Average Chamber Pressure psia[a]	Web Time sec	Area Ratio[b]	Material and Layup Angle[c]	Surface Erosion Depth in.		Char in.			
							Depth		Thickness	
					Meas.	Pred.	Meas.	Pred.	Meas.	Pred.
71.0	533	114	-1.2	MX4926 carbon phenolic, 55°	.67	.731	1.47	1.55	.80	.82
			1.0	MX4926 carbon phenolic, 68°	.70	.757	1.55	1.51	.85	.75
			1.9	MX4926 carbon phenolic, 52.5°	.15	.291	1.00	1.15	.85	.86
			2.5	MX4926 carbon phenolic, 17.5°	.10	.192	.85	.96	.75	.77
			3.8	FM5131 silica phenolic, 17.5°	.46	.177	.88	.55	.42	.37

a) Based on web time
b) Minus sign indicates a subsonic area ratio
c) Layup angle referenced to surface

TABLE IV. PREDICTED AND MEASURED SURFACE EROSION DEPTHS, CHAR DEPTHS, AND CHAR THICKNESSES FOR THE AEROJET 120-SS-1 NOZZLE

Nozzle Throat Dia. in.	Average Chamber Pressure psia[a]	Web Time sec	Area Ratio[b]	Material and Layup Angle[c]	Surface Erosion Depth in.		Char in.			
							Depth		Thickness	
					Meas.	Pred.	Meas.	Pred.	Meas.	Pred.
30.3	519	74.4	-1.2	MX4926 carbon phenolic, 55°	.58/.26[d]	.616	-	1.22	1.11	.60
			1.0	MX4926 carbon phenolic, 66°	.56/.33[d]	.629	-	1.20	1.03	.57
			1.9	MX4926 carbon phenolic, 17.5°	.11/.02[d]	.244	-	.87	.60	.63
			2.7	MX4926 carbon phenolic, 17.5°	.06	.148	.56	.75	.50	.60
			4.8	FM5131 silica phenolic, 17.5°	.15	.071	.65	.40	.50	.43

a) Based on web time
b) Minus sign indicates a subsonic area ratio
c) Layup angle referenced to surface
d) Maximum and minimum erosion, respectively

TABLE V. PREDICTED AND MEASURED SURFACE EROSION DEPTHS, CHAR DEPTHS, AND CHAR THICKNESSES FOR THE UTC UA-1205-10 NOZZLE

Nozzle Throat Dia. in.	Average Chamber Pressure psia[a]	Web Time sec	Area Ratio[b]	Material and Layup Angle[c]	Surface Erosion Depth in.		Char in.			
							Depth		Thickness	
					Meas.	Pred.	Meas.	Pred.	Meas.	Pred.
37.7	520	109.2	-1.13	FM5014 graphite phenolic, ros.	.822	.778	-	1.93	-	1.15
			1.00	FM5014 graphite phenolic, ros.	.561	.715	-	1.68	-	.97
			1.21	FM5014 graphite phenolic, ros.	.365	.493	-	1.62	-	1.13
			1.90	FM5014 graphite phenolic, 15°	.181	.245	-	1.23	-	.98
			3.41	MX2646 silica phenolic, 15°	.568	.545	-	.74	-	.19

a) Based on web time
b) Minus sign indicates a subsonic area ratio
c) Layup angle referenced to surface, ros. = rosette layup

TABLE VI. PREDICTED DEPTHS OF THE 500°F ISOTHERM AND ACTUAL MATERIAL THICKNESSES FOR THE THREE MOTORS

Motor	Area Ratio[a]	Material and Layup Angle[b]	Actual Exposed Material Thickness, in. (approximate)	Depth of 500°F Isotherm, in.	
				End of Firing	Maximum During Cooldown
260-SL-1	-1.2	MX4926 carbon phenolic, 55°	5.00	1.45	2.27
	1.0	MX4926 carbon phenolic, 68°	4.50	1.46	2.10
	1.9	MX4926 carbon phenolic, 52.5°	2.75	1.15	1.99
	2.5	MX4926 carbon phenolic, 17.5°	1.75	0.97	1.56
	3.8	FM5131 silica phenolic, 17.5°	1.75	0.58	0.90
120-SS-1	-1.2	MX4926 carbon phenolic, 55°	2.50	1.15	1.73
	1.0	MX4926 carbon phenolic, 66°	3.15	1.16	1.67
	1.9	MX4926 carbon phenolic, 17.5°	2.15	0.85	1.26
	2.7	MX4926 carbon phenolic, 17.5°	1.50	0.76	1.12
	4.8	FM5131 silica phenolic, 17.5°	1.50	0.43	0.66
UA-1205-10	-1.13	FM5014 graphite phenolic, ros.	7.50	1.81	3.20
	1.00	FM5014 graphite phenolic, ros.	7.50	1.79	2.70
	1.21	FM5014 graphite phenolic, ros.	5.00	1.64	3.00
	1.90	FM5014 graphite phenolic, 15°	3.00	1.24	2.50
	3.41	MX2646 silica phenolic, 15°	5.15	0.75	0.98

a) Minus sign indicates a subsonic area ratio
b) Layup angle referenced to surface, ros. = rosette layup

these results are typical of the other locations considered and, for all locations, the post-fire results are presented in Tables III-VI. Note that the materials descriptions and the firing conditions are included in Tables III-V. Also note that the predicted performance in terms of char depth and other internal response variables assumed no quench. Quenches, where used, were sufficiently late in the cooldown period that they had little or no effect on the internal response. This is discussed further in Section 4.3.

2.4.2 Discussion

The thermal performance of an ablative material may be conveniently divided into two categories, the surface erosion performance and the insulation performance, the former dictating nozzle contour dimension changes and both dictating the material thickness requirements. The analysis of material performance and the evaluation of the computer programs for predicting this performance must consider both categories. This analysis and evaluation is presented in the following sections for all locations considered in the 260-SL-1, 120-SS-1, and UA-1205-10 nozzles. Surface erosion performance is considered first and performance variables indicative of insulation performance are then considered. Section 2.4.2.1 discusses the predicted and measured surface erosion depths. The char depths and the insulation performance in general are discussed in Section 2.4.2.2. Finally, other information pertinent to material performance is discussed in Section 2.4.2.3.

2.4.2.1 Surface erosion depth

The comparisons of the final predicted and the measured erosion depths for the three nozzles are summarized below from Figure 7, 10, and 13 and Tables III-V.

260-SL-1

Area Ratio	Material	Comparison
-1.2	MX4926 Carbon phenolic	Favorable
1.0	MX4926 carbon phenolic	Favorable
1.9	MX4926 carbon phenolic	Prediction a factor of 2 high
2.5	MX4926 carbon phenolic	Prediction a factor of 2 high
3.8	FM5131 silica phenolic	Prediction a factor of almost 3 low

120-SS-1

Area Ratio	Material	Comparison
-1.2	MX4926 carbon phenolic	Favorable with maximum measured
1.0	MX4926 carbon phenolic	Favorable with maximum measured
1.9	MX4926 carbon phenolic	Prediction a factor of over 2 high

120-SS-1 (continued)

Area Ratio	Material	Comparison
2.7	MX4926 carbon phenolic	Prediction a factor of over 2 high
4.8	FM5131 silica phenolic	Prediction a factor of 2 low

UA-1205-10

Area Ratio	Material	Comparison
-1.13	FM5014 graphite phenolic	Favorable
1.0	FM5014 graphite phenolic	Favorable, predictions slightly high
1.21	FM5014 graphite phenolic	Favorable, predictions slightly high
1.90	FM5014 graphite phenolic	Favorable, predictions slightly high
3.41	MX2646 silica phenolic	Favorable

The UTC nozzle exhibits a generally favorable comparison throughout. For the Aerojet nozzles, however, there are two regions of significant discrepancies, the carbon phenolic in the throat extension and exit cone and the silica phenolic in the exit cone. The causes of these discrepancies are discussed below, followed by a general discussion of the comparisons.

Based on the favorable comparison of predicted and measured erosion depths for the carbon phenolic subsonic and throat regions of the 260-SL-1 nozzle (Figure 7), the major discrepancy in the throat extension and exit cone for this same material was unexpected. After evaluating a number of possibilities, the probable cause for the overprediction was revealed by post-test examination of the sectioned nozzle of the 120-SS-1 motor. [4] A layup angle warp in the char region that resulted in a lower apparent erosion depth was noted in the throat extension and exit cone and probably also occurred at the same locations (the same carbon phenolic material) for the 260-SL-1 nozzle. This warping was not noted in the throat region where the layup angle was large, 66°. The phenomenon is illustrated in Figure 16 and results in the measured erosion being significantly less than that which would have actually occurred in its absence. The physical explanation of the phenomenon is open to conjecture. Possible explanations include a high cross-ply thermal expansion at high temperature and a resultant warp to relieve the induced stress, high internal pressure due the pyrolysis gas generation in depth and a resultant warp to provide a large flow area to relieve this pressure, or perhaps a phenomenon associated with rapid cooling at shutdown.

The underprediction of the surface erosion depths for silica phenolic in both Aerojet nozzles (Figures 7 and 10) is felt to be due to one or more of three possibilities:

[4] An inspection of the 260-SL-1 nozzle was not performed under the contract.

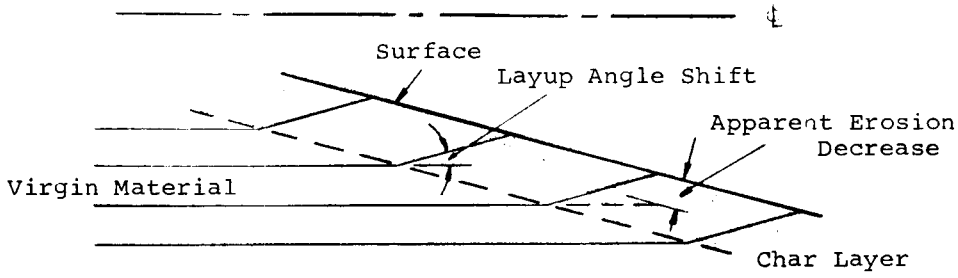

Figure 16.- Schematic of char layup angle warp phenomenon.

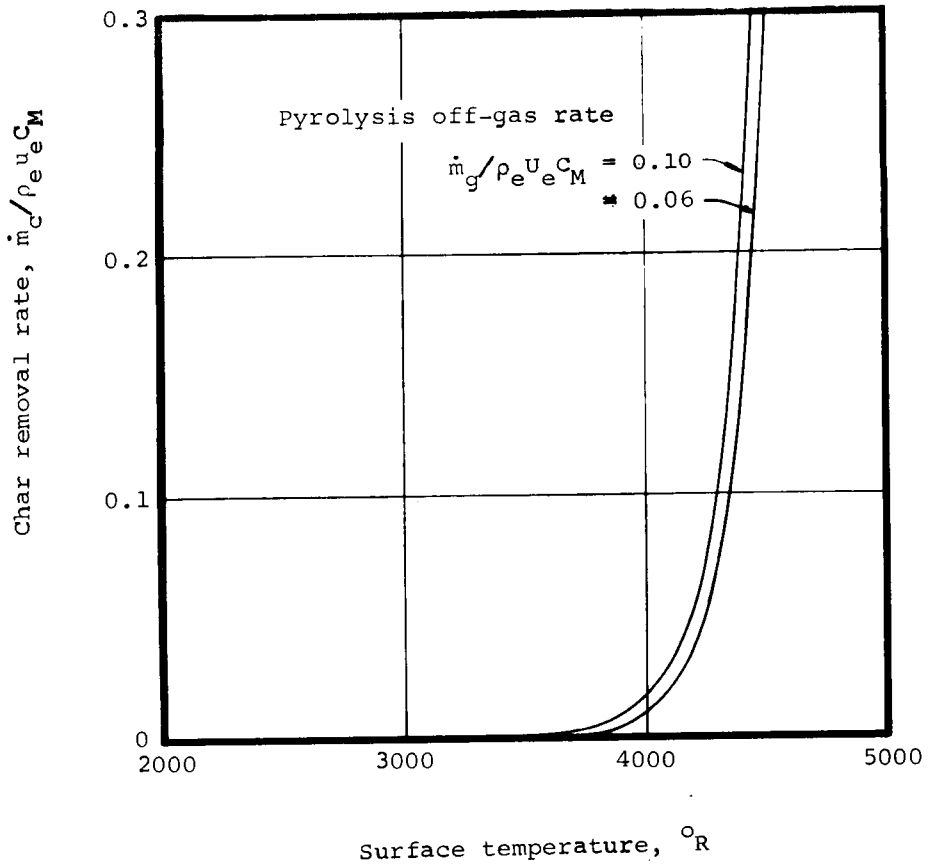

Figure 17.- Typical surface erosion response for silica phenolic. (A/A^* = 3.8, 260-SL-1 nozzle)

Char thermal conductivity assumed for the predictions was too high

Liquid layer runoff occurred

Solid phase/solid phase chemical reactions also contributed to the surface erosion.

These possibilities are discussed below.

The predictions considered surface chemical reactions (condensed phase/gas phase reactions), including material decomposition products, as the only surface erosion mechanism. For silica phenolic this erosion is highly dependent on surface temperature as shown in Figure 17. A lower char conductivity than that assumed in the predictions would result in a higher surface temperature and, for the conditions of the firings in question, a major increase in the predicted erosion would result. The assumed char conductivity for the predictions was nothing more than an educated guess so that a lower actual conductivity is certainly a possibility (char conductivity for silica phenolic was not measured under this contract).

Liquid layer runoff occurs when the viscosity of silica due to high surface temperature becomes low enough to make the surface susceptible to the gas phase shear at the wall. This phenomenon has, of course, been observed in many instances, e.g., Reference 6, but quantitative results on it are not yet available. When there is a net loss of material due to this mechanism, that is, when the quantity of "melt" leaving the location in question exceeds that arriving, this mechanism must be considered in the prediction of surface erosion depth.

Solid phase/solid phase chemical reactions between the silica reinforcement and the carbon residue of resin pyrolysis can also occur. These reactions may be expressed in the form of a "net" reaction of the form

$$SiO_2^* + C^* \rightarrow SiO + CO$$

where the asterisk denotes condensed phase and the reaction products are both in the gas phase. The net effect of the reaction is, of course, consumption of the char. This reaction has been observed and quantified in References 14 and 15 but has not yet been included as a surface erosion mechanism in the prediction technique.[5]

The prediction for the silica phenolic exit cone of the UA-1205-10 nozzle agrees favorably with the measured erosion (Figure 13) and, of course, assumed no liquid layer runoff or solid phase/solid phase reaction. This agreement may

[5] Its inclusion is under study in a current Aerotherm contract, NASA Contract No. NAS3-7945.

be fortuitous, however, because of the char conductivity used in the prediction calculations. The final assumed char conductivity was fairly low but was also felt to be consistent with the high silica content (80 percent) for that material. Because of this uncertainty in char thermal conductivity, the favorable agreement does not necessarily mean that the two mechanisms not considered in the predictions are unimportant. The definition of their importance and of accurate char thermal conductivity information must await further testing and analysis.

Note that for the 120-SS-1 nozzle the predicted erosion depths in the subsonic and throat regions agree favorably with the maximum measured erosion depths and that there are very large differences between the maximum and minimum depths (Figure 10). The general performance of carbon phenolic is discussed further in Section 3. These large differences are probably due to flow field effects associated with the propellant grain port shape and/or particle impaction effects. The latter effect would not be expected at the throat and downstream where the particles tend to channel towards the nozzle centerline due to inertial effects. Based on the comparison of predicted and measured erosion, the maximum measured depths are more representative of the erosion that should have been expected.

For the 260-SL-1 and 120-SS-1 nozzles, the exposed material in the low subsonic region was an elastomeric, a class of material that exhibits gross erosion. The quantity of gaseous products of ablation introduced into the boundary layer is therefore quite large; this results in a thickening of the boundary layer both locally and downstream, and this in turn results in a reduction of the heat transfer and mass transfer coefficients, and therefore in lower surface erosion downstream of the elastomeric material. This effect was not considered in the predictions. This is discussed further in Sections 3.5.3 and 4.1 wherein the results of an experimental and an analytic study of this phenomenon are presented.

2.4.2.2 Char depth and insulation performance

The predicted and, wherever possible, measured char depth performance for each location in each of the three nozzles is included in Tables III-V and, for the throats, in Figures 8, 11, and 14. In the tables, both char depth and char thickness are presented, char depth being the total depth of charred material including that removed by surface erosion, and char thickness being the depth of char below the final surface. The predicted char depth corresponds to the following defining criterion:

> The location in depth corresponding to a density halfway between the virgin material and fully charred material densities (e.g., see Figure 12)

From past experience this has been found to correspond quite closely to criteria used in the measurement of char depth for the materials of interest herein. For the Aerojet nozzles, the char depth was determined by penetrometer measurement and corresponded to the location where the resistance to penetration was significantly reduced over that in the char. No char depth measurements were available for the UA-1205-10 nozzle. Note in Figures 8, 11 and 14 that two other criteria for in-depth performance are also included:

> The location in depth corresponding to a density slightly less than the virgin material density (virgin material density less 2 percent of the difference between the virgin and fully charred material densities), labelled "pyrolysis zone".
>
> The maximum location in depth of the 500°F isotherm, where 500°F is felt to be a reasonable upper limit on back wall temperature for adequate thermal protection.

As noted from Table III, the agreement between the measured and predicted char thicknesses for the 260-SL-1 nozzle is very favorable at all locations considered. The predictions presented are, of course, the final ones in which the proper char conductivity data were used. Note the significant non-agreement from Figure 8(b) for the initial prediction at the throat of the 260-SL-1 nozzle; this is due directly to the improper char conductivity used. For the 120-SS-1 nozzle (Table IV) the same favorable comparison between final predicted and measured char thickness is apparent at the three downstream locations. In the subsonic and throat regions, however, the predicted char thicknesses are considerably below the measured values. The measured thicknesses are what would be expected for a graphite phenolic, not the carbon phenolic actually used. Some effect associated with the large circumferential nonuniformities in surface erosion experienced in this nozzle may be a possible explanation.

For similar firing times and similar chamber pressures, the char thicknesses for the graphite phenolic parts of the UA-1205-10 nozzle are considerably greater than those for the carbon phenolic parts of the 260-SL-1 nozzle (Tables III and V and Figures 8 and 14 respectively). This is a direct result of the higher char conductivity for graphite phenolic as compared to that for carbon phenolic (see Table I).

The discussions above have been centered on the post-fire char performance, the char thickness after cooldown. Actually, much of the char growth occurs after motor shutdown, as is apparent from Figures 8, 11 and 14. For instance, in the throat of the 260-SL-1 nozzle, the char depth (and thickness) increase about 0.25 inch during heat soak; the predicted char thickness is 0.50 inch at shutdown and 0.75 inch after cooldown (Figure 8). Most ablative nozzle applications to date have employed a "one-shot" nozzle and therefore the significant char depth, in terms of design for thermal protection, is the depth at motor shutdown, not after heat soak. This heat soak effect after shutdown is

also apparent from Figures 9, 12 and 15; in each case the second time at which distributions are presented corresponds approximately to motor shutdown.

The char depth is of course a measure of the insulation performance of an ablative material. A better measure, however, in terms of design requirements for thermal protection, is the depth of, say, the 500°F isotherm, 500°F being a reasonable upper limit for the back wall of an ablative material which has as a backup material the nozzle support structure. The material thickness requirements, in terms of this criterion, were predicted for all locations and are presented in Table VI. For a "one-shot" nozzle this 500°F limit is only significant to the end of the firing; if this limit is exceeded during cooldown it is of no consequence since the nozzle has already completed its function. The predicted thickness requirements are therefore presented in terms of the end of the firing (shutdown) and also in terms of the maximum penetration of the 500°F isotherm during cooldown. It should be noted that the actual thicknesses do not include ablative backup materials which were also used at many of the stations considered. From the table, it is apparent that in all cases the ablative material thicknesses used exceeded those required for adequate thermal protection of the nozzle support structure, by a significant margin. (The ablative part must, of course, also have sufficient thickness to maintain its structural integrity.) This certainly suggests a rather effortless approach to cost and weight savings in flightweight nozzles. Note that the thickness requirements for graphite phenolic are much greater than those for carbon phenolic due to the higher char thermal conductivity of the graphite phenolic. Silica phenolic with its low char thermal conductivity, exhibits the lowest thickness requirements, provided, of course, it is used under conditions where the surface erosion is tolerable.

2.4.2.3 General comments

One difference of possible significance between the 260-SL-1 nozzle and its subscale counterpart, the 120-SS-1 nozzle, is that all parts, exclusive of the exit cone, were autoclave cured in the former nozzle whereas the comparable parts were hydroclave cured in the subscale. These parts correspond to area ratios at which predictions were made of -1.2, 1.0, and 1.9 for both motors; the material performance results were presented as Figures 7 and 10 and Tables III and IV. Based on these results, including the comparisons of prediction and measurement, the type of cure had little or no effect on the material performance. Also, in the nylon overwrap cured parts, $A/A_* = 2.5$ and 3.8 in the 260-SL-1 nozzle and $A/A_* = 2.7$ and 4.8 in the 120-SS-1 nozzle, the comparison of measured and predicted performance relative to the other area ratios considered is similar in each nozzle. Again, therefore, the type of cure does not appear to have any appreciable effect on the performance of a material, at least for the conditions to which the materials were exposed in these nozzles. For

the record, the nominal cure pressures for the hydroclave, autoclave, and nylon overwrap cured parts were 1000 psia, 325 psia, and a calculated 75 psia, respectively.

The comparisons of predicted and measured performance for other nozzles analyzed by Aerotherm personnel are substantially similar to the results presented herein. These nozzles include the Thiokol 156-2C-1 motor and subscales and the LPC 156-5 and -6 motors and subscales; the results for these nozzles are presented in References 1, 3, 4, and 5.

2.5 Conclusion

The Aerotherm ablation computer programs were used to predict the ablative material performance for the nozzles of three large booster motors, the Aerojet 260-SL-1, the Aerojet 120-SS-1, and the UTC UA-1205-10. These predictions and their comparison with measurement were used as a base to analyze the material performance and evaluate the programs for use in nozzle design. Based on this analysis and evaluation, presented above, the following conclusions and comments are offered:

1. The exposed ablative materials of carbon phenolic and graphite phenolic in the 260-SL-1, 120-SS-1, and UA-1205-10 nozzles performed, by and large, as expected and as was predicted in terms of both surface erosion depths and char depths.

2. The carbon phenolics used in the throat extensions and exit cones of the 260-SL-1 and 120-SS-1 nozzles apparently exhibited a layup angle warp in the char region that resulted in a low apparent erosion for this material.

3. The erosion of silica phenolic is dictated by one or more of three possible erosion mechanisms:

   Surface chemical reactions, including material decomposition

   Liquid layer runoff

   Solid phase chemical reactions

Further experimentation and analysis is required to define the relative importance of these mechanisms.

4. Carbon phenolic exhibits a significantly better insulation capability, based on material thickness requirements, than graphite phenolic. This is directly related to the lower char and virgin material thermal conductivity for carbon phenolic.

5. Significant cost and weight savings without sacrifice of ablative material thermal protection performance can be effected through the use of thinner ablative material parts. This, of course, assumes that the structural integrity can also be maintained.

6. For the conditions and materials considered herein, the type of cure, hydroclave, autoclave, and in the exit cone, nylon overwrap, apparently had little or no effect on the performance of the materials.

7. The Aerotherm ablation computer programs are effective and accurate tools in design support and analysis of ablative material performance for solid rocket nozzle applications.

8. If either or both of the last two erosion mechanisms presented in 3 above are found to be important for silica phenolic, they should be included in the computer program prediction technique.

3. EXPERIMENTAL STUDY OF MATERIAL PROPERTIES AND PERFORMANCE

3.1 Introduction

Carbon phenolic and graphite phenolic materials were tested under conditions that simulated the combustion products environment of a typical solid propellant. The objective of the tests was to obtain information on material properties to better characterize the materials and to provide information in support of computer program predictions. The experimental program was broken down into three specific phases:

1. Determination of char thermal conductivity as a function of temperature and layup angle for MX4926 carbon phenolic and MX4500 graphite phenolic
2. Determination of surface erosion and char depth performance of the above materials under the simulated rocket nozzle conditions
3. Study of the influence of upstream ablation on the erosion of downstream materials.

The test materials were in the form of supersonic nozzles that were the exit nozzles of an arc-plasma generator which generated the simulation environment.

The following sections discuss the test program and results. Section 3.2 presents the experimental apparatus and the instrumentation used in the program. The test conditions are presented in Section 3.3. Certain studies and calculations in support of the experimental program are discussed in Section 3.4. The materials properties and performance determined under the program are presented and discussed in Section 3.5. Finally a summary of the results and conclusions is presented in Section 3.6.

3.2 Experimental Apparatus and Instrumentation

The experimental apparatus is discussed in this section, this apparatus consisting of the arc-plasma generator used to simulate the solid propellant

combustion products environment, the ablative material test nozzles that were subjected to this environment, and the instrumentation used to measure the test conditions and the material response. The arc-plasma generator and support equipment are discussed first in Section 3.2.1. The test nozzle configurations and materials are discussed next in Section 3.2.2. Finally, the instrumentation and data reduction procedures are presented in Section 3.2.3.

3.2.1 Arc-plasma generator and facility

The tests were performed using the Aerotherm 400-kilowatt constrictor arc-plasma generator, shown in Figure 18. Energy is added to the primary test gas via the steady electric arc discharge, the arc striking from the tungsten cathode in the cathode well to the downstream end of the tapered cylindrical anode (Figure 18). The primary gas is introduced tagentially at the insulated interface of the two electrodes to provide stable, high voltage operation. The secondary gas is introduced in the plenum chamber downstream of arc heating to yield the desired final gas composition and to insure equilibration of the primary and secondary gases before they exhaust through the test nozzle. The actual gases used in this test program are presented in a following section, Section 3.3, Test Conditions.

The arc unit is water cooled with high pressure deionized water. The electric power for the tests performed under this program was supplied by a direct current diesel elecrric generator. This unit has a maximum rated output level of 500 kilowatts of dc power (660 brake horsepower) for continuous operation. The power output and open circuit voltage are continuously variable, the maximum open circuit voltage being 1000 volts. A step-wise variable ballast resistor in series with the arc provides the necessary arc electric stability.

Arc starting is accomplished by generating an RF discharge across the insulating ring between the two electrodes after open circuit voltage has been applied across the electrodes. This usually must be accomplished at lower than desired primary flow rates to insure a successful RF breakdown. Upon starting, this flow is immediately increased to the desired value and final input power adjustments are made. This is accomplished within 5 seconds of arc ignition.[6]

The constrictor arc in its present configuration is limited to plenum chamber pressures up to about 8 atmospheres for nitrogen and for mixtures of nitrogen and helium or hydrogen.[6] This limitation is a limit of the thoriated tungsten cathode; above this pressure severe cathode degradation in the form of material loss at the surface occurs. As discussed in Reference 6,

[6] Note that these were limitations at the time of the test program; improvements in performance capabilities are continually being made.

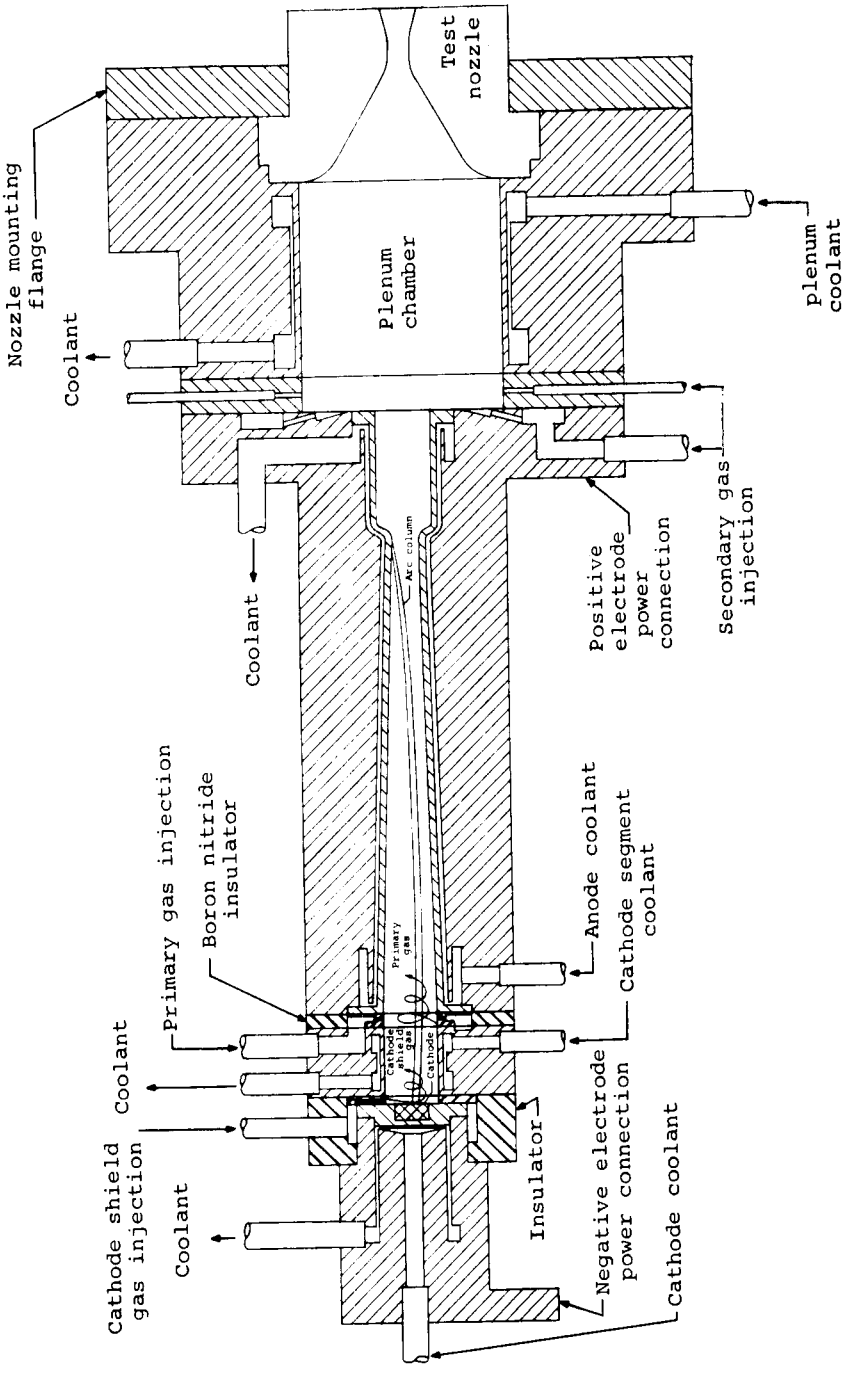

Figure 18.- Schematic representation of the Aerotherm constrictor arc-plasma generator in rocket motor simulation configuration.

testing at this moderate pressure actually simulates high pressures for large solid booster nozzles.

3.2.2 Test nozzles

The test nozzle configurations are presented in Figure 19. Three basic configurations are shown which correspond to the three phases of the test program. In the thermal conductivity test series, a long tubular throat, 0.812 inch long, (Figure 19(a)) was used to provide a sizable region of reasonably uniform conditions in which to make the precise temperature measurements required for accurate determination of conductivity. In this manner, lateral conduction effects were minimized. In the study of erosion and char depth performance, a more conventional nozzle contour (Figure 19(a)) was used to eliminate any possible tubular throat effects on the measured erosion. Figure 19(b) illustrates the test configuration for study of upstream ablation effects on downstream erosion. In this configuration, the subsonic portion of the nozzle was pure graphite to eliminate the pyrolysis gases generated upstream of the throat. This configuration represents the low upstream ablation case. The similar configuration of Figure 19(a) corresponds to the high upstream ablation case, being all composite ablative material. The test nozzles and corresponding test phase are also described as part of Table VII. In all nozzles, the throat diameter was 0.3 inch.

In the 0° throat layup nozzle for the thermal conductivity test series a parallel-to-centerline wrap was adopted throughout the nozzle for purposes of simplicity in fabrication. This approach embodied the hazards of laminate blowout but, because of the length of the throat, this was not felt to be a likely possibility and therefore the simple design approach was taken. The approach proved successful as anticipated.

The external nozzle geometry was dictated by attachment requirements to the arc-plasma generator. A typical installation is shown in Figure 18.

The thermocouple locations in the test nozzles for the determination of char conducitivity (Phase 1) and for the study of erosion and char depth performance (Phase 2) are presented in Figure 20. These locations were common to all 6 nozzles in these two test series (Figure 19(a)) and were defined by prior charring ablation calculations for the actual test conditions. Calculations were performed for the low and high conductivity extremes, 0° layup MX4926 carbon phenolic and 90° layup MX4500 graphite phenolic, respectively, and were based on estimated char conductivity values.

The billets from which the test nozzles were machined were fabricated by the Fiberite Corporation. The 90°-to-centerline billets were fabricated by compression die molding of prepreg fabric layers with each layer or ply staggered 45° from the adjacent one. The 0°-to-centerline billets were fabricated by tape wrapping, the prepreg tape width being the billet length. The complete

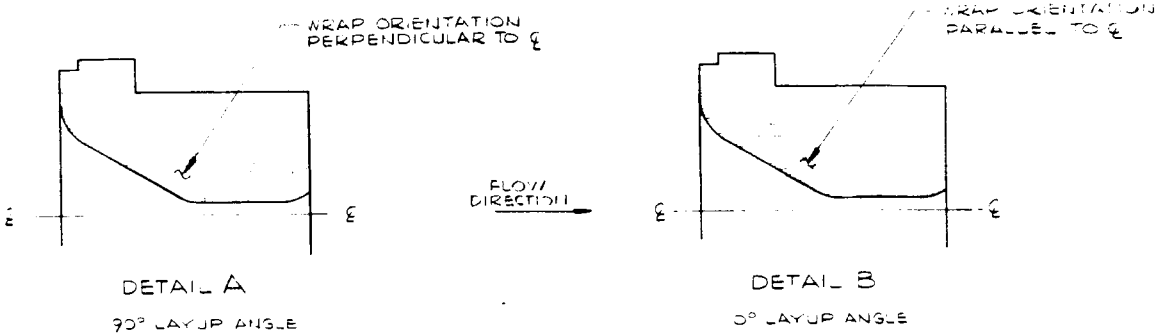

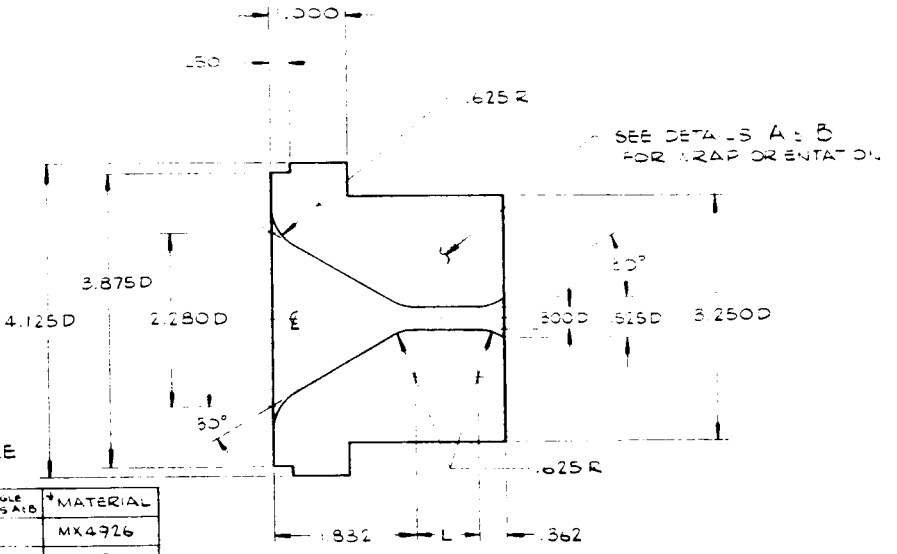

VERSION TABLE

PART NO.	DIM. L	LAYUP ANGLE SEE DETAILS A & B	*MATERIAL
600-01	.271	90°	MX4926
600-02	.271	90°	MX4500
600-03	.812	90°	MX4926
600-04	.812	90°	MX4500
600-05	.812	0°	MX4926
600-06	.812	0°	MX4500

*MX4926 - carbon phenolic
MX4500 - graphite phenolic

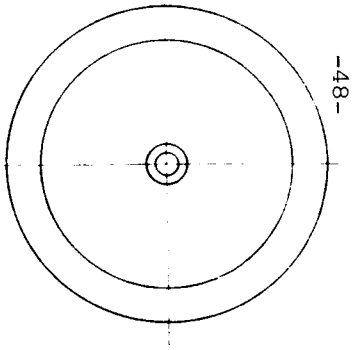

a) Standard

Figure 19.- Test nozzle configurations.

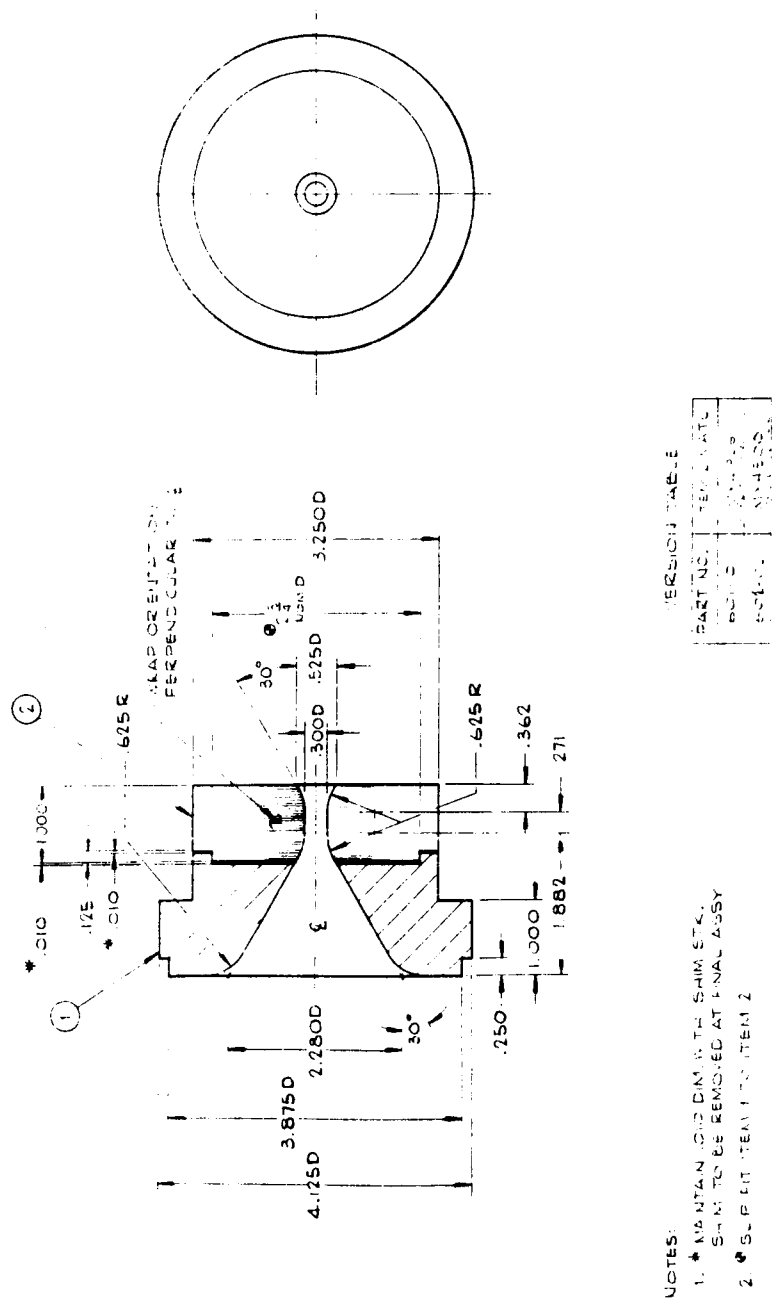

b) Segmented

Figure 19.- Concluded.

TABLE VII. SUMMARY OF ARC-PLASMA GENERATOR ROCKET SIMULATOR TESTS

Nozzle No.[a]	Material[b]	Layup[b] Angle	Test Phase	Simul. Gas	First Firing				Second Firing				
					Firing Time	Chamb. Temp.	Initial Chamb. Press.	Surface Erosion Depth	Firing Time	Chamb. Temp.	Initial Chamb.	Surface Erosion Depth	Char Depth
					sec	^{o}K	psia	in.	sec	^{o}K	psia	in.	in.
600-03	MX4926 carbon phenolic	90^{o}	Char Conductivity	Mix 5	60.4	3800	114.0	-.005	60.3	3600	107	.004	.54
600-05	MX4926 carbon phenolic	0^{o}	Char Conductivity	Mix 5	20.7[c]	3800	57.5[c]	-.004	60.2	3750	105	.003	-[c]
600-04	MX4500 graphite phenolic	90^{o}	Char Conductivity	Mix 5	60.4	3900	116.0	-.007	60.4	3750	109	.004	.49
600-06	MX4500 graphite phenolic	0^{o}	Char Conductivity	Mix 5	60.2	3800	111.0	-.004	60.2	3850	105	.003	.51
600-01	MX4926 carbon phenolic	90^{o}	Material Performance	Mix 4	47.8	3550	115.0	.044	52.4	3650	62.5	.053	.65
600-02	MX4500 graphite phenolic	90^{o}	Material Performance	Mix 4	47.3	3400	112.0	.041	47.2	3700	67.0	.046	.70
601-01	MX4926 carbon phenolic	90^{o}	Upstream Ablation Effect	Mix 4	40.2	3700	113.0	.037	50.1	3750	66.5	.073	-
601-02	MX4500 graphite phenolic	90^{o}	Upstream Ablation Effect	Mix 4	46.5	3650	113.0	.037	60.2	3850	66.0	.094	-

a) See Figure 19 for nozzle geometry

b) The two 601 series nozzles had a throat section of the indicated material and layup angle and a subsonic region of Graphitite G-90 graphite; all other nozzles were the indicated material throughout.

c) The first firing was performed with one of the two chamber pressure lines inadvertently left off; a third firing was therefore also performed at the following conditions and with the following results:

Firing Time - 60.3 sec
Chamber Temperature - 3700 ^{o}K
Initial Chamber Pressure - 101 psia
Surface Erosion Depth - 0.001 in.
Char Depth - 0.50 in.

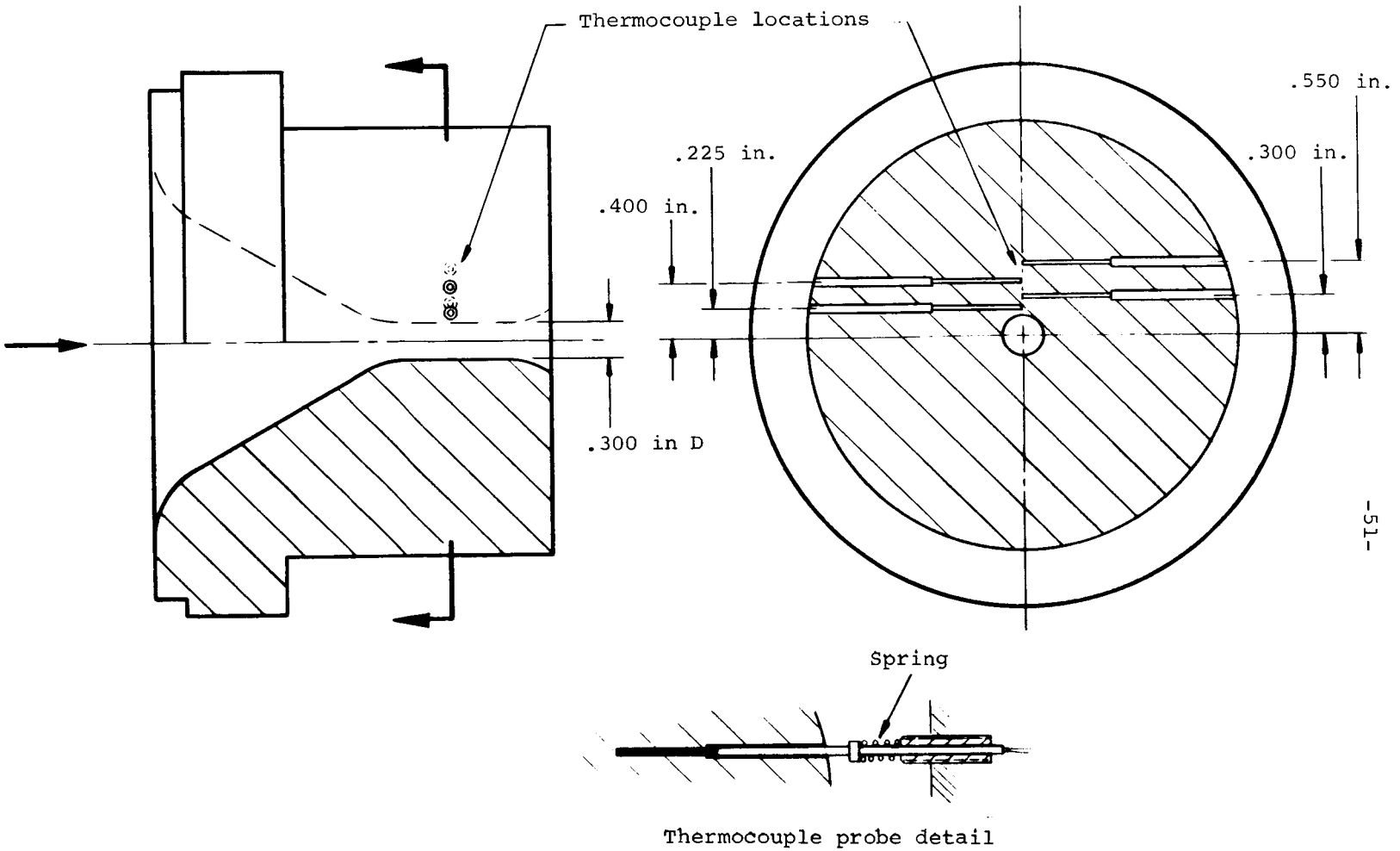

Figure 20.- Test nozzle thermocouple locations and instrumentation scheme.

billet was formed from three separate billets which were concentric hollow cylinders bonded together with Shell Epon 931. This was required because of the problems of shrinkage and delamination during cure if the wrapped sections are too thick.

The data for the prepreg tape used in billet fabrication is presented below.

Material	Billet Layup Angle	Resin Fraction	Volatiles Fraction
MX4926 carbon phenolic	90°	0.315	0.044
	0°	0.335	0.045
MX4500 graphite phenolic	90°	0.321	0.036
	0°	0.321	0.036

The molding and cure conditions for the 90° layup billets were as follows:

3°F per minute rise to 300°F

500 psia to 220°F

1000 psia from 220°F to 300°F

4 hours at 300°F and 1000 psia

The wrap and cure conditions for the 0° layup billets were as follows:

220°F tape temperature

4 to 6 rpm wrap speed

200 lbs per inch of tape width wrap tension

2000 psia (calculated) nylon overwrap pressure

2 hours at 300°F (oven cure)

Each nozzle was fired twice and in one case three times. There was no between-firing nozzle preparation performed; the nozzles were left untouched except for necessary post-test measurement to determine surface erosion depth.

3.2.3 Instrumentation and data reduction

The instrumentation and data reduction procedures used in the test program are discussed in the following sections. Section 3.2.3.1 presents this information as it pertains to defining the test conditions and Section 3.2.3.2 as it pertains to defining the material response.

3.2.3.1 Test conditions

The test conditions are defined by the gas total enthalpy, the chamber pressure, and, from these two, the chamber temperature. The enthalpy was determined from an energy balance on the arc-plasma generator. The power input to the arc unit was measured every 1.1 seconds through measurements of arc

current, with a precision shunt, and arc voltage, with a calibrated voltage divider. These outputs were fed to an analog-to-frequency converter with paper tape digital readout. The energy loss to the cooling water was determined from the measurement of flow rate and temperature rise of the water passing through the cathode-anode-plenum chamber combination (see Figure 18). The water flow rate was measured by calibrated rotameter that was read visually during test and the temperature rise was measured by a ΔT differential thermopile unit, the output of which was also recorded on the analog-to-frequency converter. The total gas flow rate was measured by visual readings of the differential pressures across calibrated orifices, one for the primary gas and one for the secondary gas. The gas total enthalpy was then calculated from the following energy balance equation

$$h_o - h_{ref} = \frac{EI - \dot{m}_{coolant}\left[c_p(\Delta T) - \frac{\Delta p}{\rho}\right]}{\dot{m}_{gas}} \qquad (10)$$

where h_{ref} is the "room temperature" enthalpy of the test gases. In all tests, the calculated enthalpy was checked by comparison of the measured chamber pressure and the chamber pressure determined by a sonic flow calculation for the determined enthalpy and the measured gas flow rate. The comparisons of theoretical and measured chamber pressures were favorable in all cases.

The chamber pressure was measured by a calibrated strain gauge total pressure tranducer, the output of which was recorded continuously on a 36-channel oscillograph. The pressure tap was located at the downstream end of the plenum chamber. The chamber temperature was determined from the calculated enthalpy and measured chamber pressure through equilibrium Mollier charts that were developed for the test gas mixtures (Reference 6). The time base for each firing was determined from the oscillograph record which accurately defined on-time and off-time and included a correlation signal between the digital output and the oscillograph output.

3.2.3.2 Material response

The ablative material response at the throat of the test nozzle was measured, directly or indirectly, in terms of surface temperature history, surface erosion history, and, for six of the eight nozzles, internal temperature histories at four locations in depth. Also, post-test measurements of surface erosion depths were made after each firing and post test measurements of char depths were made on the sectioned nozzles after the final firing. The surface temperature was measured continuously with an Infrared Industries "Thermodot"

recording optical pyrometer. The pyrometer senses brightness temperature in the near infrared at a wavelength of about 800 millimicrons. The pyrometer was sighted up the exit cone to a point in the tubular throat region approximately 0.150 inch upstream of the start of the exit cone. The view field was a spot approximately 0.085 inch in diameter. The brightness temperature recorded corresponded to a surface emissivity of 1.0; the recorded data were corrected to an emissivity of 0.85 (see Section 2.3.2.2) for reporting herein. The pyrometer output was recorded continuously on the 36-channel oscillograph.[7]

Internal temperatures were measured utilizing an instrumentation technique developed to yield accurate temperature data in low conductivity material such as those considered herein (Reference 6). This technique, utilizing Aerotherm spring-loaded thermocouple microprobes, is illustrated in Figure 20. The thermocouple probes were inserted into the test nozzles so that they were tangent to an isotherm at the thermocouple junction and the thermocouple wires were of small diameter, 0.003 inch. This minimized thermal conduction away from the thermocouple junction, an effect which results in a lower-than-actual indicated temperature. Also, to insure intimate contact of the thermocouple junction and the material, the probes were spring-loaded against the bottom of the probe holes. Finally, to minimize the disturbance to the heat flow caused by the probe, the probe was kept as small as practical. The ceramic insulator that enclosed the thermocouple wires was 0.035 inch in diameter. The nominal thermocouple locations for all instrumented nozzles are also indicated in Figure 20; the exact locations were determined from an X-ray photograph of the nozzle. The maximum error in these locations was determined to be ± 2 percent of the measured depth below the surface. The technique used for accurately defining the locations from the X-ray photographs was as presented in Reference 6 and is not repeated here. At the two nearest-to-the-surface locations (Figure 20), tungsten 5% rhenium-tungsten 26% rhenium thermocouples were used; they are accurate at temperatures up to about 4200°F (4660°R). At the other two locations, Chromel-Alumel thermocouples were used; they are accurate at temperatures up to about 2500°F (2960°R). The thermocouple outputs were recorded continuously through each firing and, except for one firing, for 2 to 5 minutes into the cooldown period. For the second firing on each nozzle, the thermocouples were simply left in place undisturbed.

A support study of possible thermocouple contamination, and the possible resultant inaccuracies in the measured temperatures due to exposure to a high temperature graphite and decomposing resin environment, was performed prior to the nozzle firings performed under the program. No contamination effects were found. The detailed results of this study are presented in a separate section, Section 3.4, Support Tests and Calculations.

[7] The high temperature exhaust gases were found to be transparent to the pyrometer and therefore caused no inaccuracies in the measured results (e.g., Reference 16).

the second firing. In the Mixture 5 tests for thermal conductivity determination, the nominal firing times were 60 seconds. The actual test conditions are included as part of Table VII.

3.4 Support Tests and Calculations

Tests to investigate possible thermocouple contamination problems and to measure the heat transfer coefficient in the test nozzle throat were performed prior to the start of the main test program. Also, computer calculations of the heat transfer coefficient and predictions of the material performance for the actual test conditions were performed. The results of these support tests and calculations are presented in this section. Section 3.4.1 discusses the thermocouple contamination study. The measured and calculated heat transfer coefficients for the test nozzle throat conditions are discussed in Section 3.4.2. Finally, the prediction of the material performance for the actual test conditions is discussed in Section 3.4.3.

3.4.1 Thermocouple contamination study

The existence of a thermocouple contamination problem due to exposure to high temperature carbon, graphite, and decomposing resin environments has been rumored but, to the authors' knowledge has never been substantiated or disproved. The result of this contamination would be a shift in the thermocouple calibration; if this occurs, the thermocouple output can no longer be accurately related to temperature. Since accurate temperature measurements are required to properly determine char thermal conductivity, a test effort to investigate possible thermocouple contamination was performed.

The test approach was simply the heating of a graphite phenolic test sample in which two thermocouple probes were inserted for test. The probes were calibrated before test and after test, the comparison of the calibration results being the measure of thermocouple contamination effects. The heat source was simply an acetylene torch. The test apparatus is shown in Figure 21. The test jig (Figure 21(a)) held an instrumented cylindrical graphite phenolic sample that was heated on its face. Using the acetylene torch, the maximum thermocouple temperature achievable was about 2500°F (2960°R).

In an effort to check the possibility of contamination at even higher temperatures, two of the thermocouples used in the actual test nozzles were calibrated before their installation in the nozzles. Unfortunately, both thermocouple beads were broken in the attempt to extract them from the test nozzle after the second firing.

To accomplish the calibration of the thermocouples for test, a calibration furnace was built and put in operation. A photograph of the unit is shown in Figure 21(b). The complete assembly was in a vacuum bell-jar which, in the photograph, has been removed. The heating element was a coil of tungsten wire wrapped around an alumina tube into which the calibration standard, on the right,

Surface recession through the firing was calculated from the measured decay of chamber pressure, this calculation of course applying to the throat only. The instantaneous throat area was calculated from the sonic flow relation and the measured test conditions, including the instantaneous chamber pressure. The instantaneous surface recession at the throat was then calculated from the determined throat area and the measured area at the start of the firing. This technique is presented in greater detail in Reference 6. Post-test measurement of surface erosion depth was also made at the throat through ball gauge and micrometer measurement.

After the final firing on each nozzle, it was sectioned for measurement of char depth. The char depth criterion was taken as the distance to the center of the narrow dark region that is indicative of the pyrolysis zone. This criterion has been used successfully by Aerotherm in the past and is consistent with the criterion presented and used in Section 2.

3.3 Test Conditions

The test gases used in the test series were Mixtures 4 and 5 formulated in the program of Reference 6. Both of these mixtures approximate the reactive specific heat of typical solid propellant combustion products; their elemental compositions are:

Element	Mass Fraction	
	Mixture 4	Mixture 5
Helium (He)	0.2284	0.2237
Nitrogen (N)	.6191	.7764
Oxygen (O)	.1525	-

Mixture 5 is effectively inert to graphitic and carbonaceous materials for the test conditions of interest and no chemical erosion of the test nozzles occurs in tests utilizing this gas. It was used in the thermal conductivity test series so that the surface recession could be accurately defined, i.e., effectively zero. Mixture 4 is chemically reactive and duplicates the actual oxidation potential of a typical solid propellant. It therefore simulates both the thermal and chemical aspects of solid propellant combustion products. This gas was used in the tests on material erosion performance and upstream ablation effects.

The nominal test conditions were an initial chamber pressure of approximately 100 psia and a chamber temperature of approximately 3800°R for Mixture 5 and 3500°R for Mixture 4. These conditions yielded approximately the same static temperature in the throat and approximately the same total enthalpy for both mixtures. The firings were performed at a constant gas flow rate and, therefore, the chamber pressure decreased with firing time for Mixture 4 as surface erosion occurred. The firing times in this case were the times for the chamber pressure to decay to about 65 psia in the first firing and 40 psia in

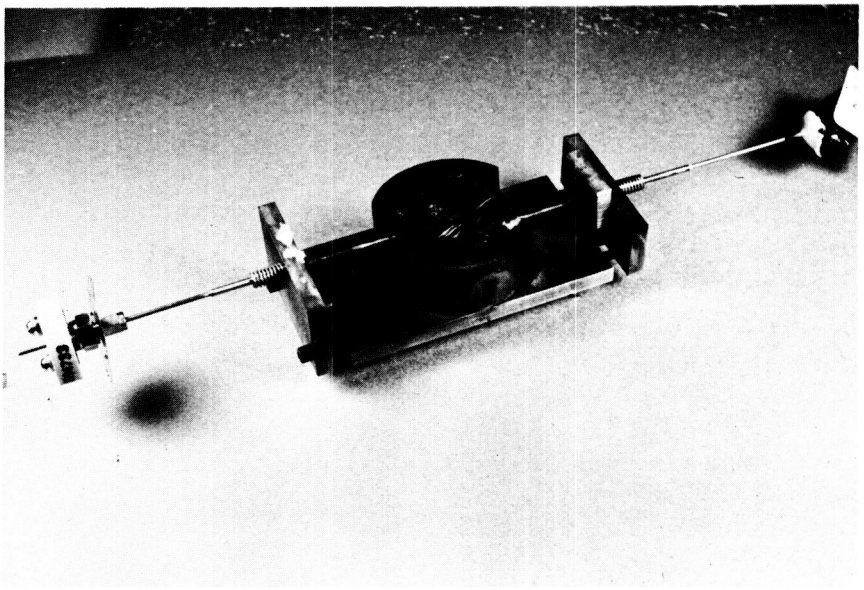

a) Test apparatus

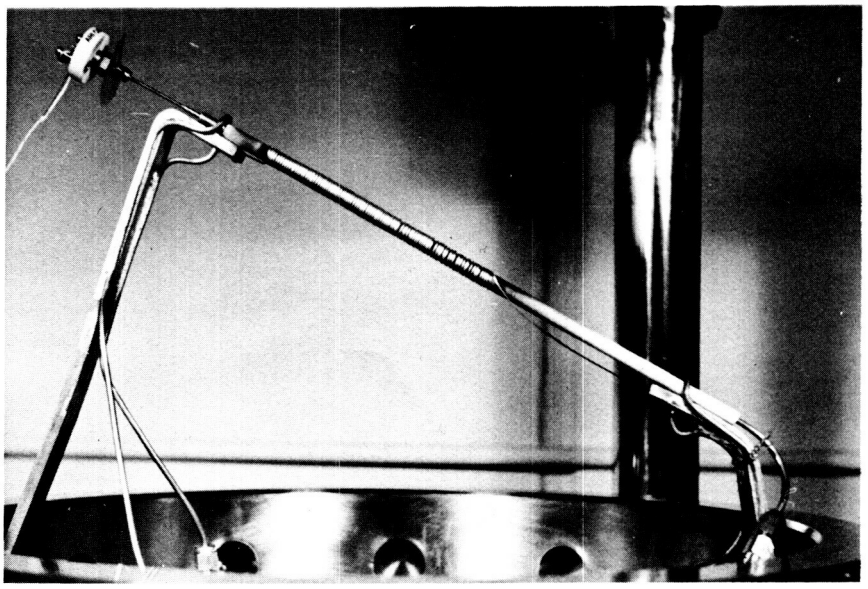

b) Calibration furnace

Figure 21.- Thermocouple contamination study apparatus.

and the thermocouple to be calibrated, on the left, were inserted. The two thermocouples were inserted to the mid-portion of the heated section until they were within 1/16-inch of each other. Temperature control was accomplished by control of the voltage across the tungsten heating element.

Typical calibration results are presented in Table VIII for the two thermocouple types considered, tungsten-5% rhenium-tungsten 26% rhenium, and Chromel-Alumel. The calibrations before and after exposure to the high temperature carbon phenolic environment are presented and compared and the exposure conditions of time and indicated maximum temperature are also included. Based on these results, no contamination effects are apparent up to the moderate temperatures of these tests and for the relatively short exposure times. Also, no significant contamination effects are anticipated up to at least 4000°F, the maximum thermocouple temperature achieved in the char thermal conductivity tests.

3.4.2 Heat transfer coefficients

In order to define the test conditions in terms of heat transfer coefficient, the coefficient at the nozzle throat for the test nozzle configuration was measured using a water-cooled calorimeter nozzle and calculated using the boundary layer computer program (Section 2.3.2.3). The calculations of heat transfer coefficient are discussed first, followed by a discussion of the calorimeter tests.

The heat transfer coefficients for the throat of the test nozzle configurations (Figure 19(a)) were calculated using the boundary layer computer program discussed in Section 2.3.2.3. The discussion of this program and the input requirements are not repeated here. The viscosity used in the calculations was calculated for both test gas mixtures from References 17 and 18. The Prandtl number used was 0.72 for both mixtures and was estimated from Reference 19 from a consideration of the mixture constituents (this value was also used in Reference 6). The calculated coefficients at the center plane of the throat were essentially identical for the two test gases at the nominal test conditions and for the two respective nozzle throat geometries (Figure 19(a)).[8] These coefficients for three discrete wall temperatures and a 0.3-inch and 0.4-inch throat nozzle are:

---

[8]The calculated coefficients decreased slightly with increasing distance down the tubular throat, and for a given distance from the throat entrance the Mixture 5 coefficients were slightly higher than the Mixture 4 coefficients for the nominal test conditions.

TABLE VIII

TYPICAL THERMOCOUPLE CONTAMINATION TEST RESULTS

Tungsten 5 percent rhenium - tungsten 26 percent rhenium Thermocouple 5			
Indicated Temperature, °F			
Standard Thermocouple	Test Thermocouple		Apparent Error
	Pre-fire	Post-fire	
1312		1327	15
1313		1327	14
1313		1327	14
1425	1428		3
1426	1431		5
1428	1432		4
1687		1704	17
1687		1704	17
1687		1704	17
1754	1764		10
1753	1763		10
1754	1764		10
1959		1980	21
1959		1979	20
1960		1980	20
2022	2034		12
2026	2038		12
2025	2037		12
2258	2274		16
2260	2274		14
2256	2272		16
Exposure - Installed in graphite phenolic material, heating for 80 seconds, maximum indicated temperature of 2350°F for test thermocouple			
Chromel-Alumel Thermocouple 2			
1268	1252		-16
1396		1370	-26
1396		1370	-26
1640	1604		-36
1727		1692	-35
1727		1692	-35
1906	1858		-48
1910	1862		-48
1983		1940	-43
1983		1940	-43
2158	2093		-65
2163	2091		-72
2163	2092		-71
2231		2167	-64
2231		2167	-64
Exposure - Installed in graphite phenolic material, heating for 99 seconds, maximum indicated temperature of 870°F for test thermocouple			

Wall Temperature $^{\circ}R(^{\circ}F)$	Heat Transfer Coefficient lb/ft^2-sec	
	$D_* = 0.3$ inch	$D_* = 0.4$ inch
760 (300)	0.277	0.166
3800 (3340)	0.214	0.128
4200 (3740)	0.203	0.122

These calculated coefficients agree very closely with the experimental results of Reference 6 when they are corrected for the difference in chamber pressure between the two cases.

The heat transfer calorimeter used for experimentally measuring heat transfer coefficient consisted of individually water-cooled segments that were stacked together to form the desired nozzle contour. The local-average heat flux was then determined for each segment from the measured coolant water flow rate and temperature rise. The details of the nozzles and test technique are presented in Reference 6. Two nozzle configurations were used, one with a 0.3-inch diameter throat and duplicating the test nozzle contour used in the thermal conductivity tests (see Figure 19(a)) and one with a similar geometry but with a 0.4-inch diameter throat, this larger diameter being the approximate diameter at the start of the second test for the nozzles in which surface erosion occurred. In both configurations, the throat section consisted of three segments and data were taken for these three segments only since this was the region of interest in the main test program. Unfortunately, the inlet segment of the 0.3-inch diameter nozzle failed before final tests were performed and no final results were obtained for this nozzle configuration. Also, the results for the 0.4-inch diameter nozzle were somewhat ambiguous. A quick check of the data immediately after the calorimeter nozzle tests yielded a throat heat transfer coefficient consistent with the calculated result presented above; the final reduced data, however, yielded a considerably lower coefficient. In the attempt to reconcile this anomaly, no definitive error in either result was found; however, it is felt that the thermocouple circuit sensitivity setting was incorrectly specified and used in the final data reduction. A check of the results that would have been achieved if the setting had been displaced one position from that assumed resulted in a measured heat transfer coefficient of 0.177 lb/ft^2-sec as compared to the comparable calculated value of 0.166 lb/ft^2-sec presented above.

Based on the ambiguity of the experimental results, the calculated values of heattransfer coefficient presented above were used in all calculations of material response discussed in the following section.

3.4.3 Prediction of material performance

The ablation computer programs were used to predict the material performance for several of the tests performed herein as a check on the test results and, conversely, as a check on the accuracy of the computer programs. Predictions were made both for Mixture 4 and Mixture 5 tests. Again, the programs and input requirements are not repeated here; the predictions were performed as presented in Section 2.3. The predictions employed the char conductivity results obtained under the program and the resin fractions measured for the actual nozzle materials (Section 3.2.2). The unequal diffusion coefficient option was used in all calculations. The prediction results are presented in the following section which discusses the actual test program results.

It should be noted that the Charring Material Ablation program was used in the determination of char conductivity. It, however, was the primary tool in the data reduction and its use is, therefore, discussed with the test results.

3.5 Materials Properties and Performance, Results and Discussion

The test results under the three phases of the experimental studies task of the contract are presented in the following sections. These three phases encompassed the determination of char thermal conductivity for a carbon phenolic material and a graphite phenolic material, the determination of erosion and char depth performance for these same materials under simulated conditions, and a study of upstream ablation effects on downstream erosion. The results of these test programs are discussed in Sections 3.5.1, 3.5.2, and 3.5.3, respectively. The description of the test nozzles, the actual test conditions, and the test results in terms of surface erosion and char depth are presented in Table VII.

3.5.1 Char thermal conductivity

Char thermal conductivity was determined for:

MX 4926 carbon phenolic	0° layup
	90° layup
MX 4500 graphite phenolic	0° layup
	90° layup

from the test firings on nozzles 600-03 through 600-06 (Table VII). The results are presented in Figure 22 in terms of conductivity as a function of temperature. They were also presented previously as part of Table Ia. Before discussing these char conductivity results, a discussion of the technique for determining them is in order.

Thermal conductivity is usually determined under steady state conditions and, in the case of chars, with a laboratory prepared sample. The character

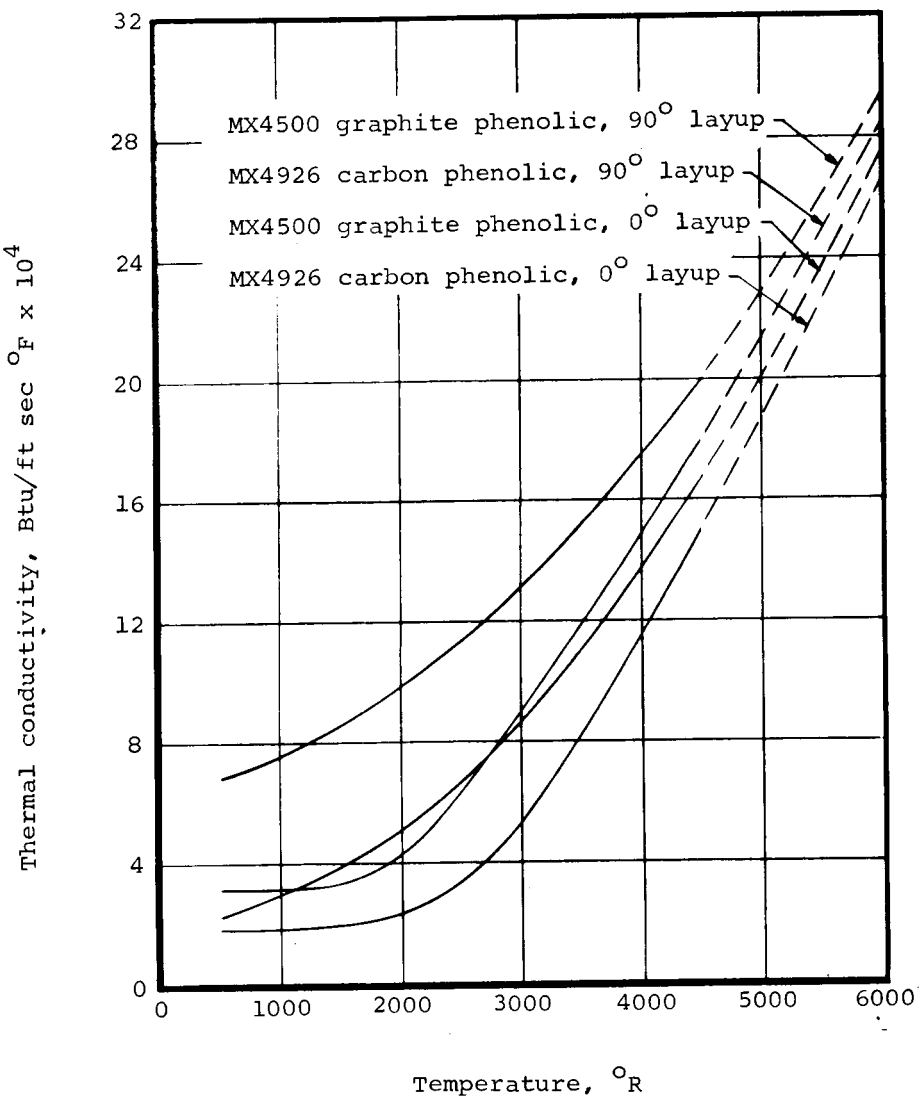

Figure 22.- Char thermal conductivities for carbon phenolic and graphite phenolic.

of a char is a function of the manner in which it was formed, however. A material sample which is charred under slow heating conditions in a laboratory is different in character than a char formed under the dynamic, rapid heating conditions of a nozzle firing since resin decomposition is a function of both temperature and time, Equation (4). It is therefore difficult to obtain a representative sample prior to a firing of the material of interest, and even after the firing, the size of the sample that can be obtained from a fired component is limited. Also, the steady state determination of conductivity excludes the possible effects of the pyrolysis gases that flow through the char; they can influence the effective material conductivity through their contribution to conduction and through their effect on radiation interchange in the porous char matrix.

In the technique used here these problems are circumvented; the data from which the char conductivity was determined were obtained under dynamic conditions that simulated those of a rocket nozzle. These test data were the temperature histories of the four thermocouples in depth (Figure 20), the measured surface temperature, and the measured surface erosion which, for Mixture 5, was negligible. The data reduction procedure was a parametric input of char thermal conductivity (as a function of temperature) to the Charring Material Ablation Program, with the surface temperature and surface erosion (zero) also input, until the predicted internal temperature histories agreed closely with those measured.[9] This determination was made from the data of the first firing on each nozzle only; the second (and in one case third) firing was used as a check on the determined conductivity. The predicted final internal temperature histories corresponding to the conductivity results of Figure 22 are presented in Figure 23 for each test nozzle together with the measured internal temperature histories.[10] The agreement between measured and predicted temperature histories is very favorable. The number of "guesses" on char conductivity required to achieve these results ranged from 6 to 18 for the four cases considered. It is felt that the number of iterations can be reduced in future determinations and that this procedure might well be amenable to automation.

The comparisons of predicted and measured internal temperatures for the second firing on each nozzle are presented in Figure 24. The agreement for the 90° layup nozzles is, again, very favorable,[10] but for the 0° layup nozzles, the predictions are consistently somewhat higher than the measured temperatures. Upon sectioning the test nozzles after testing was complete, the probable source of this discrepancy was revealed. The variation of char thickness with axial distance was such as to indicate that axial conduction in the mature char of

---

[9] This technique was first employed by Aerotherm personnel in late 1964 using data from the program of Reference 6.

[10] Thermocouple 1 of Figure 23(a) was determined to be only 0.029 inch below the surface rather than the nominal depth of 0.075 inch. Because of this very shallow depth, the temperature gradient along the thermocouple probe was severe and conduction effects not present at greater depths can be significant. The lower-than-predicted temperature is felt to be due to this effect.

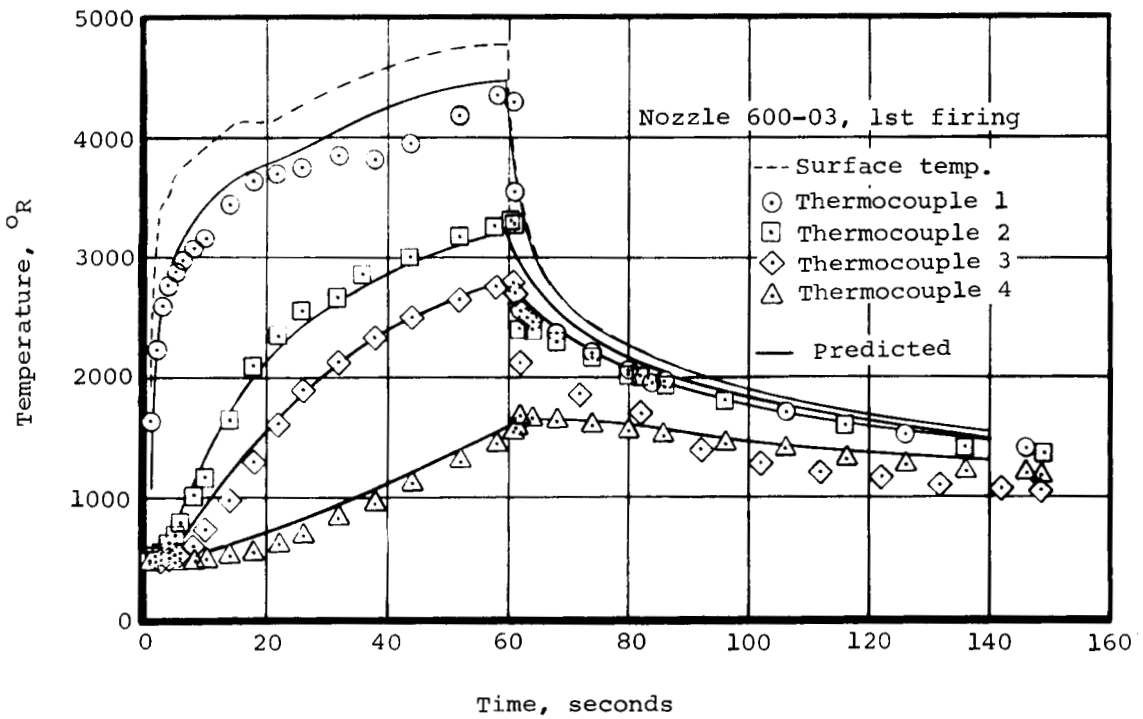

a) MX4926 carbon phenolic, 90° layup

Figure 23.- Comparison of predicted and measured internal temperature histories for the first firings on the thermal conductivity test nozzles.

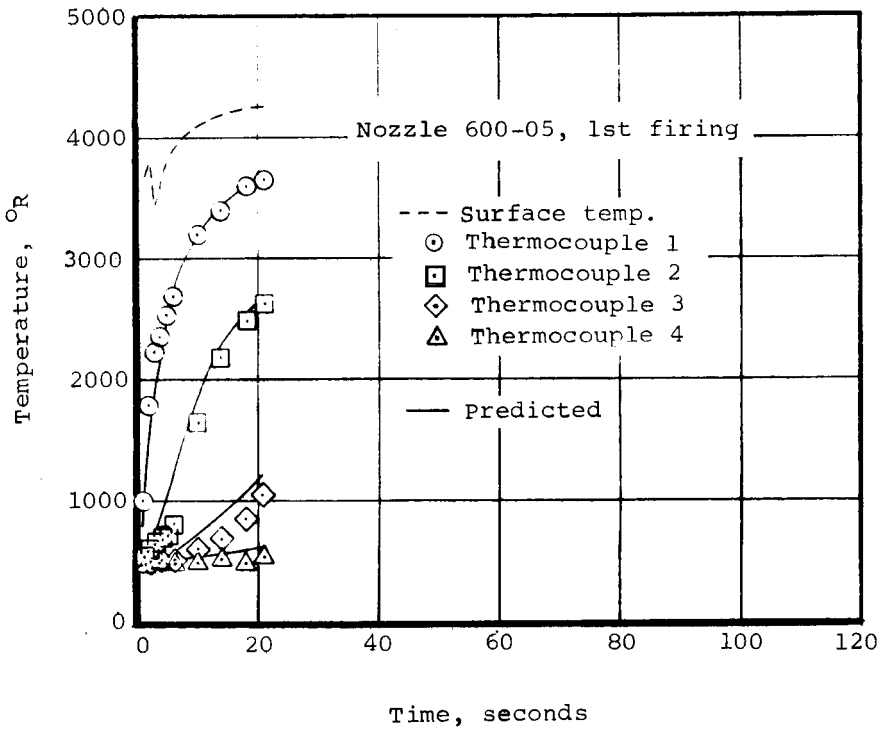

b) MX4926 carbon phenolic, 0° layup

Figure 23.- Continued.

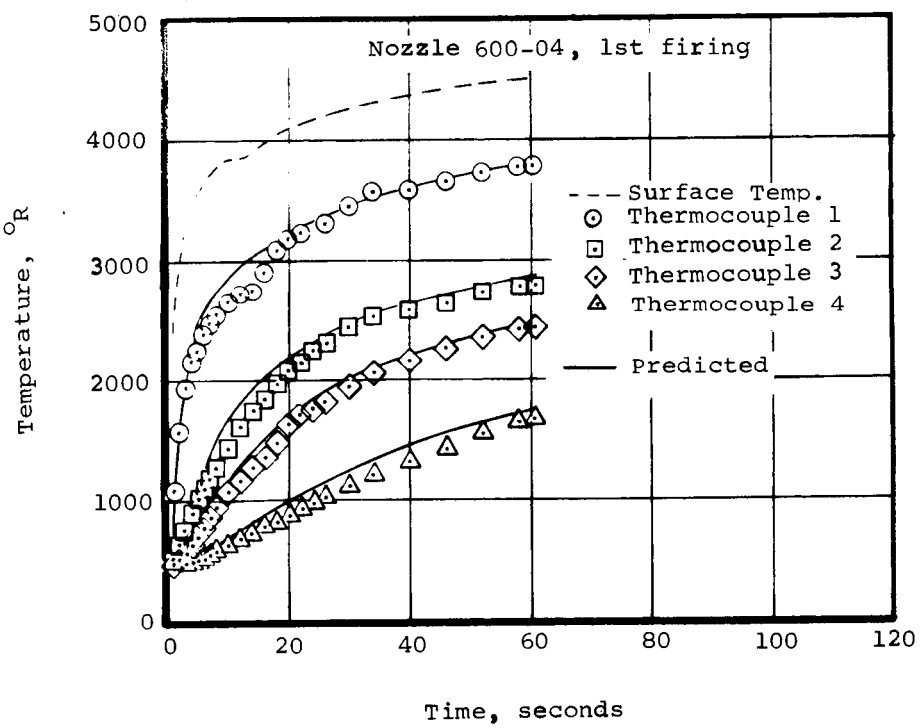

c) MX4500 graphite phenolic, 90° layup

Figure 23.- Continued

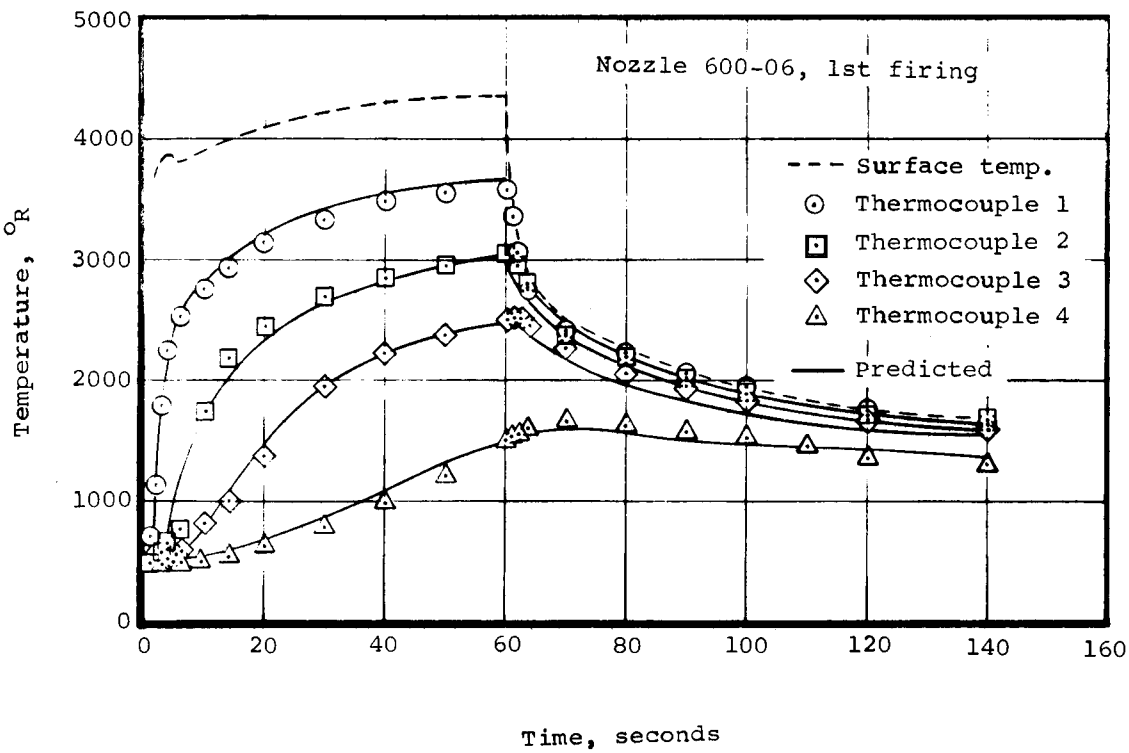

d) MX4500 graphite phenolic, 0° layup

Figure 23.- Concluded.

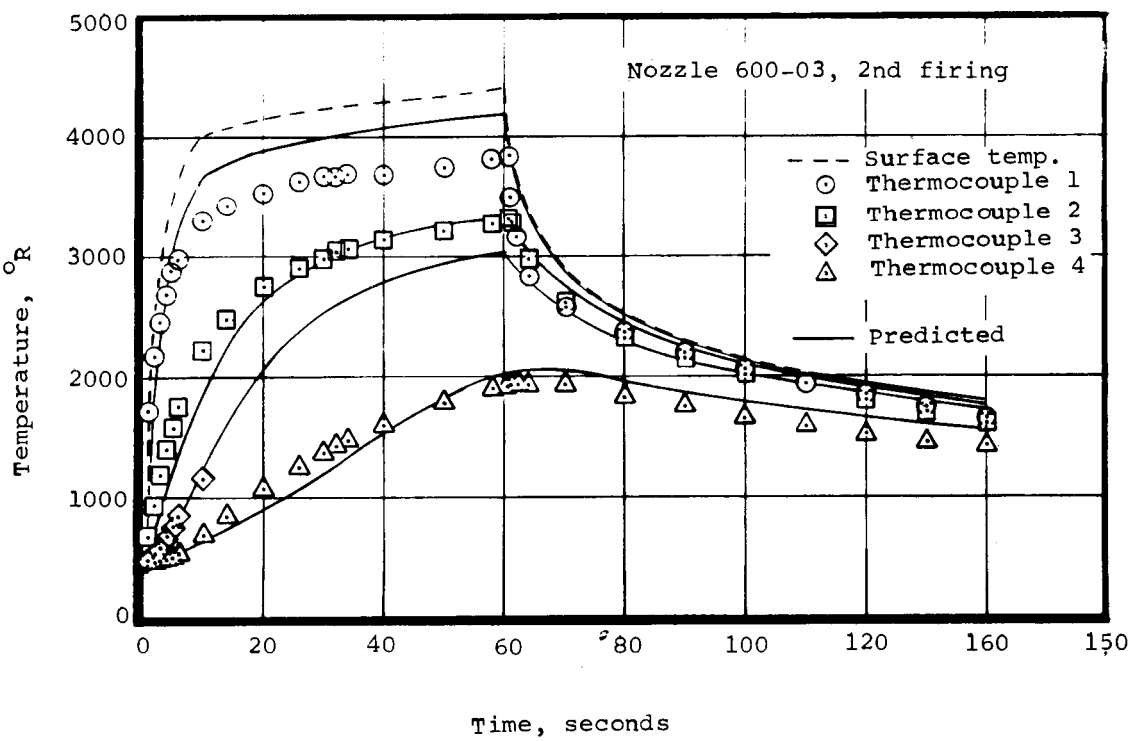

a) MX4926 carbon phenolic, 90° layup

Figure 24.- Comparison of predicted and measured internal temperature histories for the second firings on the thermal conductivity test nozzles.

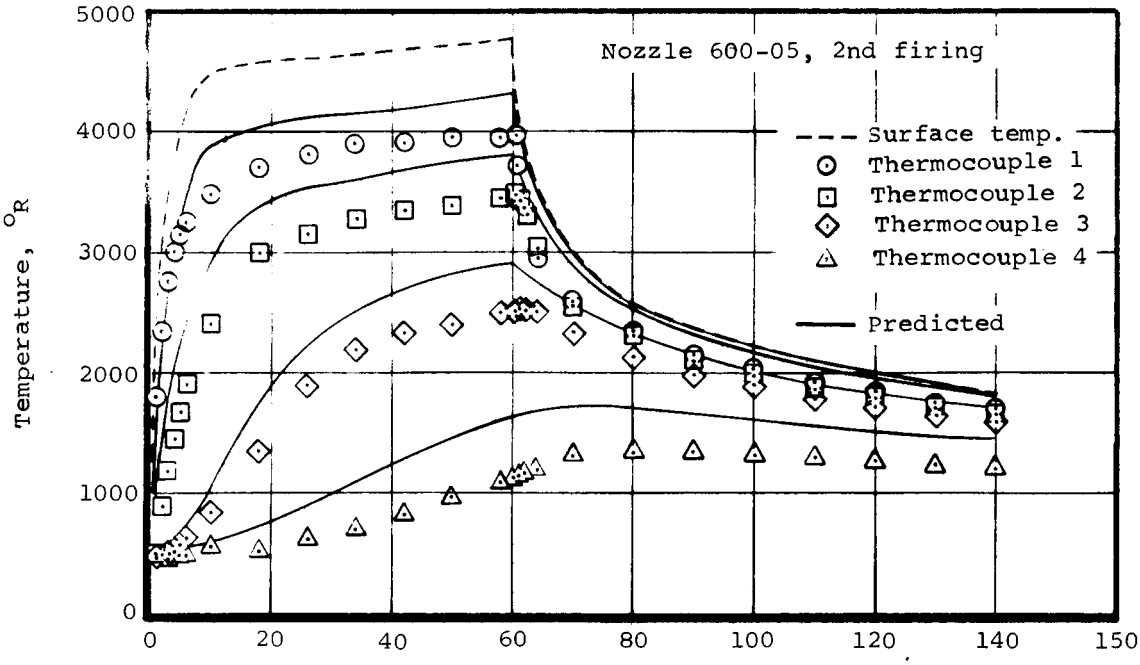

b) MX4926 carbon phenolic, 0° layup

Figure 24.- Continued.

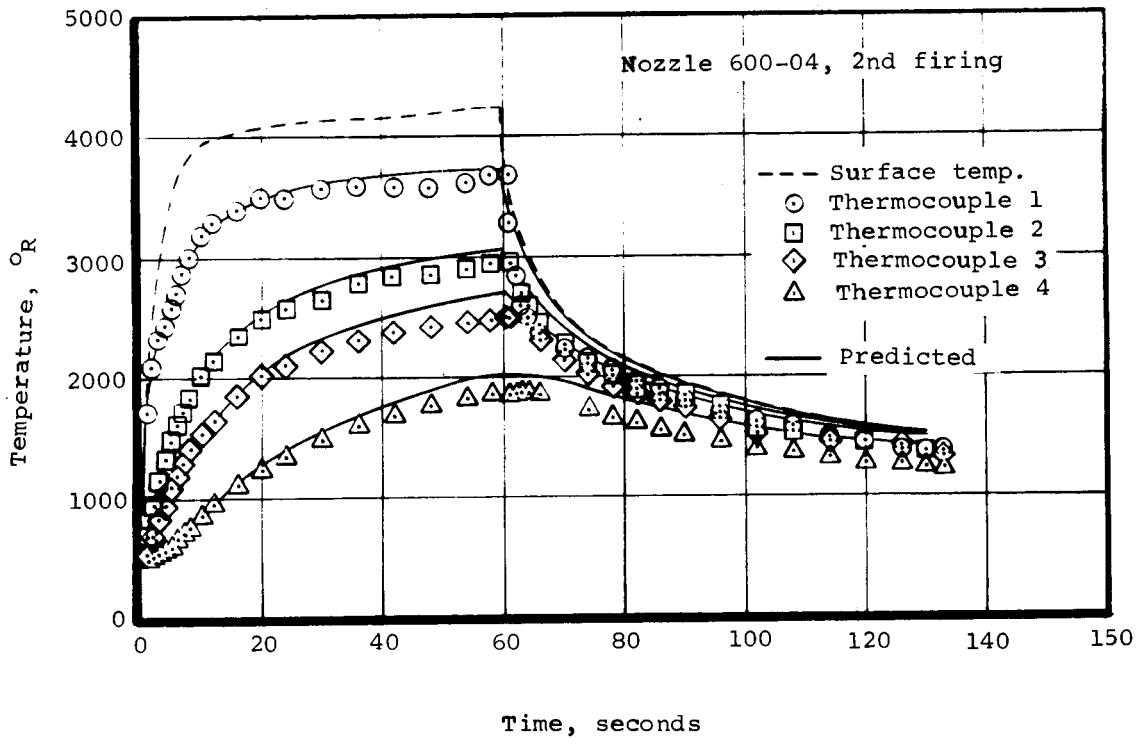

c) MX4500 graphite phenolic, 90° layup

Figure 24.- Continued.

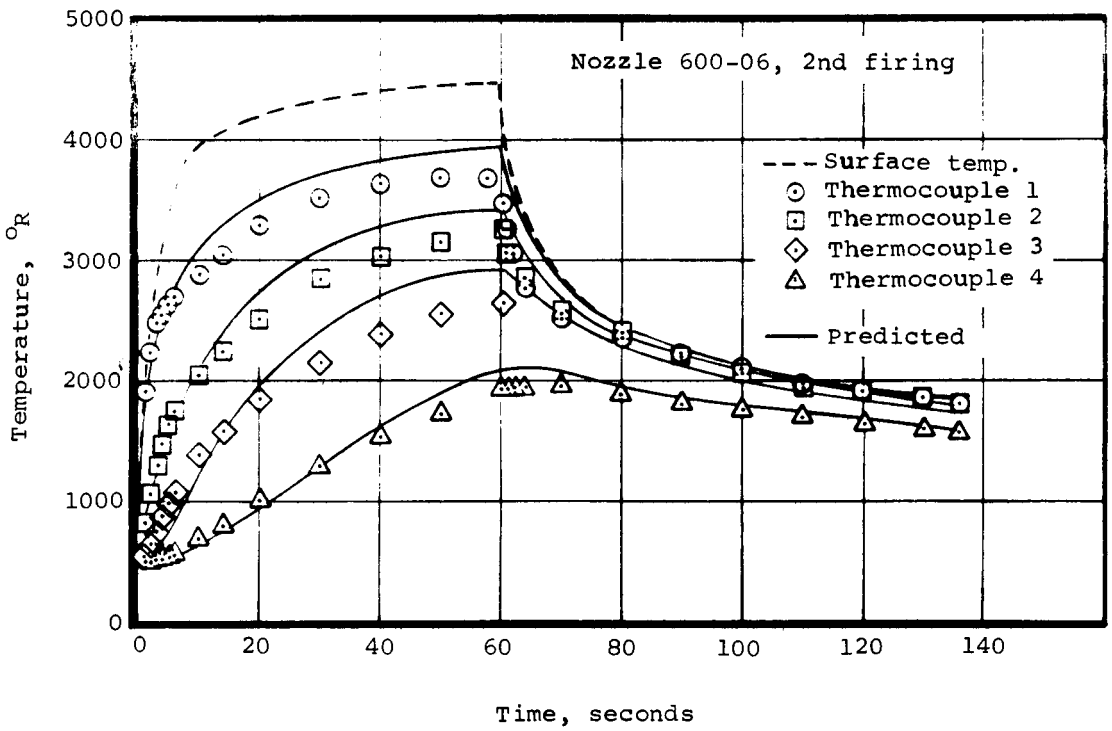

d) MX4500 graphite phenolic, 0° layup

Figure 24. - Concluded.

the second (and third) firings occurred. The measured temperatures would therefore be expected to be lower than predicted since the prediction assumed one-dimensional radial heat flow.

Based on the favorable (and explainable) agreement between the predicted and measured internal temperature histories (Figures 23 and 24), the char conductivity results of Figure 22 are felt to be quite adequate for engineering calculations of material performance. The results are valid to $4500^{\circ}R$ and have been extrapolated to $6000^{\circ}R$. These conductivity results are now discussed below.

The MX4500 graphite phenolic exhibits a higher char conductivity than the carbon phenolic; this is typical of these materials as a class and is not an observation limited to the two specific materials considered. The general character of the conductivity variation with temperature is different for the two materials, the temperature variation of conductivity being quite small for carbon phenolic at moderate temperatures. As expected, the 90° layup angle yields a higher conductivity than the 0°; this cloth orientation offers a better path for heat conduction than does the across-the-cloth orientation. At higher temperatures, this layup angle effect becomes quite small; internal radiation becomes an effective conduction mechanism at high temperature and it apparently is not so directionally dependent. Note from Table I that the room temperature char conductivity is close to the virgin material conductivity. In fact, for both materials at both layup angles in each, it was reasonable to equate "high" temperature virgin material conductivity and room temperature char conductivity.

The results presented are, of course, for the extremes in layup angle, 0° or heat flow perpendicular to the layup direction and 90° or heat flow parallel to the layup direction. Although no data were taken for intermediate layup angles, the following equation, repeated from Section 2.3.2.2, is suggested for generalizing the results presented

$$k = k_{0^{\circ}} \left[1 + \left(\frac{k_{90^{\circ}}}{k_{0^{\circ}}} - 1 \right) \sin \theta \right] \qquad (3)$$

where θ is the layup angle referenced to a tangent to the surface.

It is significant to note as an aside to the main test results that the 0° layup nozzles performed very well. These nozzles were fabricated parallel to the centerline throughout (Figure 19(a)). This resulted in what is usually considered to be an unfavorable layup angle "direction" in the subsonic portion of the nozzle and also in a susceptibility to laminate blow-out. These nozzles exhibited no unusual effects and no delaminations, however, and actually performed better than the 90° layup nozzles in this latter respect.

The performance of the MX4926, 90° layup nozzles (600-03) was predicted using the set of ablation computer programs and the measured test conditions;

the surface response, in terms of surface erosion and surface temperature, was calculated rather than specified as was done in the determination of char conductivity. The measured and predicted surface and internal temperature histories are presented in Figure 25. The predicted surface erosion depth was zero. The agreement between measurement and prediction is therefore very favorable on all counts. Based on these comparisons, the calculated heat transfer coefficients (Section 3.4.2) and the computer program treatment of surface thermochemistry appear to be quite accurate.

3.5.2 Material performance

The study of surface erosion, char depth, and overall performance was made for MX4926 carbon phenolic and MX4500 graphite phenolic, both at 90° layup angle only. The test conditions and results are summarized in Table VII (nozzles 600-01 and -02) and post-test photographs of the sectioned nozzles are presented in Figure 26. The test results are discussed below.

The average surface erosion rates based on post-test measurement and firing time are presented below:

Material	Average Surface Erosion Rate, mils/sec	
	1st Firing	2nd Firing
MX4926 carbon phenolic	0.92	1.06
MX4500 graphite phenolic	0.87	0.97

As expected, the erosion performance of the two materials is almost identical. The graphite phenolic does exhibit a slightly better performance however. Note that the restart (second) firings exhibited a higher erosion rate than the initial firings. This is due to the absence of the protective pyrolysis off-gases early in the restart firings before the heat penetrated the mature char formed in the previous firing. The comparison shown above is somewhat conservative in terms of this effect in that the severity of the heat flux and mass flux was lower in the second firing due to the erosion, and therefore, increase in throat diameter, of the first firing. (Note the differences in initial chamber pressures between the first and second firings as shown in Table VII.) Taking this into account, the average recession rate for comparable heat flux and mass flux conditions would be a factor of about 1.8 higher for the restart (second) firings. The implications for restartable motors are apparent.

The final char depth after the two firings, presented in Table VII, is greater for the graphite phenolic material as would be expected due to its higher thermal conductivity as compared to carbon phenolic. The difference in char depth for the two materials is quite small, however. This is due to the small diameter axisymmetric nozzle configuration used in these tests; if the nozzle diameter had been large or if the test sections had been flat slabs, the difference between the char depth performance for the two materials would have been significantly greater.

The post-test examination of the sectioned nozzles, Figure 26, revealed some interesting observations regarding the material performance. The carbon

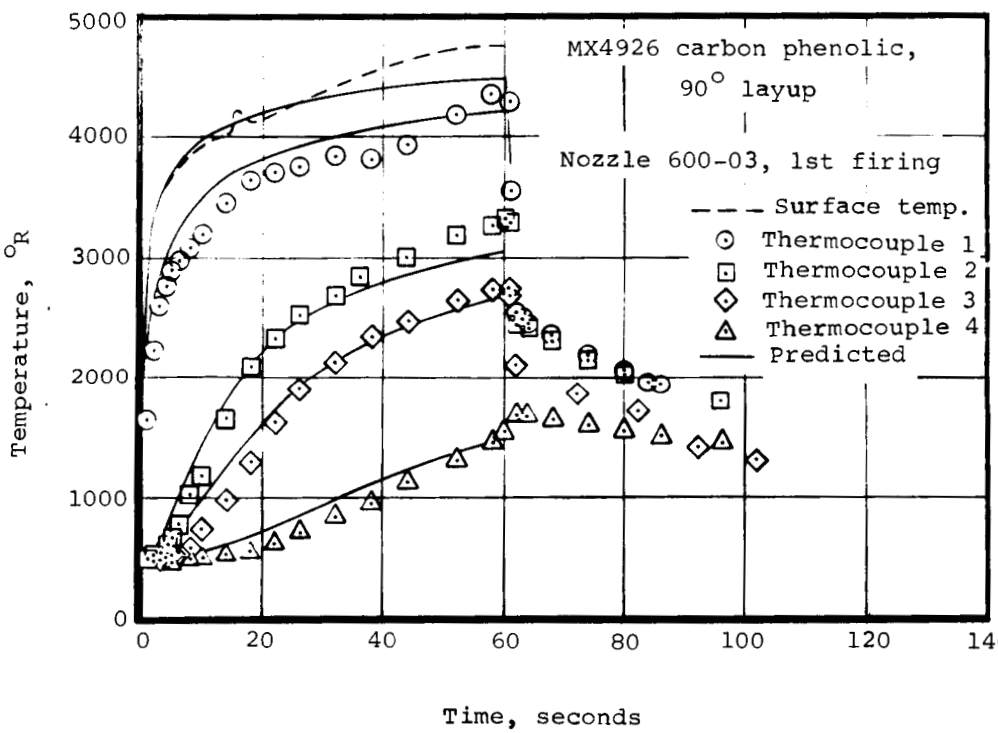

Figure 25.- Full prediction (Option 1) of surface and internal temperature histories and comparison with measurement for the first firing on the MX4926 carbon phenolic, 90° layup thermal conductivity test nozzle.

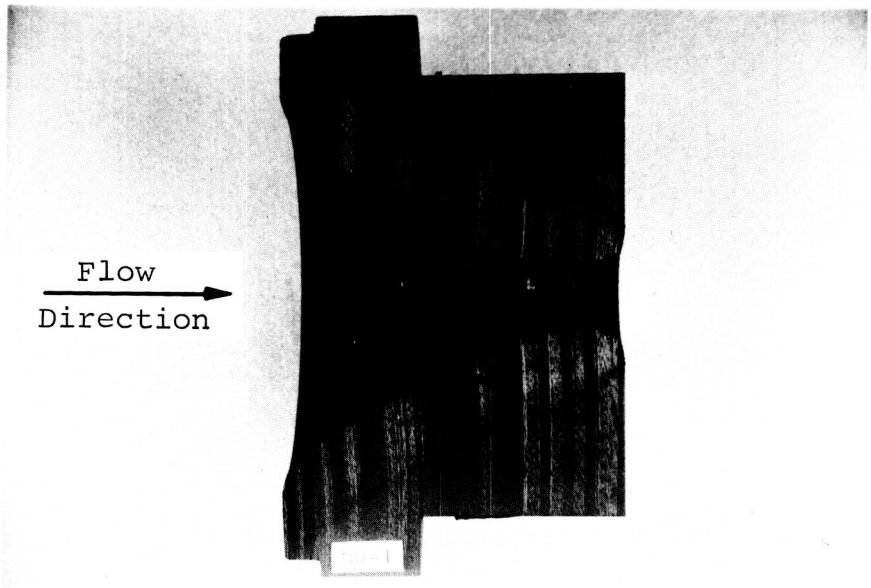

a) MX4926 carbon phenolic (600-01)

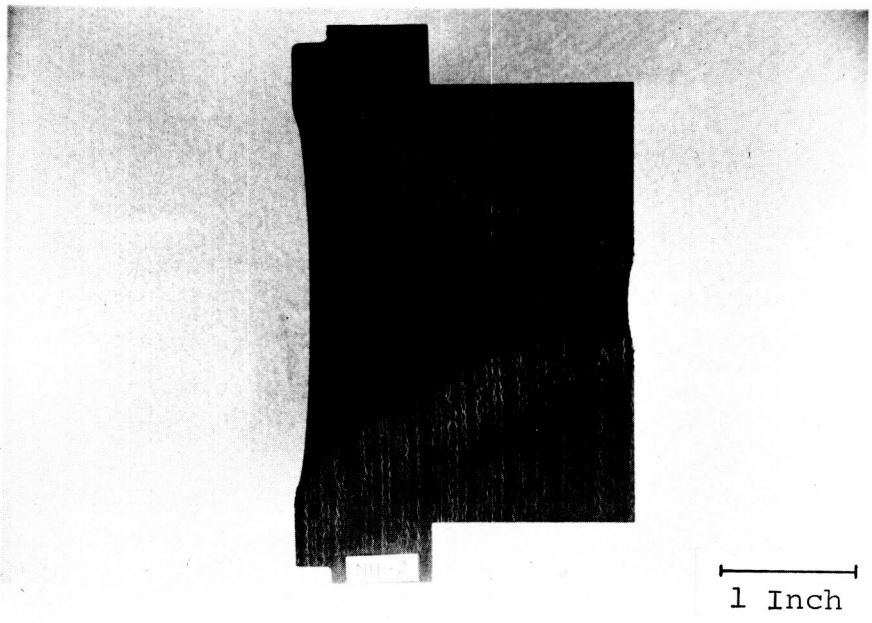

b) MX4500 graphite phenolic (600-02)

Figure 26.- Sectioned test nozzles.

phenolic exhibited significantly more delaminations and these delaminations were more extensive than for the graphite phenolic. It was not possible to determine whether they occurred during the firing or during cooldown. In any case, the carbon phenolic certainly appears to be the less stable material.[11] Also note that both nozzles exhibited a mechanical erosion in the exit cone due to a shock structure in the flow in this region; a normal shock occurred just upstream of the nozzle exit due to a mismatch of exit area ratio (too high) and exit pressure (atmospheric). The carbon phenolic was significantly more susceptible to this mechanical erosion phenomenon than was the graphite phenolic.[11] Finally, surface erosion overtook the thermocouple closest to the surface in the second firing on both nozzles. In both cases, the surface nonuniformity which resulted caused a significant local nonuniformity in erosion downstream.

In summary of the above results, graphite phenolic exhibited a slightly better surface erosion performance and appeared to be the more stable material. Carbon phenolic, however, exhibited a better insulation performance as indicated by the comparisons of char depth.

The nozzle firing results were subjected to further analysis through computer program predictions of the material performance for the actual conditions of the two firings on each of the two nozzles. These predictions and the measured results are presented in Figure 27 in terms of surface erosion and char depths. The agreement is very favorable. The predictions for the first firings bear out the conclusion that graphite phenolic exhibits better erosion performance. Since the predictions were made in a continuous firing-cooldown-firing-cooldown sequence, it is difficult to make surface erosion comparisons for the second firings; because of the differences in measured and predicted erosion, the conditions at the start of the second test firings were different than the conditions at the start of the second prediction firings. Note the difference in the character of the predicted erosion as a function of time for the first and second firings in the two cases. In the first firings, the erosion rate is approximately constant after the first few seconds of the firings, whereas in the second firings, the erosion rate starts very high and steadily decreases with time throughout the firings. As discussed above, this is due to the initial absence of pyrolysis gases followed by their slow increase through the firing as the heat penetrates the mature char from the previous firing and resin decomposition again occurs. The predicted and measured char depths are in very good agreement, Figure 27, and the predictions bear out the previous conclusion that the carbon phenolic has the better insulation performance. Note the relatively small increase in char depths through the restart (second) firing and cooldown.

---

[11] These observations may be related to the carbon cloth used in prepeg tape manufacture. More stable carbon cloths are purported to be available today.

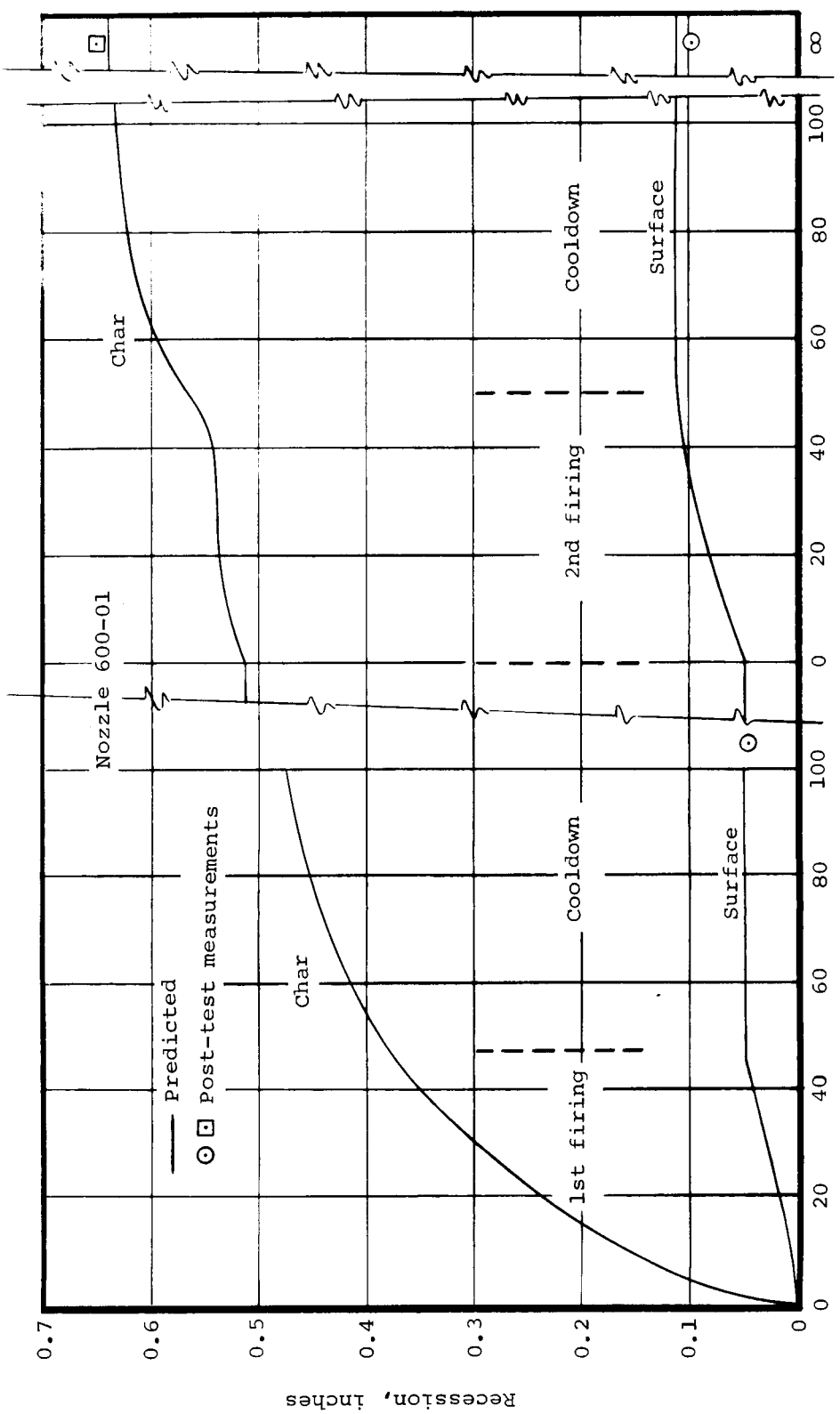

a) MX4926 carbon phenolic, 90^{o} layup

Figure 27.- Comparison of predicted and measured surface erosion and char depth performance.

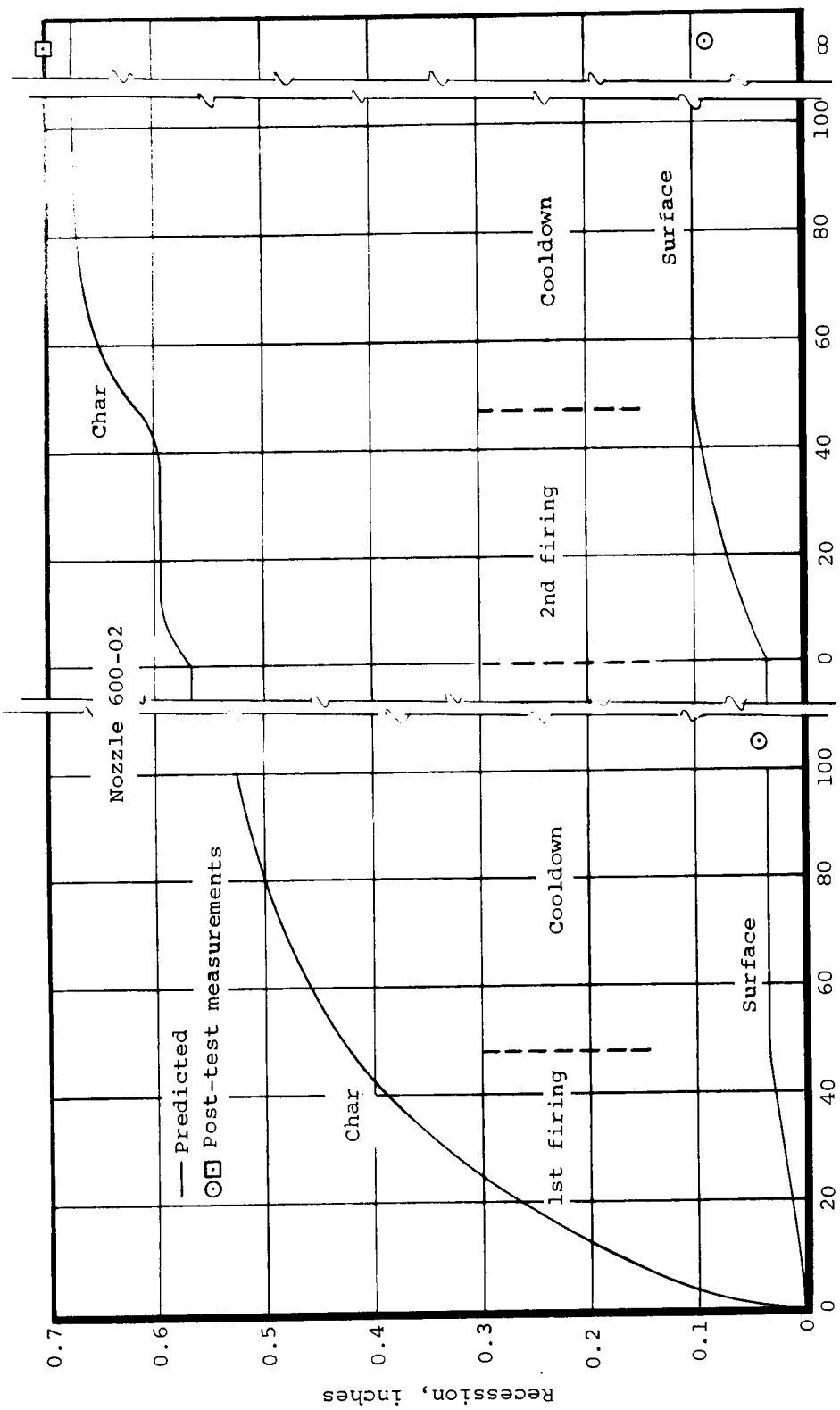

b) MX4500 graphite phenolic, 90° layup

Figure 27.- Concluded.

A typical comparison of measured and predicted surface and internal temperature response is presented in Figure 28; these results are for the first firing on the MX4926 nozzle (600-01). The comparison of these results is somewhat obscured by the differing location of the surface with respect to the thermocouples for the predicted and measured cases. For instance, the actual recession is expected to be considerably less than predicted for the first few seconds of firing due to the transient time required to achieve full test conditions (Section 3.2.1). The predicted surface temperature is considerably lower than that measured. The reason for this has not been defined but the measured result certainly appears to be real based on the comparison of predicted and measured internal temperatures late in the firing.

It should be noted that, although the results presented in this section are indicative of performance in an actual rocket nozzle, they are not quantitatively equivalent to the actual nozzle performance for location with the same material and the same heat and mass transfer coefficients. For composite ablatives that form a carbonaceous char (e.g., carbon and graphite phenolic) and for the simulation scheme used here, the close duplication of gas oxidation potential, specific heat, and transfer coefficients, does not result in a duplication of recession rate. This is primarily a result of the test nozzle geometry, the absence of surface chemical reactions involving hydrogen, and the different effects of the pyrolysis off-gases between the actual and simulation environments. First, the geometry effect is associated with the small diameter axisymmetric nozzle configuration used. Because the pyrolysis off-gases are generated in depth where the average diameter of the pyrolysis zone is significantly greater than the "surface" diameter (see sketch),

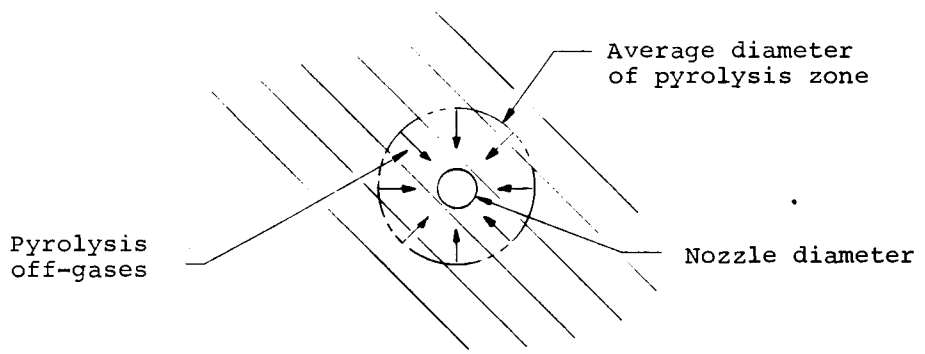

the pyrolysis off-gas rate per unit surface area is significantly greater in the test configuration used herein. In general, the greater this off-gas rate the lower the surface erosion rate since the "blowing" at the surface reduces

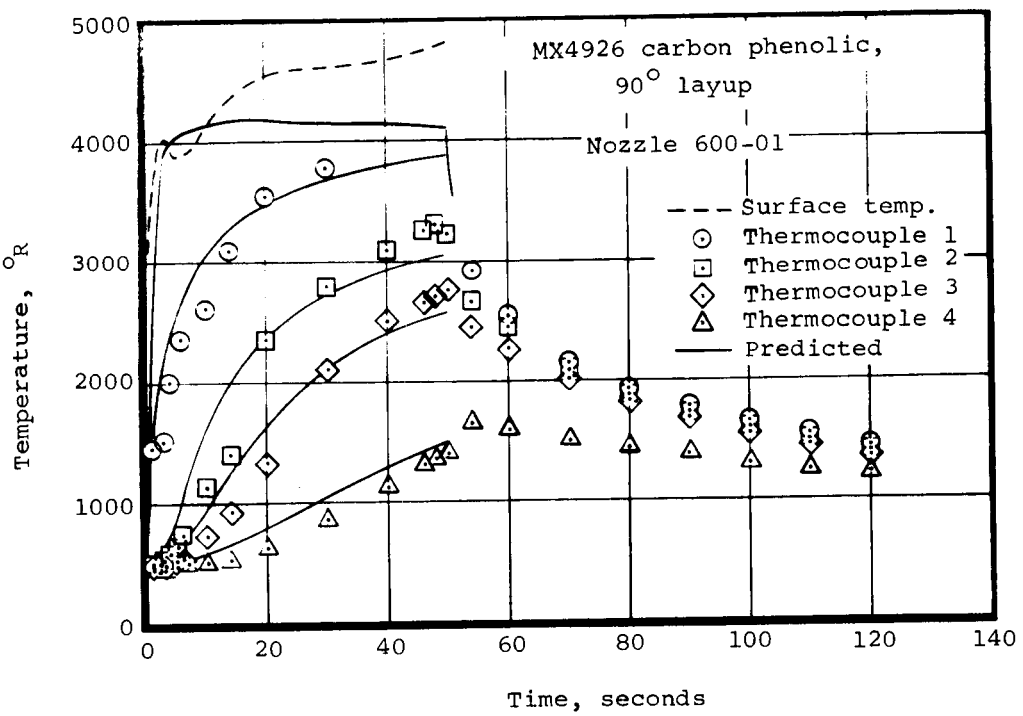

Figure 28.- Comparison of predicted and measured surface and internal temperature histories for MX4926 carbon phenolic, 90° layup (600-01).

the heat and mass transfer coefficients and the off-gases react with some of the oxidizing species which, with reduced off-gases, would react with the char. Second, the reactions of hydrogen with the char surface that occur in an actual propellant are, of course, not present in the simulation case since hydrogen is not included in the test gases (Section 3.3). These reactions can account for as much as 25 percent of the surface erosion in a typical solid rocket (e.g., Reference 3). Finally, the chemical interaction of the pyrolysis gases with the edge gases to inhibit the reaction with the char is somewhat different for the simulation gases than for the solid propellant combustion products.

3.5.3 Effect of upstream ablation

The study of the effect of upstream ablation on surface erosion downstream was unfortunately rather undefinitive. As discussed in Reference 1, large quantities of ablation products introduced upstream of, say, the throat of a nozzle result in a lower throat erosion than would occur in the absence of these ablation products. The extremes studied herein were an all-phenolic nozzle, nozzles 600-01 and -02 (Figure 19(a)), as the high upstream ablation case, as compared to a phenolic throat section with a pure graphite subsonic section upstream, nozzles 601-01 and -02 (Figure 19(b)), as the low upstream ablation case. The results are presented in Table VII and post-test photographs of the sectioned nozzles or throat sections are presented in Figures 26 and 29. The erosion would be expected to be higher for the 601 series nozzles because of the lower upstream ablation. The second firings on these nozzles support this conclusion; the first firings, however, do not. This anomalous result is related to the nozzle configuration used for the low upstream ablation case. The pure graphite of the subsonic section is a much better conductor of heat than the phenolic impregnated materials and, because of this, presented a very high temperature, relatively speaking, along the interface between the phenolic throat sections and the graphite subsonic section. The fiberfrax insulation between these two sections was not sufficient to prevent significant heat conduction to the phenolic sections and therefore charring occurred at this interface to a considerable depth. This effect apparently reversed the intended effect for the first firings; because of the high local blowing immediately upstream of the throat section due to the decomposition at the interface, the low upstream ablation nozzle actually became the high upstream ablation nozzle. Note that quantity and distance from the point of interest, not quantity alone, are the significant parameters in the investigated effect. (This is discussed further in Section 4.1.) In the second firing, very little further charring in the interface apparently occurred and the absence of the upstream resin decomposition products resulted in the expected increased erosion. Although the results cannot be regarded as definitive, it is interesting to make some comparisons between the second firings as presented below:

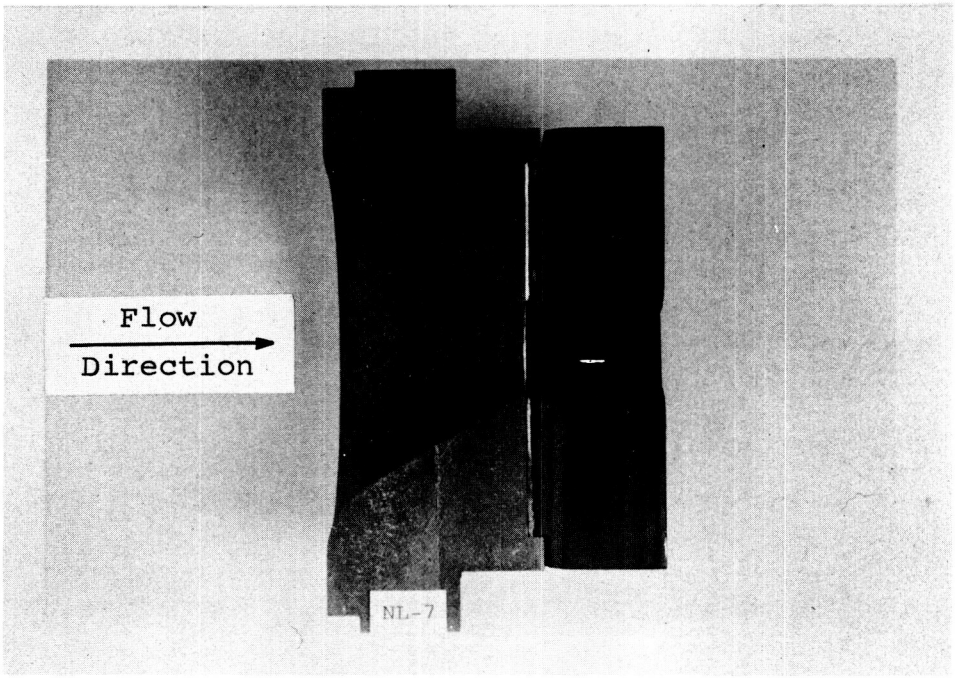

a) MX4926 carbon phenolic (601-01)

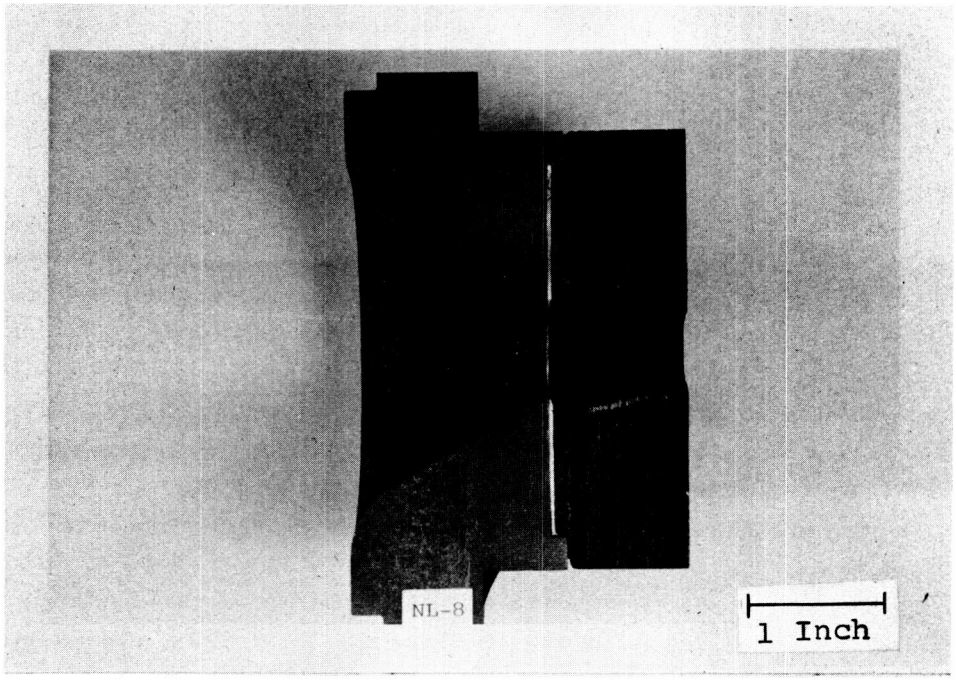

b) MX4500 graphite phenolic (601-02)

Figure 29.- Sectioned test nozzles.

	Average Surface Erosion Rate, mils/sec	
	With Upstream Decomposition	Without Upstream Decomposition
MX4926 carbon phenolic	1.06	1.46
MX4500 graphite phenolic	0.97	1.56

An increase in erosion rate of about 50 percent occurred in both cases. The definition of how realistic this comparison is must await more definitive testing and analysis.

3.6 Conclusion

Carbon phenolic and graphite phenolic materials were tested under conditions that simulated the combustion products environment of a typical solid propellant. The char thermal conductivity and performance of the materials were determined and studied. Based on these test firings, as presented above, the following conclusions and comments are offered:

1. Char thermal conductivity was successfully obtained under dynamic conditions for:

   MX4926 carbon phenolic - 90° layup
   0° layup

   MX4500 graphite phenolic - 90° layup
   0° layup

2. The surface erosion performance of MX4926 carbon phenolic and MX4500 graphite phenolic are quite comparable. The graphite phenolic exhibits a slightly better erosion performance, however.

3. The insulation capability of MX4926 carbon phenolic, as evidenced by the measured char depth, is better than that of MX4500 graphite phenolic. This is a direct result of the lower virgin material and char thermal conductivities for the carbon phenolic.

4. The above conclusions on the specific materials apply in general to carbon phenolics and graphite phenolics as material classes provided the resin percents fall in the approximate range of 30-35.

5. The surface erosion results for the simulation conditions and geometry are indicative of but not equivalent to those that would be expected in the actual combustion products environment for a typical solid rocket nozzle.

6. No definitive results were obtained for the effect of upstream ablation on surface erosion downstream due to problems in the experimental approach.

7. As concluded in Section 2, the Aerotherm ablation computer programs are effective tools in the analysis of ablative material performance.

4. STUDY OF SPECIAL PROBLEMS

A small part of the program effort was devoted to the study of special problems that arose or of areas of interest that appeared particularly pertinent during the contract period. Four specific studies were performed under this task. The major effort was the analysis of the theoretical approach to calculating heat and mass transfer coefficients and a study of the means of extending this approach to include effects not presently considered, including the effect of upstream ablation. The second study was a calculation of heat flux and heat transfer coefficients for a hypothetical 260-inch motor nozzle which was liquid cooled. The third task effort was a definition of the effectiveness of a quench during cooldown in limiting the internal material decomposition during heat soak. Finally, detailed internal thermal response predictions were supplied to the Air Force for the throat materials of the Aerojet 120-SS-1 nozzle and a UTC Titan IIIC motor nozzle in support of a study to characterize chars. The results of these studies are presented in the following sections.

4.1 Study of Techniques for Calculating Heat and Mass Transfer Coefficients for Material Performance Predictions

Implicit to the successful prediction of thermochemical erosion of ablative materials is the accurate estimation of heat and mass transfer coefficients as input to the ablation predictions. The magnitudes of these coefficients depend upon local boundary layer edge and wall conditions, and on the variations of these conditions at all points along the surface upstream of the particular point being considered. In addition to these considerations, the transfer coefficients are influenced by the nozzle geometry.

Techniques are not presently available for the exact description of the boundary layer (and thence, transfer coefficients) for arbitrary geometries and conditions, particularly for the case of the turbulent boundary layer. At best, semi-empirical techniques have been required to successfully characterize even the simplest cases. In addition, even the restricted exact (or near exact) solutions available are often operationally cumbersome and limited in the number of variables which can be considered simultaneously. For these reasons, at least for the present, the estimation of various transfer coefficients must rely on approximate boundary layer techniques, which are hopefully sufficiently simple to allow operational flexibility, and yet sufficiently detailed to satisfactorily account for the effects of the significant variables which influence these coefficients.

In the past, Aerotherm has made extensive use of the energy integral method presented in Reference 6 for the prediction of heat transfer coefficients, based in part on the apparent adequacy of the technique, (see Figure 30 - taken

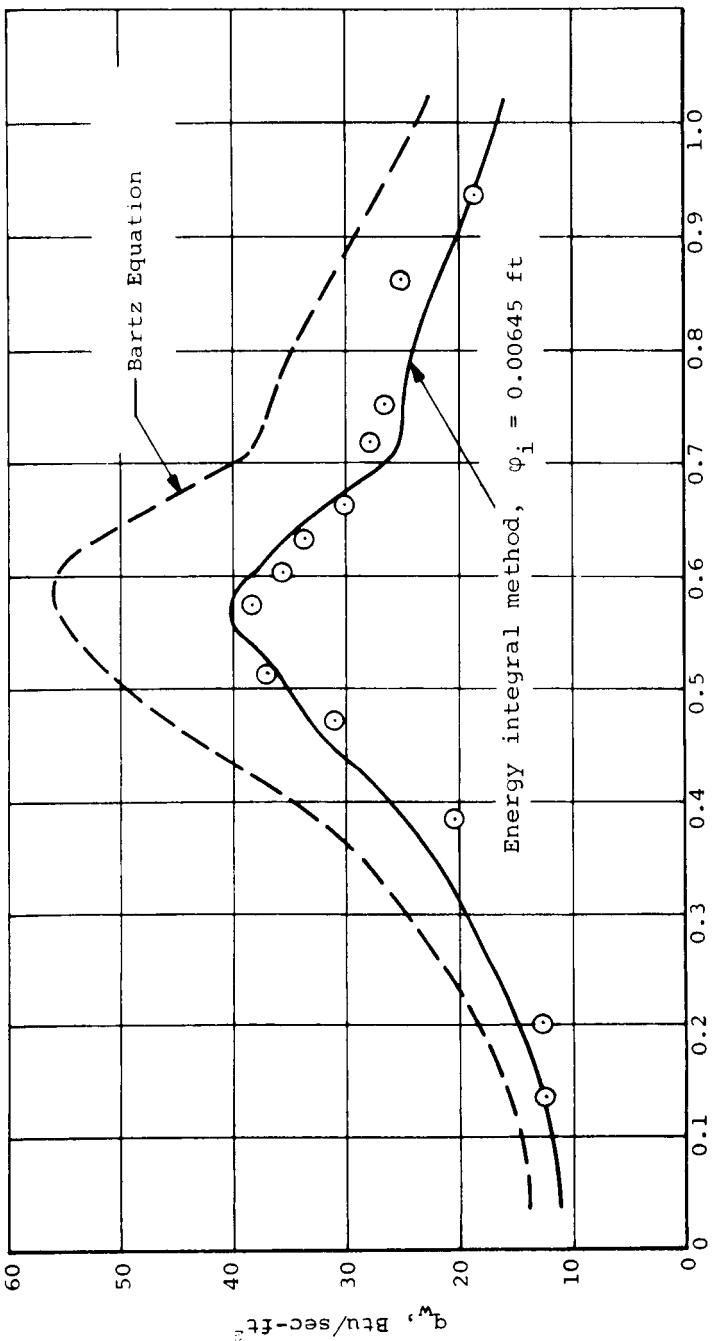

Figure 30.- Comparison of energy integral method results with experimental data from JPL Test 218. (taken from Reference 6)

from Reference 6 where these results are discussed) and based in large part on its simplicity and degree of generality. Recent studies, however, have indicated the necessity of a boundary layer prediction technique of even greater generality; for example, in ablating nozzles, consideration should be given to the effects of ablation (blowing) upstream of the point of interest on both the energy and mass boundary layers. Because of the attractive features of the energy integral method, effort has been successfully applied to the modification of this technique under the present program to increase its generality and accuracy. Concurrent with these developments was the comparisons of the technique with certain available exact solutions in order to assess its accuracy as applicable to rocket nozzles.[12] The detailed results of these modifications and comparisons with exact solutions are presented in Appendix A. The following paragraphs summarize these comparisons and also present the results of an extension of the basic technique to include the effects of upstream blowing (ablation).

In comparisons with exact solutions, it was found, in general, that the energy integral technique correctly predicts the direction of the influence of all variables considered, if not the magnitude of their effects. The technique slightly overpredicts non-isothermal wall effects, but underpredicts the effects of variable freestream velocity (pressure gradient) for the two-dimensional geometries examined. For two-dimensional, axisymmetric geometries, the approximate results for variable freestream velocity, although below the exact results, were in error by a lesser extent than for a two-dimensional geometry. It was also found that the technique is valid for cases where the wall enthalpy is either always above or always below the level of freestream stagnation enthalpy but is not valid for cases where the wall enthalpy "crosses over" the stagnation enthalpy. Based on these comparisons, it is believed that the concepts of the technique provide a firm and valid basis for modifications to consider the effects of other variables. These modifications are discussed in Appendix A. It should also be noted that the technique is appropriate to the calculation of mass-transfer coefficients where its applicability and restrictions are similar to those for the calculation of heat-transfer coefficient.

The energy integral technique was used to estimate the effects of significant upstream ablation on the nozzle heat transfer coefficient downstream of this region of high ablation. The Aerojet 120-SS-1 nozzle was considered, the region of high ablation being the subsonic region in which V-44 elastomeric was

[12] Although laminar conditions rarely prevail in a rocket nozzle, the technique is compared for the most part with available exact laminar boundary layer solutions because of the paucity of exact solutions for the turbulent case. Nevertheless, since the basis of the technique is the same for both the laminar and turbulent cases, a good comparison with exact solutions for the laminar case is indicative of the adequacy of the technique for the turbulent case.

the exposed material. The calculation was performed by numerical integration of the energy integral equation, Equation (A23), using the linearized form of Equation (A18). In order to simplify the calculation, the effects of variable boundary-layer properties were not considered. In addition, the boundary layer was assumed to be turbulent over its length, and the origin of the boundary layer was assumed to be at the juncture of the grain and the aft closure. An early time during the firing was considered which established the instantaneous origin of the boundary layer and provided reasonable estimates of the surface profile. Instantaneous blowing rates were estimated through consideration of the final experimental material erosion profiles. To initiate the integration, an estimate was made of the boundary-layer energy thickness at the beginning of the elastomeric insulation by allowing a short running length upstream of the elastomeric ($\Delta\frac{x}{r^*} = 0.1$), and computing φ from Equation (A4). In the linearized form of Equation (A18), a value of $\lambda = 0.3$ was selected to yield results more representative of the results for $\lambda = 0.4$ in the exponential form of Equation (A18) for the range of blowing rates.

Results of these calculations are presented in Figure 31 which includes the heat transfer coefficient that would be obtained along a non-ablating wall $C_{H_{\beta=0}}^*$ (similar to those results obtained from the present boundary layer computer program), the coefficient resulting from upstream blowing but zero blowing locally C_H^*, and the coefficient due to upstream and local blowing C_H. These results are discussed below in the light of the present approach to handling the heat-transfer coefficients.

Typically, the Stanton number results (actually $\rho_e u_e C_H$) input to the Charring Material Ablation Program (CMA) are those obtained with zero blowing from the present boundary layer computer program, $C_{H_{\beta=0}}^*$, which is internally corrected in the CMA program by the exponential form of Equation (A18) to account for local blowing. Because of upstream blowing, however, the input values of heat transfer coefficient are higher than the actual "non-ablating-wall" heat-transfer coefficient C_H^*, resulting in general in an overprediction of erosion rates for cases of significant upstream blowing.

In general, the effects of upstream blowing on "non-ablating-wall" heat transfer coefficients are not large for rocket nozzles, being the greatest for this example at the end of the rubber insulation ($x/r^* \approx 0.75$) where the reduction in this coefficient is slightly greater than 16 percent. This reduction decays to about 5 percent at the throat ($x/r^* = 1.72$), due to the lower blowing rates downstream of the rubber insulation. These results do not consider the chemical structure of the boundary layer as influenced by upstream ablation. Chemical effects manifest themselves most significantly in the alteration of mass transfer coefficients, yielding a direct influence on material

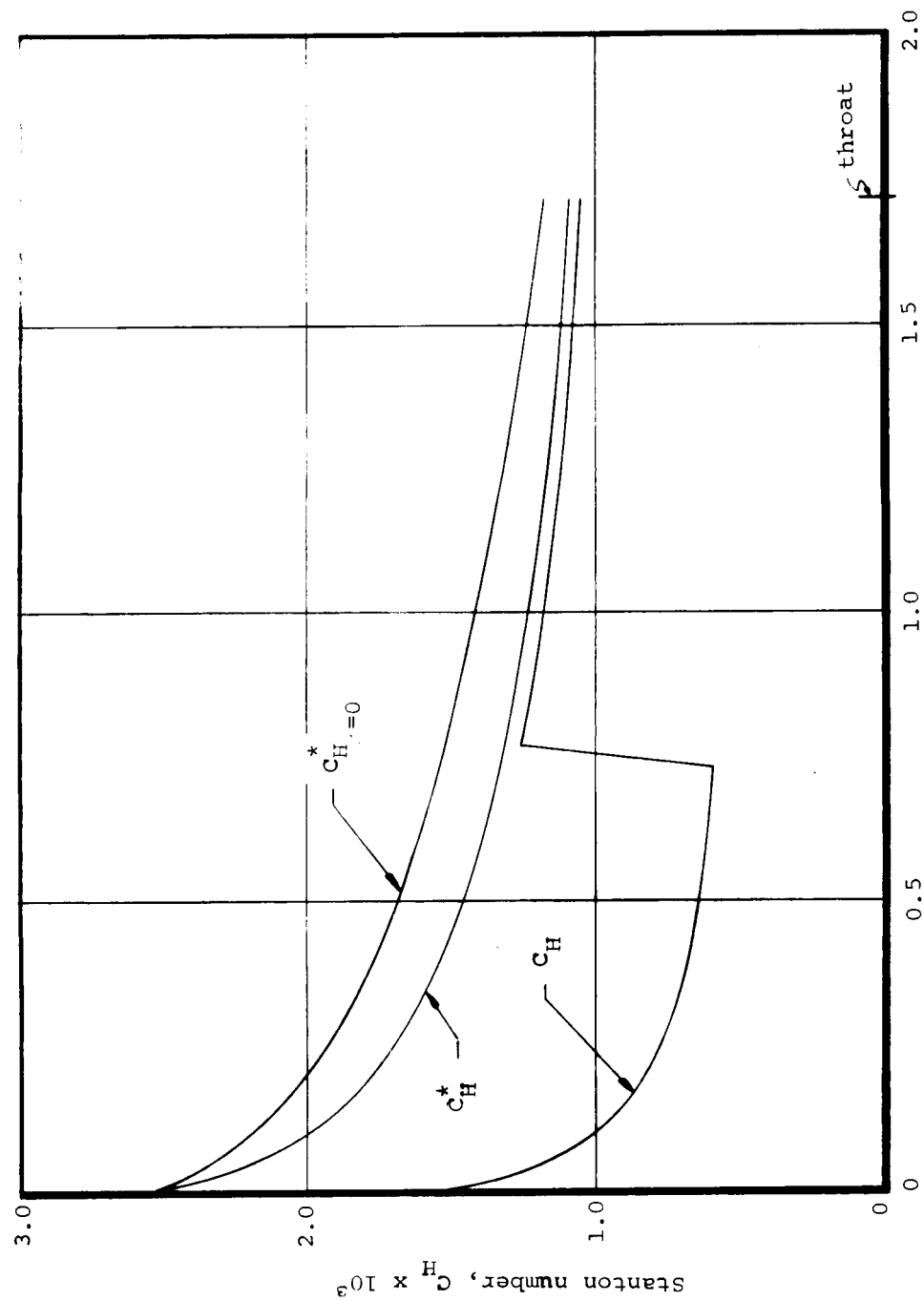

Figure 31.- Examination of the effects of ablation on heat transfer coefficient for the Aerojet 120-SS-1 nozzle.

surface chemical erosion rates. It is believed that these chemical effects can be accounted for through application of the same technique used to calculate heat transfer coefficients, through the mass boundary layer analogy to Equation (A25). However, this effort is outside of the scope of the present contract, but should be included in future studies.

4.2 Heat Flux and Transfer Coefficients for a Liquid-Cooled Large Booster Nozzle

The heat flux and transfer coefficients were calculated for a hypothetical liquid-cooled 260-inch motor nozzle in support of an in-house study being performed at the NASA Lewis Research Center. The boundary layer computer program discussed in the previous section (Section 4.1) and in Section 2.3.2.3 was used to accomplish these calculations. The "hot-side" heat transfer parameters were determined as a function of area ratio for the following conditions:

Aerojet ANB-3105 solid propellant
Chamber pressure - 630 psia
Nozzle contour of Figure 32
Constant (with surface distance) wall temperatures of
$1000^{\circ}F$
$3700^{\circ}F$

The latter wall temperature corresponds to the melt temperature of alumina (Al_2O_3). The results are presented in Figures 33 and 34. The maximum heat flux occurs very close to the throat and, of course, the overall level is higher for the lower wall temperature. This maximum flux at $1000^{\circ}F$ wall temperature is just over 1200 Btu/ft^2-sec. The heat transfer coefficient, $\rho_e u_e C_H$, is presented in Figure 34 (a) and the coefficient based on a temperature driving potential, $h_T = q/(T_o - T_w)$, is presented in Figure 34 (b).

4.3 Effect of Quench on Reducing Char Depth and Internal Decomposition

The effectiveness of quenching a fired nozzle with water or carbon dioxide during the cooldown period, in terms of reducing the char depth and internal decomposition, was investigated for the example of the exit cone of the Aerojet 260-SL-1 nozzle. This was studied through ablation computer calculations of a normal cooldown and a cooldown with a quench 160 seconds after the start of the firing for the following assumptions:

Normal cooldown - Cooling by surface radiation out the exit cone (the assumptions of the predictions of Section 2)

Quench cooldown - Cooling by surface radiation out the exit cone from shutdown to 160 seconds, quench at 160 seconds to a surface temperature of $70^{\circ}F$ at 165 seconds, constant surface temperature of $70^{\circ}F$ from 165 seconds on.

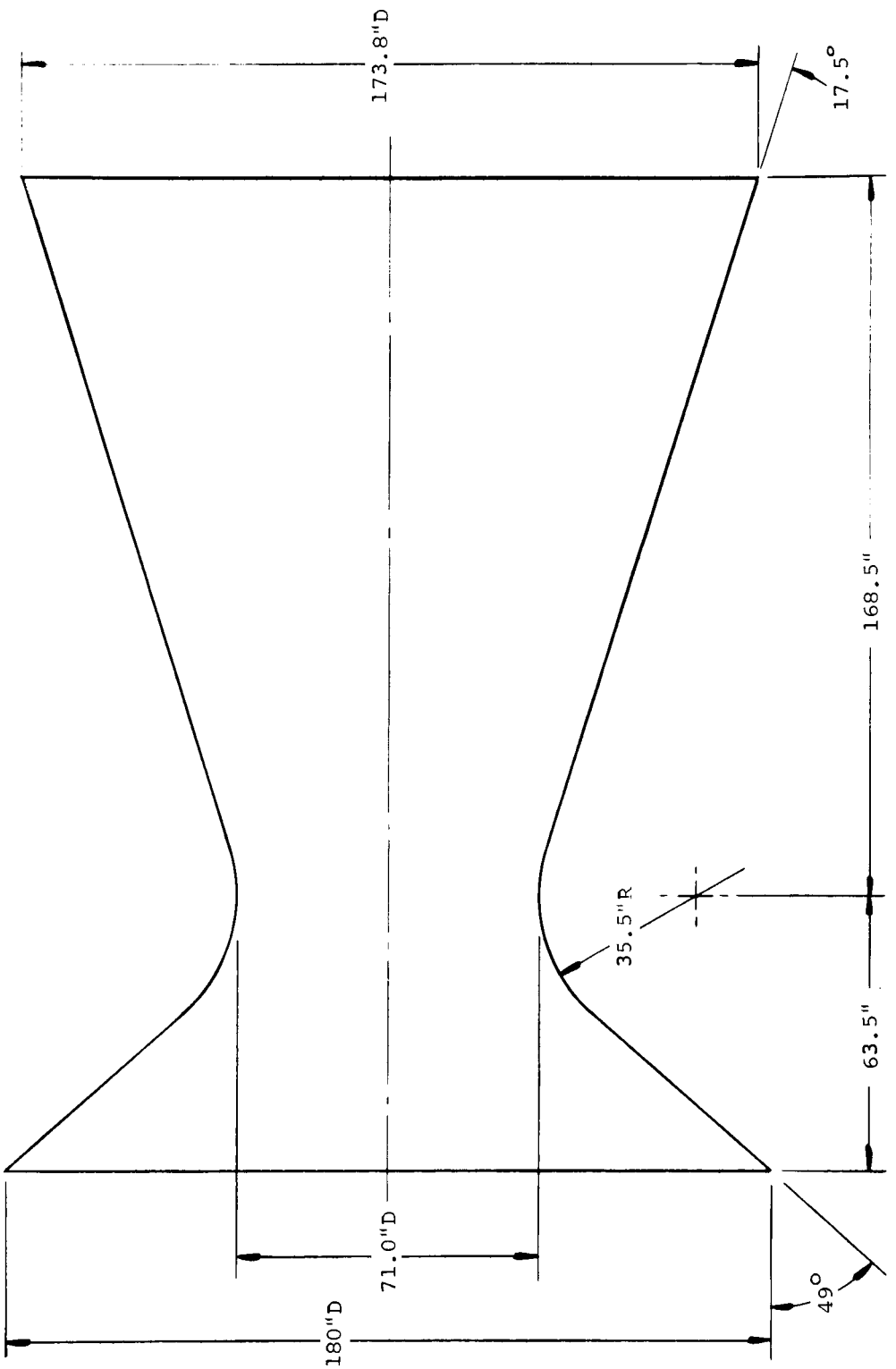

Figure 32.- Assumed nozzle contour for the hypothetical liquid-cooled 260-inch rocket nozzle.

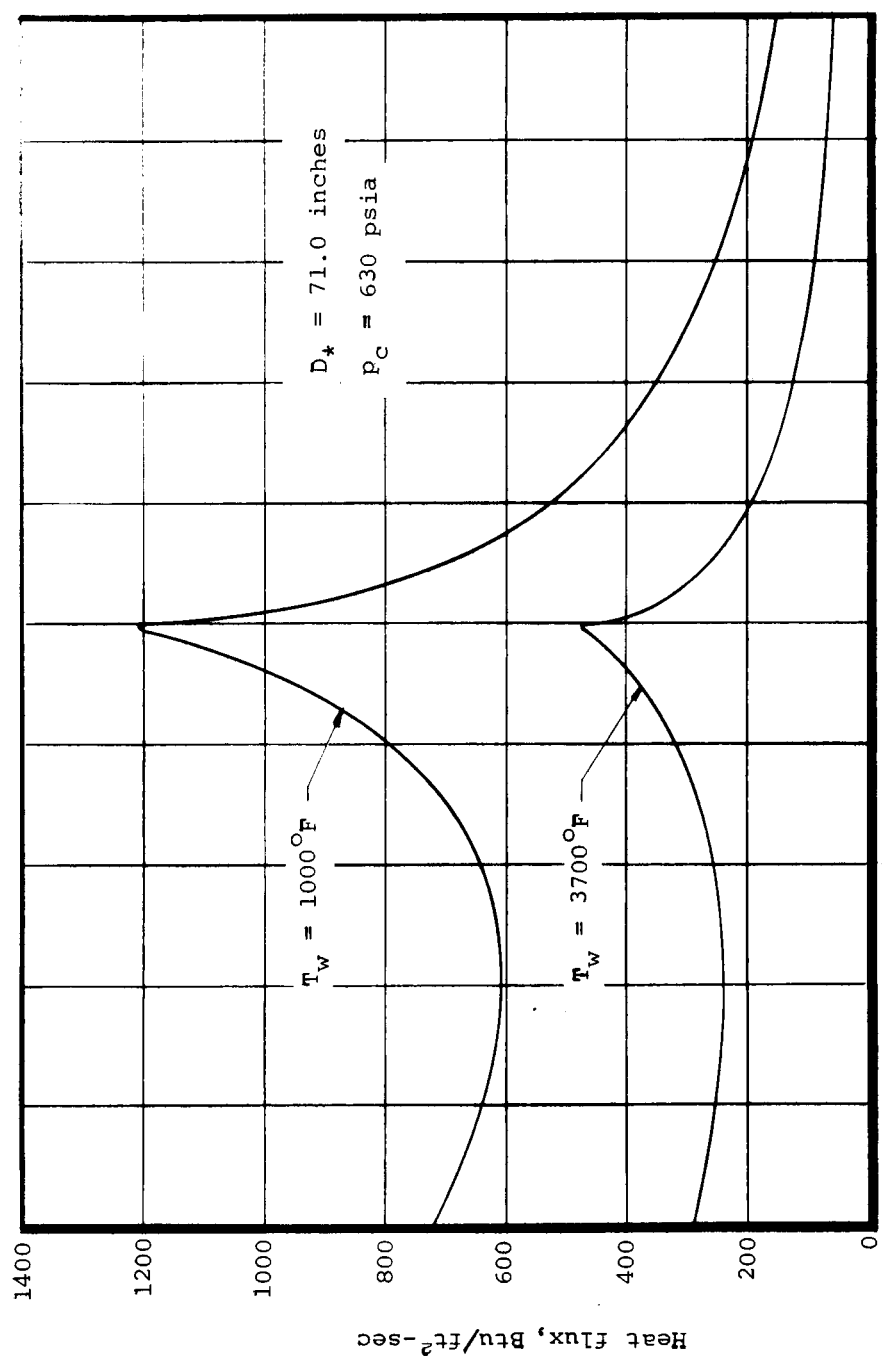

Figure 33.- Heat flux distribution for a hypothetical liquid cooled 260-inch rocket nozzle.

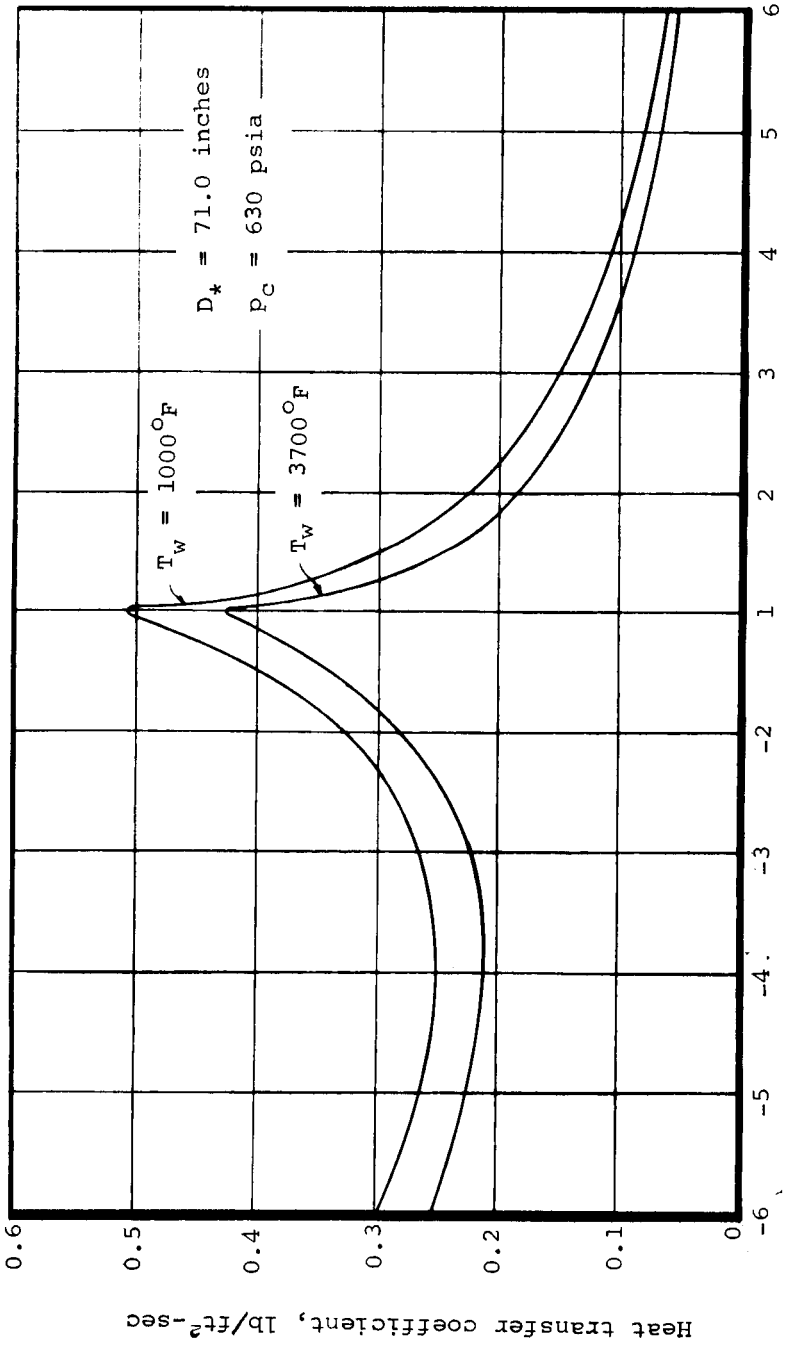

a) $\rho_e u_e C_H$

Figure 34.- Heat transfer coefficients for a hypothetical 260-inch rocket nozzle.

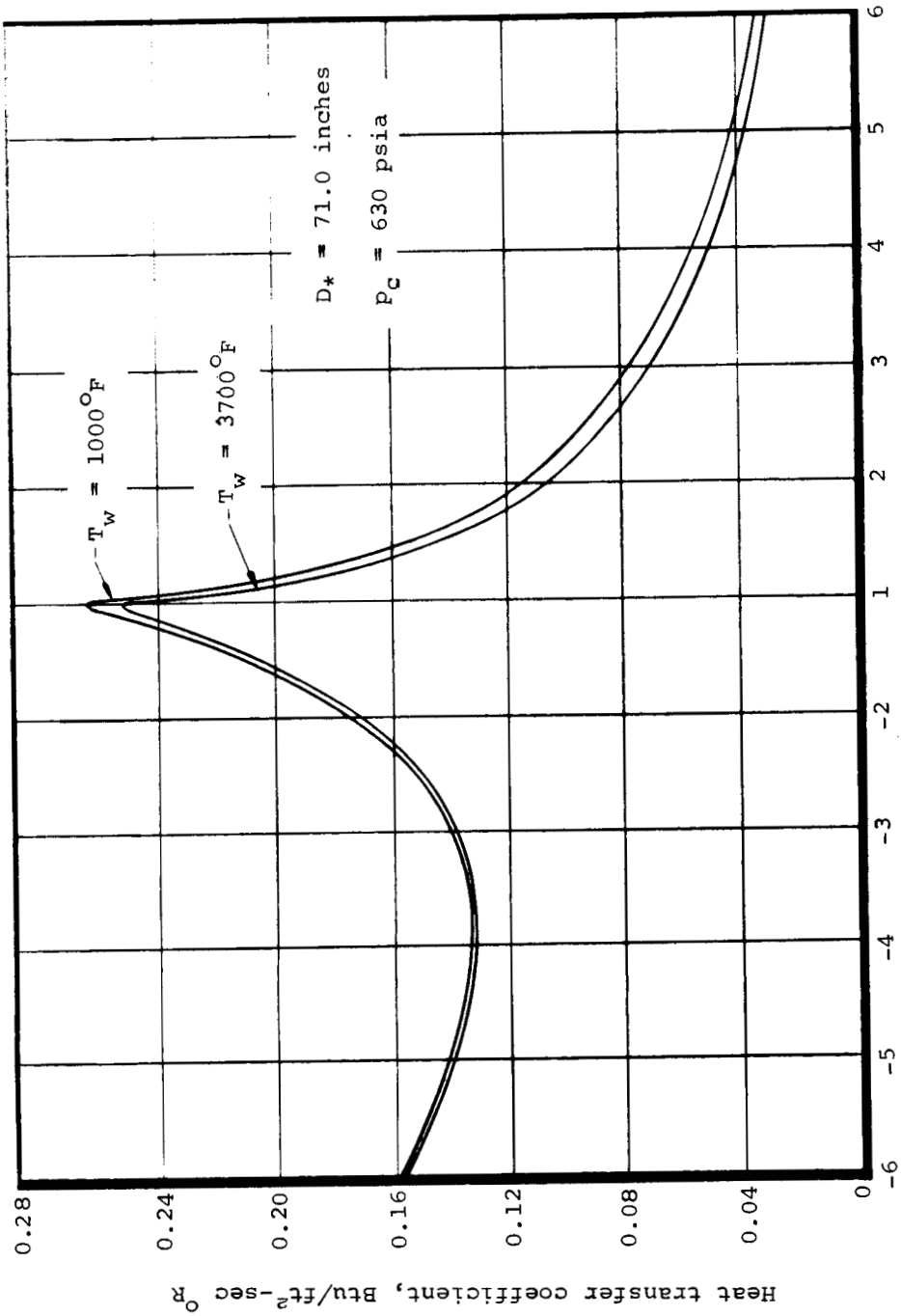

b) $h_T = q/(T_o - T_w)$

Figure 34.- Concluded.

These predictions were made before the final char conductivity results were obtained, but the results in terms of percentage decrease in the significant internal performance parameters are indicative of the magnitude of the quench effects. These results for the two exit cone locations considered in Section 2 for the 260-SL-1 nozzle are:

Area Ratio	Material and Layup Angle	Percent Decrease Due to Quench		
		Char Depth	Pyrolysis Zone Depth	Maximum Depth of 500°F Isotherm
2.5	MX4926 carbon phenolic, 17.5°	5	10	27
3.8	FM5131 silica phenolic, 17.5°	4	8	23

The quench is rather ineffective in reducing the char depths and pyrolysis zone depths but it is effective in limiting the penetration of the 500°F isotherm. It should also be noted that the magnitude of the quench effect is also somewhat optimistic. The time after shutdown at which the quench was assumed to start was shorter than "normal" and the assumed rapid surface temperature decrease to 70°F is probably optimistic.

4.4 Internal Thermal Response Predictions

Calculations of the internal thermal response for the throat materials of the Aerojet 120-SS-1 and UTC UA-1205-10 nozzles were supplied to The Boeing Company in support of a current Air Force Materials Laboratory Contract AF 33(615)-3804. The contract is concerned with the experimental characterization of chars and the generation of representative chars under laboratory conditions. Specific cases under consideration are the throat material of the 120-SS-1 nozzle and the throat material of one of the UTC Titan IIIC development motor nozzles. The internal thermal response calculations provided by Aerotherm are being used to define the thermal history of the two material parts which, in turn, is being used to define the requirements for generating a representative char sample under laboratory conditions. Also, the predicted internal density distributions of the two materials are being compared with actual measurements being made under the contract.

Recall that the predictions for the two nozzles in question were performed under the program task discussed in Section 2. For the 120-SS-1 nozzle throat, however, the predicted surface erosion depth was slightly higher than the maximum erosion depth measured and significantly higher than the average measured erosion depth (Figures 8 and 11). Therefore, to allow a direct comparison of internal response for the same approximate predicted and measured erosion depths,

a second prediction was made such that the predicted erosion depth was equal to the measured average erosion depth. This was accomplished by appropriately reducing the input heat (and mass) transfer coefficient to the Charring Material Ablation computer program. These results supplied to Boeing are presented in Figures 35 and 36, Figure 35 being the transient response as a function of time and Figure 36 being representative temperature and density distributions through the firing. In addition, the complete computer program output was sent to Boeing. Since the specific nozzle, the firing conditions, and the surface erosion depth were unknown for the UTC nozzle material sample, no calculations in addition to those of Section 2 were performed. The results are presented in Figures 12 and 15, and, together with the complete computer program output, were transmitted to Boeing.

5. AREAS FOR FUTURE STUDIES

Problem areas of nozzle design and material performance that require future study, as indicated in part by the results of this contract and in part by the general experience of Aerotherm Corporation and the rocket industry, were defined under this contract and possible approaches to their solution were outlined. These areas for future study encompass the more effective use of currently available materials, the study of new material possibilities, and study and analysis of material performance to better define material characteristics and capabilities. These recommendations are presented in the following sections.

5.1 Reduction of Nozzle Cost

The present day cost of large ablative nozzles is surprisingly high. There are several potential areas in which realistic and significant cost savings can be effected as outlined below:

Thinner ablative material parts

Define thickness requirements for thermal protection and structural integrity; a factor of 2 cut in present day standards appears possible

Lower cost ablative materials

Define the acceptability of glass phenolic and asbestos phenolic for high area ratios in the exit cone; define the minimum supersonic area ratio for practical use of silica phenolic; study feasibility of more extensive use of these and elastomeric materials in the subsonic region

Lower cost fabrication techniques

Wider use of autoclave cure and nylon overwrap, eliminate or reduce the use of bias tape; define capabilities and reliability of snap cure type fabrication; consider the merits of molded parts (castables)

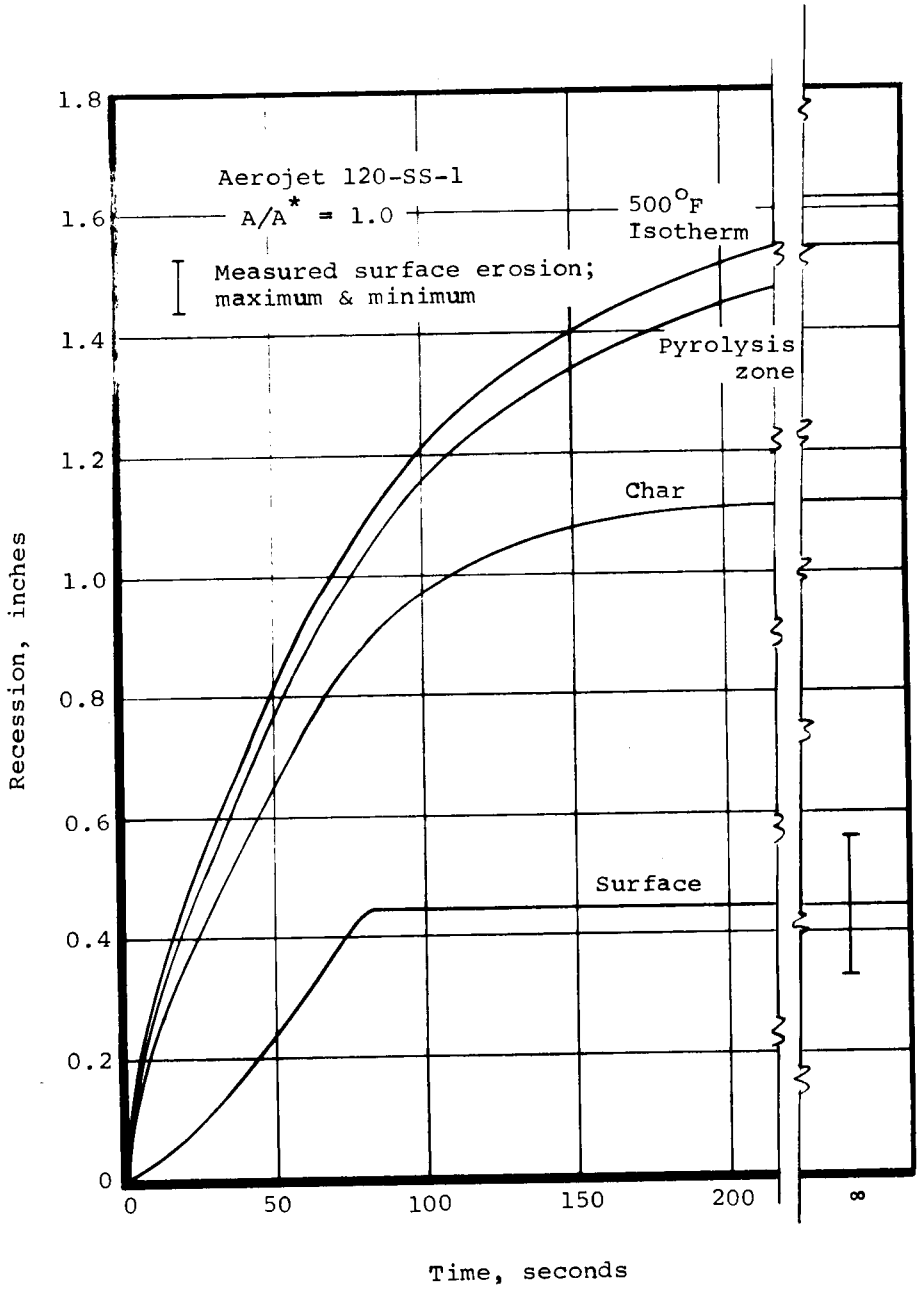

Figure 35.- Predicted transient response of the throat material for the 120-SS-1 nozzle for equal predicted and measured average surface erosion depths.

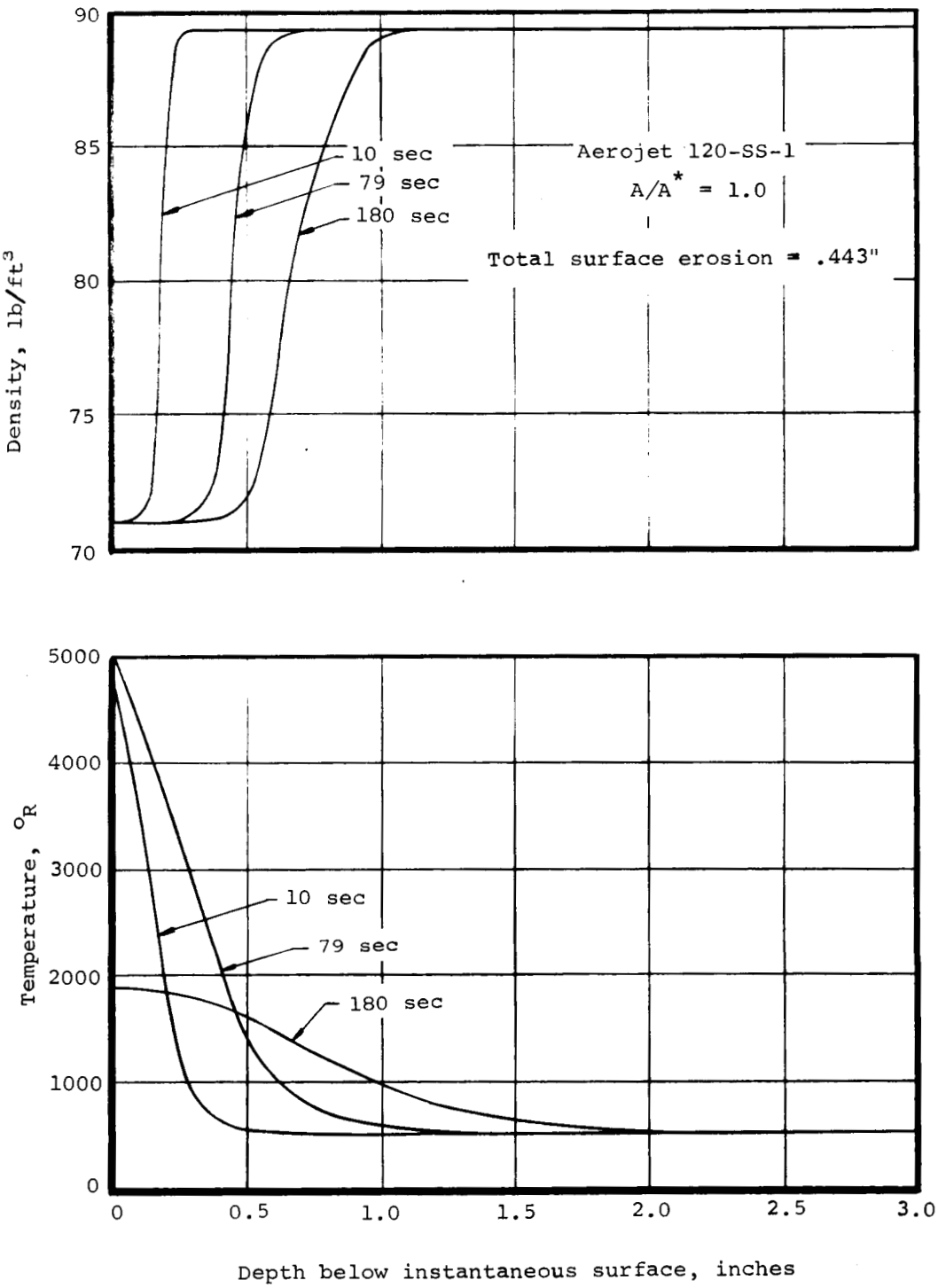

Figure 36.- Predicted temperature and density distributions for the throat of the 120-SS-1 nozzle for equal predicted and measured average surface erosion depth.

New materials

Investigate the capabilities of rayon phenolic and Creslan phenolic for throat extension and exit cone applications; investigate the capabilities and thickness reduction possible with dual fabric materials (e.g., carbon fabric near surface with transition to silica fabric in depth); investigate the capabilities of carbon paper phenolics; investigate the possibilities for higher resin percents and larger amounts of filler in the standard cloth phenolics

5.2 Reuseable Nozzles

The reuse of ablative nozzles offers the potential of time and cost savings and therefore should be investigated further. The following should be considered:

Methods of refurbishment

Investigate the material performance and cost tradeoffs for no refurbishment except superficial cleaning, reimpregnation of the char, and machining to virgin material (this to include consideration of material thickness requirements, number of reuses)

Effects peculiar to sea water immersion

Approaches to repairing or replacing damaged or critical parts

5.3 Effects of Manufacturing and Fabrication Faults on Material Performance and Means of Correction Where Necessary

The acceptability limits and possible fixes associated with the following faults should be defined:

Cracks
Voids
High volatiles (water, hydrocarbons)
Nonuniform layup
Surface ripple
Off-spec resin content
Incomplete cure

5.4 Properties and Performance Mechanisms of Silica Phenolic

The properties and surface erosion mechanisms for silica phenolic are not adequately defined. A program similar to that performed under this contract for carbon and graphite phenolics should be initiated. This would include:

Determination of char thermal conductivity

Determination of char specific heat

Study of surface erosion mechanisms and definition of their importance -

Surface chemical reactions

Liquid layer runoff

Solid phase chemical reactions

5.5 Properties and Performance Mechanisms of Elastomeric Materials

The popular and increased use of elastomeric materials in large booster nozzles, both conventional and submerged, and the quantities required dictate the need for a better understanding of these materials. Further programs similar to that for silica phenolic, Section 5.4 above, should be performed.

5.6 Effect of Upstream Ablation on Downstream Erosion

The studies of this contract should be continued through further testing to quantitatively define the effect of upstream ablation on downstream erosion. Also, techniques to allow its inclusion in the prediction of material performance according to the recommendations of Section 4.1 should be developed.

5.7 Flow Field for Submerged Nozzles

The flow field around the reentrant portion of submerged nozzles is presently ill-defined. Its definition is critical to the proper design of nozzle ablative material components and accurate prediction of material performance. Cold flow tests should be performed and correlated with analytic prediction techniques that can be used in support of nozzle design.

5.8 Relation of During-Fire Performance to Post-Fire Observation and Measurement

Post-fire observations and measurements after heat soak and quench may not be representative of the actual material performance during a firing. Effects associated with quench, cooldown, heat soak, and post-fire measurement techniques on the post-fire interpretation of material performance should be defined.

5.9 Development and Use of Instrumentation to Further Characterize Material Performance

The transient measurement of surface erosion depth, char depth, and internal material pressure (due to pyrolysis gas generation) during a nozzle firing would provide valuable information on the overall response of ablative materials. Instrumentation to accomplish these measurements should be developed and used in the analysis of material performance.

5.10 Char Layup Angle Warp Phenomenon

This phenomenon should be better defined in terms of when it occurs, during the cooldown or during the firing, what causes it, and what its significance is in terms of interpreting insulation effectiveness.

5.11 Material Performance in the Subsonic Region of Nozzles

The present study concentrated on the low area ratio subsonic region, throat, and supersonic region. Further effort should be concentrated on the higher area ratio subsonic region and subsonic regions of submerged nozzles. This should include the type of effort performed herein and a study of particle impact effects and desirable materials for this region.

5.12 More Extensive and Effective Use of Theoretical Material Performance Prediction Techniques in Support of Nozzle Design and in Post-Firing Analysis of Material Performance

The use of prediction techniques as presented herein should be encouraged in future nozzle design and in further analyses of material performance in past and future motor firings. This would provide the material manufacturer, part fabricator, nozzle designer, and engineer with a better understanding of ablative materials, and hence would promote their more economic use and provide a more definitive base for nozzle design.

APPENDIX A

REVIEW, EXTENSIONS, AND MODIFICATIONS OF THE CALCULATIONS OF HEAT TRANSFER COEFFICIENTS IN ROCKET NOZZLES

A.1 EXAMINATION OF THE ENERGY-INTEGRAL TECHNIQUE

The energy-integral technique of Reference 6 appears to account for the effects on heat transfer coefficient of variable wall temperature and free stream velocity on both two-dimensional (2-D) and two dimensional, axisymmetric (2-D-A) configurations for both laminar and turbulent boundary layers without transpiration. Comparisons of solutions obtained from the method with applicable exact or near exact solutions are presented in this section.

It is well to indicate the method in its simplest form through introduction of the basic differential equation, and presentation of the solution of the differential equation, as follows.

The integral form of the boundary layer energy equation for the low speed constant property boundary layer for either 2-D or 2-D-A geometries is

$$\frac{d\varphi}{dx} = C_H - \varphi \frac{d}{dx} \ell n \left[r\rho_e u_e (T_{te} - T_w) \right] + \beta \qquad (A1)$$

where for 2-D geometries the radius, r, is everywhere equal to unity, or equal to the actual surface radius for 2-D-A geometries, and x is the surface coordinate. Considering the case of an isothermal flat plate without transpiration, the latter two terms in Equation (A1) are identically zero. For this same case, the heat transfer coefficient is known to vary for a wide range of Reynolds numbers approximately as follows

$$C_H = \frac{a}{Pr^{2/3} (Re_x)^m} \qquad (A2)$$

where the constants and exponents for laminar or turbulent boundary layers are

	a	m
laminar	0.332	0.5
turbulent	0.0296	0.2

Inserting Equation (A2) into (A1), and integrating with surface distance, x, an alternate heat transfer correlation equation for a flat plate, in terms of Reynolds number based on energy thickness, Re_φ, can be derived

$$C_H = \left[\frac{a}{Pr^{2/3} (Re_\varphi)^m (1 - m)^m} \right]^{\frac{1}{1-m}} \qquad (A3)$$

The energy integral method of Reference 6 (originally developed independently in References 20 and 21) assumes that Equation (A3) is valid also for boundary layers with finite axial pressure gradient and wall temperature gradient on 2-D and 2-D-A bodies. Applying Equation (A3) to Equation (A1) and assuming $\beta = 0$ (no transpiration), a first-order differential equation of the Bernoulli-type results which can be formally integrated to yield the variation of energy thickness, φ, with surface running length, and with arbitrary distributions of surface temperature and free stream velocity. This variation is (from Equation A-27 of Reference 6)

$$\varphi^{\frac{1}{1-m}} = \left\{ \frac{\left[r \rho_e u_e (T_{te} - T_w) \right]_i \varphi_i}{r \rho_e u_e (T_{te} - T_w)} \right\}^{\frac{1}{1-m}}$$

$$+ \frac{1}{\left[r \rho_e u_e (T_{te} - T_w) \right]^{\frac{1}{1-m}}} \int_{x_i}^{x} \left[\frac{a \, r \rho_e u_e (T_{te} - T_w)}{Pr^{2/3} \left(\frac{\rho_e u_e}{\mu} \right)^m (1 - m)} \right]^{\frac{1}{1-m}} \frac{dx}{1-m} \qquad (A4)$$

Equation (A4) may be inserted into Equation (A3) to calculate the heat transfer coefficient, C_H. In Equation (A4), the subscript, i, refers to parameters prevailing at the lower limit of integration, x_i. This lower limit may be at a stagnation point on a body, or at some point on the body where boundary layer parameters are known and can be used as input to the estimation of parameters downstream of x_i. A typical example is the case of flow over a sphere where flow is initially laminar, but undergoes transition to turbulent flow. For the laminar portion, x_i (and φ_i) is zero, and for the turbulent portion, x_i is at the point of transition and φ_i is the value of φ at transition.

For the sake of simplicity (but without a loss in generality for the studies herein), it is assumed that the boundary layer is either all laminar or all turbulent downstream of the point of initiation of the thermal boundary layer, x_i. Making the simplification of $\varphi_i = 0$ at $x = x_i$ and substituting Equation (A4) into Equation (A3), a closed form expression for the heat transfer Stanton number can be developed and cast in the form of the flat plate relation (see Reference 2)

$$C_H = \frac{a}{Pr^{2/3}\left[\frac{\rho_e u_e (x - x_i)}{\mu}\right]^m G^m} \qquad (A5)$$

The parameter, G, is a "stretching" factor on the isothermal flat plate relation to simultaneously account for variable free stream velocity, axisymmetric geometry (if appropriate), and variable wall temperature, and is defined below

$$G = \left[\frac{\left(\frac{\rho_e u_e}{\mu}\right)^m Pr^{2/3}}{r\,\rho_e u_e c_p (T_{te} - T_w)}\right]^{\frac{1}{1-m}} \left[\frac{1}{(x - x_i)}\right] \int_{x_i}^{x} \left[\frac{r\,\rho_e u_e c_p (T_{te} - T_w)}{\left(\frac{\rho_e u_e}{\mu}\right)^m Pr^{2/3}}\right]^{\frac{1}{1-m}} dx \qquad (A6)$$

Equation (A5) will be used for subsequent comparisons of the results of the method with "exact" solutions in the following subsections, with the restriction, however, of constant properties.

A.1.1 Nonisothermal Wall Effects

The effects on C_H of a step change in wall temperature on a flat plate have been studied in References 22 and 23 for the laminar and turbulent boundary layers, respectively. Results have been obtained from certain approximations of the behavior of the thermal boundary layer within an already established momentum or velocity boundary layer, the so-called thermal entry length problem. Although the solutions are approximate, comparisons of solutions with data are sufficiently favorable to suggest that the solutions are for all practical purposes exact. It is convenient to express results in terms of the value of C_H that would exist along an isothermal flat plate by a ratio of actual C_H to the value of C_H for an isothermal plate, C_{H_T}. Results for the step wall temperature change on the flat plate are:

$$\frac{C_H}{C_{H_T}} = \frac{1}{\left[1 - \left(\frac{x_i}{x}\right)^a\right]^b}, \quad x \geq x_i \qquad (A7)$$

	a	b
laminar	3/4	1/3
turbulent	9/10	1/9

Solutions for arbitrary distributions of wall temperature can be obtained by superposition of an infinite number of small steps. Solutions have been obtained for the exemplary case of a step wall temperature change followed by a linear variation of wall temperature. For simplicity, if the step wall temperature change is assumed to occur at the plate leading edge, then the Stanton number downstream of the step change varies as follows

$$\frac{C_H}{C_{H_T}} = \frac{1 + A\left(\frac{d}{c}\right)x}{1 + \left(\frac{d}{c}\right)x} \tag{A8}$$

for the wall temperature variation

$$T_{te} - T_w = c + dx$$

The values of A are 1.612 and 1.134 for laminar and turbulent flow, respectively (References 23 and 24). The behavior of Equation (A8) with $(d/c)x$ is of some interest. For example, for a step wall temperature change only ($d = 0$, $c \neq 0$), $C_H/C_{H_T} = 1.0$, and the variation of C_{H_T} is the variation for an isothermal plate. For large absolute values of $(d/c)x$, $C_H/C_{H_T} = A$. For negative (d/c) (temperature change downstream of the step opposite in direction to the step change), certain singularities are evident in Equation (A8), singularities which however have real physical significance. For example, when $(d/c)x = -1$, Equation (A8) goes to infinity, which simply means that the wall heat flux, $\rho_e u_e C_H c_p (T_{te} - T_w) = q_w$, is finite but with zero wall to freestream temperature difference (a condition which can be physically realized). For $A\left(\frac{d}{c}\right)x = -1$, the wall heat flux is zero with a finite temperature driving potential (also a real phenomenon).

The "exact" results presented above have significance in terms of results obtained for the same examples from the energy integral method as presented below. These "exact" cases are, of course, special exemplary cases within the overall capabilities of the energy integral method. The isothermal flat plate Stanton number used here is Equation (A5) with $G = 1.0$ (see Equation (A6) where all terms in the integrand cancel terms outside the integrand for this case). Non-isothermal wall conditions result in a value of G different from unity, such that

$$\frac{C_H}{C_{H_T}} = \frac{1}{(G)^m} \tag{A9}$$

Evaluating G for the step temperature change yields

$$\frac{C_H}{C_{H_T}} = \frac{1}{\left[1 - \frac{x_i}{x}\right]^m}, \quad x \geq x_i \tag{A10}$$

which is similar in form and magnitude to the exact solution, Equation (A7). As before, solutions for arbitrary temperature distributions could be obtained through superposition of an infinite number of step changes. Equation (A7) compares more favorably with appropriate data than does Equation (A10) (see Reference 25, for example), such that if the superposition approach is employed which is no more or less difficult using either Equation (A7) or (A10), the more exact Equation (A7) is preferable. However, an approximate solution for arbitrary temperature distributions can be obtained simply through evaluation of G in Equation (A9) for the prescribed distribution. Using the temperature variation which was specified for the exact solution of Equation (A8), Equation (A9) yields

$$\frac{C_H}{C_{H_T}} = A \left\{ \frac{\left[1 + \left(\frac{d}{c}\right)x\right]^{\frac{1}{1-m}} \left(\frac{d}{c}\right)x}{\left[1 + \left(\frac{d}{c}\right)x\right]^{\frac{2-m}{1-m}} - 1} \right\}^m \tag{A11}$$

where $A = \left(\frac{2 - m}{1 - m}\right)^m = 1.732$ (laminar), $= 1.176$ (turbulent)

For large positive value of $(d/c)x$, $C_H/C_{H_T} = A$, for which the approximate results are about 7.5 and 3.5 percent greater than the exact results for the laminar and turbulent cases, respectively. For all positive values of $(d/c)x$, the errors in the approximate results are equal to or less than those for large values of $(d/c)x$ indicated above, yielding the conclusion that the approximate technique accounts for non-isothermal wall effects in a simple and highly satisfactory manner for positive values of (d/c). For the case of arbitrary wall temperature distribution, it is inferred from the above comparison that as long as the wall temperature is either always lower or always higher than the freestream temperature (which is the case for most practical applications), then the approximate solution will yield highly acceptable results.

This technique fails, however, for cases when the wall temperature is both above and below freestream temperature as the flow progresses along the surface. For the example above, certain arguments in Equation (A11) become imaginary when the wall temperature becomes equal to the freestream temperature. Unlike the exact solution to this example, Equation (A8), in the approximate solution when the wall-to-freestream temperature difference is zero, so also is wall heat flux, and vice-versa.

A.1.2 Effects of Variable Freestream Velocity Along an Isothermal Wall

No exact solutions are available for the thermal boundary layer for the turbulent case with arbitrary freestream velocity distributions. Exact similarity solutions have been obtained, however, for the laminar boundary layer along an isothermal wall in wedge flow ($u_e \propto x^n$) in Reference 26. Results from the energy integral technique will be compared with the exact laminar solutions in this subsection, the degree of comparison for the laminar case being presumed to be an indicator of the adequacy for the turbulent case, since the method for the two cases are identical in concept.

For the constant property boundary layer along an isothermal 2 - D wall, the expression for G, Equation (A6), is ($x_i = 0$)

$$G = \frac{1}{u_e x} \int_0^x u_e dx = \frac{1}{n+1} \tag{A12}$$

for $u_e \propto x^n$.

A parameter convenient for comparison with exact laminar wedge flow solutions can be obtained through insertion of Equation (A12) into Equation (A5) and rearranging to yield

$$C_H Pr Re_x^{1/2} = 0.332 Pr^{1/3} (1 + n)^{1/2} \tag{A13}$$

Equation (A13) is compared with exact results from Reference 26 in Figure A1 where it is seen that the direction of change in heat transfer coefficient with acceleration ($n > 0$) or deceleration ($n < 0$) is predicted by the energy integral technique, but not the magnitude of the change. Nevertheless, for Prandtl numbers near unity, for the range of the exponent, n, considered in Figure A1, the approximate results are in error by about 20 percent or less. Since the correction to the flat plate relation for turbulent flow is $(1+n)^{0.2}$, a much smaller correction than for the laminar case ($(1+n)^{0.5}$), it is inferred that the energy integral method satisfactorily accounts for the effects of variable freestream velocity on heat transfer coefficient, particularly for the rocket nozzle case where the boundary layer is normally turbulent in the critical regions of concern.

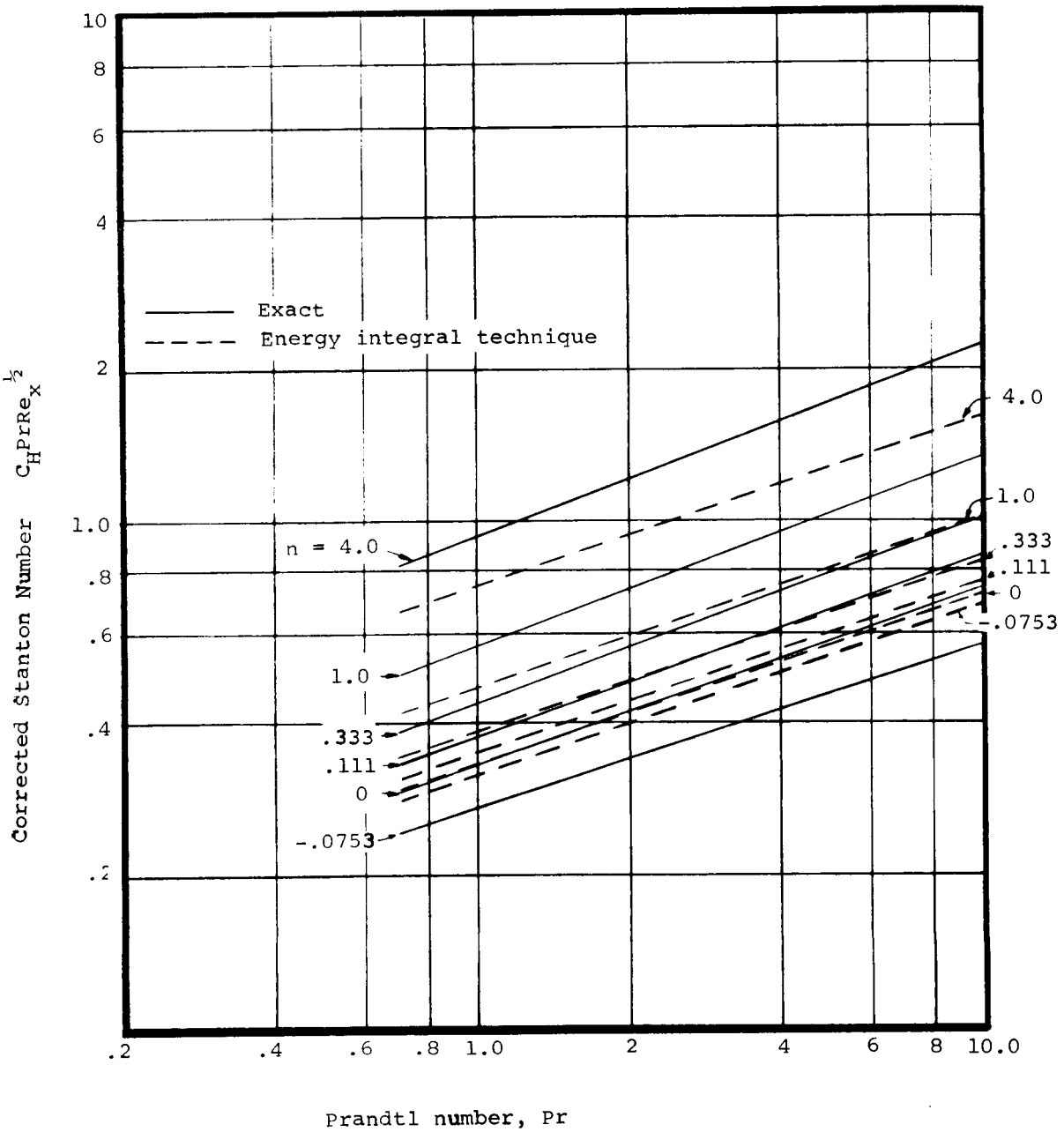

Figure A1.- Comparison of exact and energy integral technique Stanton numbers for $U_e = c\, x^n$ (laminar boundary layer).

A.1.3 Effects of the Type of Two-Dimensional Geometry

The energy integral technique can be compared with exact laminar results for both types of two-dimensional geometries, 2-D and 2-D-A. For this purpose, results are compared with exact solutions for stagnation point heat transfer on a cylinder (2-D) and sphere (2-D-A) (cases for which exact solutions are readily available for comparison purposes).

The boundary layer edge velocity variations near the stagnation point (small $\frac{x}{R}$) are

$$\text{cylinder,} \quad u_e = 2u_\infty\left(\frac{x}{R}\right) \tag{A14}$$

$$\text{sphere,} \quad u_e = 3/2\ u_\infty\left(\frac{x}{R}\right)$$

where R is the radius of the cylinder or sphere
and u_∞ is the freestream velocity

Inserting Equations (A14) into (A6) and the result into Equation (A5), after some manipulation the stagnation point $(x/R \to 0)$ Nusselt number is obtained

$$Nu_R = A\ Re_R^{1/2}\ Pr^{1/3} \tag{A15}$$

where $Nu_R \equiv \frac{(\rho_e u_e C_H) c_p R}{k}$, $Re_R \equiv \frac{\rho_\infty u_\infty R}{\mu_\infty}$. The exact (for Prandtl numbers near unity) and energy integral values of A are

	exact	energy-integral method
cylinder	0.81 (Reference 26)	0.664
sphere	0.93 (Reference 27)	0.813

The approximate and exact results compare within about 18 percent for the cylinder and within about 13 percent for the sphere. It is significant that the best comparison is for the 2-D-A case, suggesting that although the effects of variable freestream velocity are not as accurately predicted for the 2-D type geometry as would be hoped (see the previous subsection), these shortcomings of the approximate technique are somewhat offset for the 2-D-A geometry, the typical rocket-nozzle case.

A.2 MODIFICATION OF THE PRESENT TECHNIQUE TO ACCOUNT FOR TRANSPIRATION (ABLATION)

Certain exact solutions have been obtained by Aerotherm personnel using numerical methods for the effects of constant blowing rate along a flat plate for both the laminar case (Contract NAS9-4599) and the turbulent case (Reference 28). The basic elements for the detailed exact calculation of all

aspects of boundary-layer behavior for both the laminar and turbulent cases have been developed under these various programs. In spite of the availability of these basic elements, however, further developments and study efforts are necessary before the techniques for the general turbulent boundary-layer case (in particular) can become operational. In the meantime, some of the available results from these programs can be used to aid in the approximate characterization of the boundary layer convection transfer coefficients with transpiration or blowing. Preliminary attempts to characterize the effects of transpiration were made in Reference 1 through extension of the energy integral technique to include transpiration. In this section, the effort of Reference 1 are refined for the turbulent case and also extended to include transpiration into the laminar boundary layer.

The basic differential equation to be employed is the boundary-layer integral Equation (A1), which is for the case of an isothermal flat plate

$$\frac{d\varphi}{dx} = C_H + \beta \tag{A16}$$

In this development, the following functional relationship for the Stanton number with transpiration is assumed to apply

$$C_H = C_H(Re_\varphi, \beta, Pr) \tag{A17}$$

The effect of transpiration C_H is manifested both by its upstream influence on Re_φ as well as its local influence. A simple film theory type of equation for C_H, which when inserted into Equation (A16) will yield a variation of C_H with surface distance, is (Reference 1)

$$C_H = \frac{2\lambda\beta}{e^{\frac{2\lambda\beta}{C_{H_\varphi}^*}} - 1} \approx C_{H_\varphi}^* \left(1 - \lambda \frac{\beta}{C_{H_\varphi}^*} + \ldots\right) \tag{A18}$$

where C_{H_φ} = Equation (A3) (tentatively) and where λ is a constant whose value depends upon whether the boundary layer is laminar or turbulent. Unfortunately, for large blowing, when Equation (A18) is inserted into either Equation (A1) or (A16), these equations cannot be formally integrated, and one must resort to numerical methods. However, for the case of small constant blowing along an isothermal flat plate, the approximate form of Equation (A18) for small blowing can be inserted into Equation (A16) to yield

$$\frac{d\varphi}{dx} = C_{H_\varphi}^* + (1 - \lambda)\beta \tag{A19}$$

where $C_{H_\varphi}^* = \frac{E}{\varphi^{\frac{m}{1-m}}}$ and E = a constant for this case. Letting $(1 - \lambda)\beta \equiv F$ = constant for this case, then

$$\frac{d\varphi}{dx} = \frac{E + F\varphi^{\frac{m}{1-m}}}{\varphi^{\frac{m}{1-m}}} \approx \frac{1}{\frac{\varphi^{\frac{m}{1-m}}}{E} - \frac{F}{E^2}\varphi^{\frac{2m}{1-m}}} \quad \text{(for small F)} \tag{A20}$$

The approximate form of Equation (A20) can be formally integrated to yield the variation of φ with x. The resulting value of φ, when inserted into Equation (A3), yields a transcendental function for the variation of $C_{H_\varphi}^*$ with x. When this function is expanded in a binomial series, and higher order terms containing β are neglected, a quadratic equation for C_{H_φ} results which yields

$$C_{H_\varphi}^* \approx C_{H_x}^* - \frac{m}{1+m}(1 - \lambda)\beta \tag{A21}$$

where $C_{H_\varphi}^*$ = Equation (A2) (tentatively) and from the approximate form of Equation (A18)

$$C_H = C_{H_\varphi}^* - \lambda\beta \approx C_{H_x}^* - \lambda\beta - \frac{m}{1+m}(1 - \lambda)\beta \tag{A22}$$

From Equation (A22), it can be seen that for small constant transpiration along an isothermal flat plate, the Stanton number is equal to that obtained without blowing, $C_{H_x}^*$, less terms which include the blowing rate. An alternate film theory type relation for this case which relates the Stanton number to that obtained without transpiration at a given value of Re_x is,

$$C_H = \frac{2\bar{\lambda}\beta}{e^{\frac{2\bar{\lambda}\beta}{C_{H_x}^*}} - 1} \approx C_{H_x}^*\left(1 - \bar{\lambda}\frac{\beta}{C_{H_x}^*} + \ldots\right) \tag{A23}$$

The distinction between λ or $\bar{\lambda}$ is that the former is appropriate to the comparison of C_H to the zero local blowing value of C_H ($C_{H_\varphi}^*$) at constant Re_φ whereas the latter is appropriate to comparisons performed at constant Re_x along a flat plate with constant blowing. Thus, Equation (A18) is presumed to correct the Stanton number for local blowing which is in general variable, and

Equation (A23) is presumed to correct the Stanton number for constant local and average blowing along a flat plate only. For this latter case, the approximate form of Equation (A23) can be equated to the latter equality of Equation (A22) to obtain a relation between $\bar{\lambda}$ and λ.

$$\lambda = (1 + m)\bar{\lambda} - m \tag{A24}$$

Proposed turbulent values of λ or $\bar{\lambda}$ applied without distinction to the linearized forms of Equations (A18) or (A23) have been 1/2 which is obtained from film theory), 0.37 (Reference 29), and 1/5 (Reference 30). The value recommended in Reference 6 is $\lambda = 1/5$, the value used to account for transpiration in early ablation predictions using the Aerotherm charring material ablation computer program. These latter two values of λ have been obtained through correlations of certain early experimental transpiration data. In Reference 28 it was found that a value of $\bar{\lambda} = 1/2$, used in the exponential form of Equation (A23), provided a suitable curve fit to the "exact" theoretical results for the transpired turbulent boundary presented in Reference 28. This value of $\bar{\lambda}$ yields a value of $\lambda = 2/5$ from Equation (A24) (compared to $\lambda = 3/8$ from Reference 1 evaluated in a less exact manner) for the turbulent case ($m = 1/5$). It is significant that the "exact" theoretical results of Reference 28 compare extremely well with available flat plate transpiration data. By inference, the approximate formulation presented here, when solved by the requisite numerical techniques, will also compare favorably with available turbulent transpiration data.

The laminar case has been considered here by obtaining an "exact" solution to the nonsimilar laminar boundary layer with constant blowing along a flat plate. This solution was obtained through use of an Aerotherm computer program developed under Contract NAS 9-4599 which numerically solves the laminar boundary layer equations through application of an integral-matrix technique. One case was run with constant blowing, $\beta = 5.1 \times 10^{-5}$, and it was found that the exponential form of Equation (A23) with $\bar{\lambda} = 2/3$ compares with the integral-matrix solution within less than 5 percent for values of $\beta/C_{H_x}^*$ less than 1.0. The corresponding value of λ from Equation (A24) is $\lambda = 1/2$ ($m = 1/2$), which is identically equal to the value obtained from film theory.

The effects of local and upstream blowing on Stanton number have been briefly considered in this subsection. The basic procedure for modification of the energy integral technique for the computation of heat-transfer coefficients has been indicated. The introduction of arbitrary blowing distributions to the basic boundary-layer energy integral differential equation obviates its solution in closed form, or at least, the attempts made in this study to obtain a closed form solution through application of various transformations have been unsuccessful. For this reason, a solution has been obtained to an approx-

imate differential equation for small constant blowing along a flat plate, resulting in a relation distinguishing the effects of local blowing from effects due to upstream blowing. Although a solution has not been obtained for large blowing, relations have been developed, and constants have been evaluated in such a way that it is expected that a numerical integration of the basic equation will yield results which will compare favorably with available exact solutions. In particular, the effects of local variable blowing, and the effects of constant blowing along a flat plate can be evaluated from the exponential forms of Equations (A18) and (A23), respectively, using the following constants evaluated in this study

	λ Equation (A18)	$\overline{\lambda}$ Equation (A23)
laminar	1/2	2/3
turbulent	2/5	1/2

A.3 RECOMMENDED EXTENSIONS TO THE ENERGY INTEGRAL METHOD

Based on studies presented in this Appendix, it is believed that the basic concepts of the energy integral method are sufficiently realistic to form the basis for generation of valid input information for ablation calculations in a relatively simple and straightforward manner. Certain improvements in the application of these basic concepts seem appropriate, however.

The recommended form of the energy integral differential equation (presented here only for the special case of the low speed constant property boundary layer) is as follows for both the laminar and turbulent boundary layers,

$$\frac{d\varphi}{dx} = \frac{2\lambda\beta}{e^{\frac{2\lambda\beta}{C_{H_\varphi}^*}} - 1} + \beta - \varphi\frac{d}{dx}\ell n\left[r\rho_e u_e(T_{te} - T_w)\right] \qquad (A25)$$

The recommended values of λ are 1/2 and 2/5 for the laminar and turbulent boundary layers, respectively.

The variation of $C_{H_\varphi}^*$ presented as Equation (A3), although quite accurate for the laminar boundary, is accurate only for a restricted range of Re_φ for the turbulent case. The form of Equation (A3) was retained in the development of the method primarily because this particular form allowed the formal integration of the differential equation. Inasmuch as Equation (A25) cannot be integrated formally, but must be integrated numerically if the effects of transpiration are to be taken into account, an improved representation of $C_{H_\varphi}^*$ for the turbulent case is in order; this should also yield improvements in results for the turbulent case without transpiration as well.

For this purpose, a logarithmic form for the turbulent variation of $C_{H_\varphi}^*$ with Re_φ was examined, and found to give an improved fit to the exact results of Reference 28 for Prandtl number of unity ($C_f/2$ vs. Reynolds number on momentum thickness) and 0.71 (air). The adopted relation contains the same Prandtl number dependence as Equation (A3) for the turbulent case (that is, $C_{H_\varphi}^* \propto Pr^{-\frac{2}{3(1-m)}} = Pr^{-5/6}$), and is evaluated such that the magnitude of $C_{H_\varphi}^*$ equals that from Equation (A3) at an energy thickness Reynolds number, Re_φ, of 5×10^3. This modified relation is:

$$\left(C_{H_\varphi}^*\right)_{turb} = \frac{0.0123}{Pr^{5/6}} \left(\log Re_\varphi\right)^{-8/5} \tag{A26}$$

In this appendix, only the constant property, low-speed boundary layer has been considered. The concepts of the method are such as to provide a basic framework for application of simple correlations of exact results for certain other parameters that are not considered here. For example, the Prandtl number dependency considered here appearing in Equation (A2) was derived in the past by way of a simple correlation of exact results obtained for the laminar boundary layer with variable Prandtl number (see Figure A1, n = 0), resulting in a basic extension of the Reynolds analogy to Prandtl numbers different than unity. This correlation, obtained for the laminar boundary layer, has been also applied successfully to correlations of data for the turbulent boundary layer (see also the theoretical results of Reference 28), because the effects of molecular properties (like Prandtl number) are manifested largely in the laminar sublayer. Correlations are presently available to correct for variable properties and for the high-speed boundary layer flow without transpiration, again through correlations of exact laminar boundary layer results to establish appropriate reference property conditions. At present, these corrections,which have resulted in part from correlations of exact solutions, are available for modification of Equation (A25) to account for high speed and non-constant property effects for the non-transpired boundary layers, and these corrections should be employed in the solution of Equation (A25).

The method proposed to account for transpiration is strictly applicable only to the case of transpirants similar to those of the freestream (the constant property case considered here); the introduction of ablation products to the boundary layer generally results in "transpiration" of species different than those of the freestream. Reference 30 proposes a correction to Equation (A18) (for example) to account for observed effects of differences in molecular weight between the freestream and transpirant. Corrections can now be better derived through correlations of exact results which can now be obtained using the integral matrix non-similar laminar boundary layer solution technique.

In many respects, the boundary layer differential equations for mass, momentum, and energy are similar. For unity Prandtl and Lewis numbers, the mass and energy boundary layer differential equations are identical in form, as are their respective forms of the integral boundary layer equations (the integral form of the momentum boundary layer equation differs from those for mass and energy for the typical case of finite streamwise pressure gradient). In the previous discussions, only the energy boundary layer was considered. However, the developments are also appropriate to the mass boundary layer (for future consideration) through proper substitution of analogous terms. That is, heat transfer coefficient (C_H) is analogous to mass transfer coefficient (C_M), Prandtl number is analogous to Schmidt number, energy thickness is analogous to mass thickness, and enthalpy is analogous to species concentration. Although terms in the energy equation are analogous to like terms in the mass equation, this does not in general mean that the heat transfer coefficient (for example) is proportional to the mass transfer coefficient, unless the variations of all like terms with surface distance are similar.

The recommended revisions to the energy integral technique (or its analogy, the mass integral technique), and the mechanisms for this revision and checkout are as follows:

1. Develop a computer program to facilitate the numerical integration of the "basic" energy differential equation, Equation (A25), using the improved Stanton number correlation, Equation (A26), for the turbulent case and Equation (A3) for the laminar case.

2. Where appropriate, modify terms in the basic differential equation to account for high speed and non-constant property effects for arbitrary boundary layer edge gases (this has already been done in Reference 3 for the case of no-blowing using the more approximate turbulent Stanton number correlation of Equation (A3)).

3. Obtain exact solutions of the laminar boundary layer for transpiration of foreign gases and correlate these results to obtain approximate analytical corrections to Equation (A18) for inclusion in Equation (A25) and its subsequent integration.

4. Include in 1 above the capability to simultaneously calculate mass transfer coefficients using methods similar in concept to the computation of heat transfer coefficients.

The incentive for these revisions is provided by: 1) the necessity to accurately characterize heat and mass transfer coefficients as input to the thermochemical ablation calculations; 2) to have at hand an inexpensive computational procedure which adequately reproduces the more expensive and time-consuming exact boundary layer solutions as these solutions become available; and 3) to be able to obtain realistic approximate results which cannot await the more exact boundary layer developments of the future. The exemplary

problem of the effects of significant upstream ablation on downstream erosion rates, considered under this program (Section 4.1) and in Reference 1, is one which cannot presently be handled in a satisfactory manner with an available operational scheme. It is believed that the developments recommended herein will provide the means to explore these effects. In addition, the resulting computational scheme will have application to a wide variety of other problems (for example, transpiration-cooled or liquid-cooled nozzles).

REFERENCES

1. Schaefer, J. W. and Dahm, T. J.: Analysis of Ablative Material Erosion for the Thiokol 156-2C-1 Motor Nozzle (U). Vidya Report No. 206, Vidya Div. of Itek Corp., November 15, 1965, (CONFIDENTIAL).

2. Dahm, T. J. and Schaefer, J. W.: Preliminary Analysis of Ablation Material Performance for Two Lockheed Propulsion Company 156-inch Solid Rocket Motor Nozzles. Vidya Technical Note 8032-TN-1, Vidya Div. of Itek Corp., May 21, 1965.

3. Dahm, T. J. and Schaefer, J. W.: Analysis of Subscale Results and Final Prediction of Ablation Material Performance for Two Lockheed Propulsion Company 156-inch Solid Rocket Motor Nozzles (U). Vidya Technical Note 8032-TN-2, Vidya Div. of Itek Corp., July 36, 1965, (CONFIDENTIAL).

4. Dahm, T. J. and Schaefer, J. W.: Comparison of Predicted Ablation Material Performance with Firing Results for Two Lockheed Propulsion Company 156-inch Solid Rocket-Motor Nozzles (U). Aerotherm Technical Note 8032-TN-3, Aerotherm Corp., May 1966. (CONFIDENTIAL)

5. Schaefer, J. W., and Dahm, T. J.: Computer Program Calculation of Ablative Material Performance for Solid Rocket Motor Applications (U). CPIA Publ. No. 111, Vol. 1, pp 371-395, June 1966. (Paper presented at the ICRPG/AIAA Solid Propulsion Conference, Washington D. C., July 19-21, 1966.) Aerotherm Corp., (CONFIDENTIAL)

6. McCuen, P. A., Schaefer, J. W., Lundberg, R. E., and Kendall, R. M.: A Study of Solid-Propellant Rocket Motor Exposed Materials Behavior, Report Number AFRPL-TR-65-33, Vidya Report No. 149, Vidya Div. of Itek Corp., Feb. 26, 1965.

7. User's Manual, Fortran Variable Names, Flow Charts; Aerotherm Charring Material Ablation Program, Version 2, Aerotherm Corp., January 1966, February 1966, April 1966, respectively.

8. User's Manual, Aerotherm Equilibrium Surface Thermochemistry Program, Version 2, Aerotherm Corp., June 1966.

9. Pears, C. D., Engelke, W. T., and Thornburgh, J. D.: The Thermal and Mechanical Properties of Five Ablative Reinforced Plastics from Room Temperature to 750 F. AF Materials Lab., Technical Report No. AFML-TR-65-133, April 1965.

10. Pears, C.D., Engelke, W.T., and Thornburgh, J.D.: The Thermophysical Properties of Plastic Materials from -50° F to Over 700° F. AF Materials Lab., Tech. Doc. Rep. No. ML-TDR-64-87, Part I.

11. Pears, C.D.: The Thermophysical Properties of Plastic Materials from -50°F to Over 700° F. AF Materials Lab., Tech. Doc. Rep. No. ML-TDR-64-87, Part II, April 1965.

12. Private Communication with Lockheed Missiles and Space Company, Sunnyvale, California, August 1964.

13. Kratsch, K.M., Hearne, L.F., and McChesney, H.R.: Thermal Performance of Heat-Shield Composites During Planetary Entry. Presented at the AIAA-NASA National Meeting, Palo Alto, California, Sept. 30 - Oct. 1, 1963.

14. Beecher, N., and Rosensweig, R.E.: Ablation Mechanisms in Plastics with Inorganic Reinforcement, ARS Journal, Vol. 31, No. 4, April 1961, and Erratum, AIAA Journal, Vol. 3, No. 8, August 1965.

15. Blumenthal, J. L., Santy, M. J., and Burns, E. A.: Kinetic Studies of High Temperature Carbon-Silica Reactions in Charred Silica-Reinforced Phenolic Resins. TRW Space T.L. Report 9840-6998-TU000, March 1965 - also The Combustion Institute, Fall Meeting, October 25, 26, 1965, Paper No. WSCL 65-25.

16. Rindal, R. A., Flood, D. T., and Clark, K. J.: Experimental and Theoretical Analysis of Ablative Material Response in a Liquid-Propellant Rocket Engine. Third Quart. Prog. Rep., Contract NAS3-7945, Aerotherm Corp., June 30, 1966.

17. Brokaw, Richard S.: Alignment Charts for Transport Properties Viscosity, Thermal Conductivity, and Diffusion Coefficients for Nonpolar Gases and Gas Mixtures at Low Densities. NASA TR-R-81, 1961.

18. Svehla, Roger A.: Estimated Viscosities and Thermal Conductivities of Gases at High Temperatures. NASA TR R-132, 1962.

19. Ragent, Boris and Noble, Charles E., Jr.: High-Temperature Transport Coefficients of Selected Gases. Vidya Report No. 52, Vidya Div. of Itek Corp., September 1, 1961.

20. Burnell, J. A., Goodwin, F. K., Nielsen, J. N., Rubesin, M. W., and Sacks, A A. H.,: Effects of Supersonic and Hypersonic Aircraft Speed upon Aerial Photography. Vidya Report No. 28, Vidya Div. of Itek Corp., October 1960.

21. Ambrock, G.S.: Approximate Solution of Equations for Thermal Boundary Layers with Variations in Boundary Layer Structure. Soviet Physics, Tech. Physics, Vol. 2, No. 9, 1957.

22. Eckert, E. R. G.: Introduction to the Transfer of Heat and Mass, McGraw-Hill Book Company, New York, 1950.

23. Reynolds, W.C., Kays, W.M., and Kline, S.J.: Heat Transfer in the Turbulent Incompressible Boundary Layer with Arbitrary Wall Temperature and Heat Flux. Final Report - Part III, under contract NAw-6494, Stanford University, July 1957.

24. Kays, W.M.: Convection Heat and Mass Transfer, Department of Mechanical Engineering, Stanford University, Stanford, California. - See also Convection Heat and Mass Transfer, McGraw-Hill Book Company, 1966.

25. Reynolds, W.C., Kays, W.M., and Kline, S.J.: Heat Transfer in the Turbulent Incompressible Boundary Layer with a Step Wall Temperature Distribution. Final Report - Part II, under contract NAw-6494, Stanford University, July 1957.

26. Eckert, E.R.G.: VDI Forshungsheft 416, 1942.

27. Cohen, C.B., and Reshotko, E.: Heat Transfer at the Forward Stagnation Point of Blunt Bodies. NACA TN 3513, July 1955.

28. Kendall, R.M., Rubesin, M.W., Dahm, T.J., and Mendenhall, M.R.: Mass, Momentum, and Heat Transfer within a Turbulent Boundary Layer with Foreign Gas Mass Transfer at the Surface, Part I - Constant Fluid Properties, Vidya Report No. 111, Vidya Div. of Itek Corp., February 1, 1964.

29. Eckert, E.R.G.: Survey of Boundary Layer Heat Transfer at High Velocities and High Temperatures, WADC TR-59-624, 1960.

30. Hidalgo, H.: Ablation of Glassy Materials around Blunt Bodies of Revolution, ARS Journal, September 1960.